SEDIMENT REWORKING MECHANISMS IN SHELF SEAS

In situ observations from the southeastern North Sea

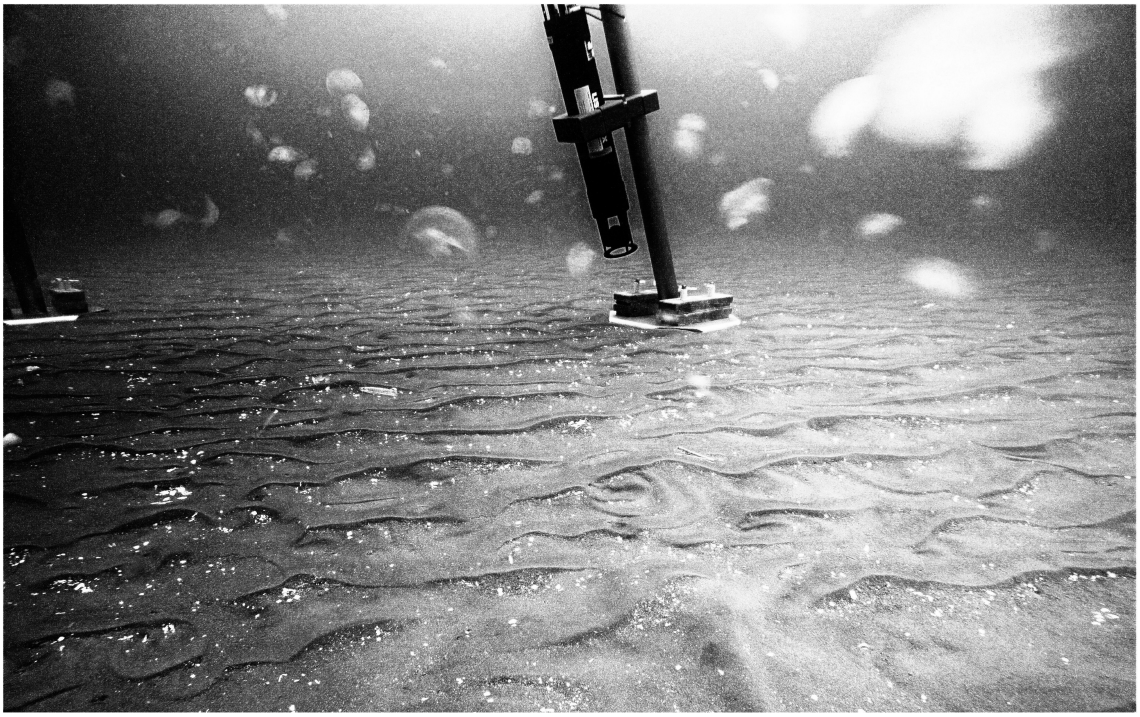

DISSERTATION

zur Erlangung des Doktorgrades der Naturwissenschaften
im Fachbereich Geowissenschaften
der Universität Bremen

vorgelegt von

KNUT KRÄMER

Bremen, April 2018

marum

Universität Bremen

Sediment reworking mechanisms in shelf seas
In situ observations from the southeastern North Sea
Bremen, April 2018

Gutachter:
Prof. Dr. Christian Winter, Christian-Albrechts-Universität zu Kiel
Prof. Dr. Tobias Mörz, Universität Bremen

Betreuer:
Prof. Dr. Christian Winter

ABSTRACT

The seafloor in shallow coastal and shelf seas is a highly dynamic system providing plenty of natural resources and important ecosystem services. Driven by energetic physical forcing, biological activity and intense anthropogenic use, its mobile sediments are constantly overturned. The reworking processes mediate the exchange of abundant organic matter and pollutants across the benthic interface. Coherent in situ measurements of forcing and morphodynamic response help to identify relevant reworking mechanisms, to outline their spatial and temporal scales, and to quantify their impacts on the benthic ecosystem. New high-resolution observation techniques enable also the assessment of small-scale processes that, due to their ubiquity, are yet of shelf-wide importance. This thesis explores three mechanisms in the southeastern North Sea: The morphology and dynamics of small scale-bedforms, the relation of physical and biogenic sediment reworking by bedform migration and bioturbation, and the effect of submarine fluid expulsion. The analysis of these processes reveals new links between physical and biological drivers and illustrates their complex interactions at the benthic interface.

ZUSAMMENFASSUNG

Der Meeresboden in flachen Küsten- und Schelfmeeren ist ein hochdynamisches System, das eine Vielzahl natürlicher Resourcen und wichtige Ökosystemdienstleistungen bereitstellt. Angetrieben durch starke physikalische Kräfte, biologische Aktivität und intensive anthropogene Nutzung werden seine mobilen Sedimente ständig umgelagert. Die Umlagerungsprozesse beeinflussen den Austausch von organischem Material und Schadstoffen zwischen Wassersäule und Sediment. Kohärente In-situ-Messungen des Antriebs und der morphodynamischen Reaktion helfen, relevante Umlagerungsmechanismen zu identifizieren, ihre räumlichen und zeitlichen Skalen zu umreißen und ihre Auswirkungen auf das benthische Ökosystem zu quantifizieren. Neue hochauflösende Beobachtungsmethoden ermöglichen auch die Bewertung kleinskaliger Prozesse, die aufgrund ihrer Allgegenwärtigkeit aber von schelf-weiter Bedeutung sind. In dieser Arbeit werden drei Mechanismen in der südöstlichen Nordsee untersucht: Die Morphologie und Dynamik kleinskaliger Bodenformen, das Verhältnis von physikalischen und biogenen Sedimentumlagerungen durch Bodenformmigration und Bioturbation und die Wirkung von submarinen Flüssigkeitsaustritten. Die Analyse dieser Prozesse zeigt neue Verbindungen zwischen physikalischen und biologischen Akteuren auf und veranschaulicht ihre komplexen Wechselwirkungen an der benthischen Grenzfläche.

ACKNOWLEDGMENTS

This thesis was created at MARUM – Center for Marine Environmental Research at the University of Bremen with support from the GLOMAR graduate school. The position was partially funded by MARUM and project NOAH – North Sea Observation and Assessment of Habitats.

I would like to express my gratitude towards a number of people without whom I would not have completed this work.

My supervisor, Christian Winter, for the right balance between motivating enthusiasm for new approaches and *doktorväterlicher* strictness demanding focus and keeping track with the ever-looming schedule. Tobias Mörz for kindly taking over the second review.

The Coastal Dynamics work group for a warm welcome and an excellent working atmosphere. My fellow PhD students and wonderful office mates Brice, Markus and Mohammad. My colleagues Marius and Gerald for long scientific and non-scientific discussions over coffee and beer. Alice for exchange of experiences with bedforms and babies. Gabriel for all the little technical miracles and company during cruises and Soeren for all the talks about the geeky stuff.

Captain and crew on R/V Heincke for the professional support of the scientific program and the good atmosphere during five cruises in the German Bight.

The developers and contributors behind free and open source software such as Linux, KDE, QGIS, gdal, ImageMagick, MB-System, OpenCPN and LaTeX.

Andreas, Benny and Dennis für ihre Freundschaft, spontane Besuche und Zerstreuung in Schnee, Sand, Wind und Wellen.

Meinen Eltern für eine weltoffene Erziehung und ihre Bereitschaft, mich meiner Wege ziehen zu lassen und mir gleichzeitig immer ein Zuhause zu bieten.

Und schließlich meiner eigenen kleinen Familie für all die Liebe, Symphatie und Motivation, die es braucht um das beständige Auf und Ab in der Forschung durchzustehen.

CONTENTS

LIST OF FIGURES

LIST OF TABLES

LIST OF SYMBOLS

VARIABLES

SYMBOL	UNIT*	MEANING
A	m	Wave orbital amplitude
C	μmol l^{-1}	Concentration
d	m	Water depth
d_{50}	μm	Median grain size
D_*	-	Dimensionless grain size
g	m s^{-2}	Gravitational acceleration
h_s	m	Sonar altitude above seabed
H_s	m	Significant wave height
k_g	m	Grain roughness
$k_{s,f}$	m	Form roughness
L	m	Wave length
r, θ, ϕ	m,°,°	Spherical coordinates
s	-	Density ratio
T_p	s	Wave peak period
u	m s^{-1}	Flow velocity
w_f	m	Sonar footprint width
x, y, z	m	Carthesian coordinates
$z_{0,f}$	m	Form roughness height
α	°	Bedform slope angle
β	°	Sonar beam width
γ	°	Grazing angle
ϵ	m	Error estimate
η	m	Bedform height
θ	-	Shields parameter
λ	m	Bedform length
ν	m^2 s^{-1}	Kinematic viscosity of seawater
ρ_s	kg m^{-3}	Density of sediment
ρ_w	kg m^{-3}	Density of seawater
τ	N m^{-2}	Shear stress
ψ	-	Bedform aspect ratio

* If not indicated otherwise.

Mathematical symbols and operators for quantity a

Symbol	Meaning
$\bar{a}$	Depth-averaged
$\vec{a}$	Vector
$\vec{A}$	Matrix
Δa	Difference
$a(b)$	Functional relation between a and b
σ_a	Standard deviation

Indices

Symbol	Meaning
$\parallel$	Parallel
$\perp$	Perpendicular
c	Current
$crit$	Critical
i	Image extrema method
m	Measured
max	Maximum
tr	Threshold
p	Predicted
s	Statistical method
t	Transect method
w	Wave

List of acronyms

ADCP	acoustic Doppler current profiler
ADV	acoustic Doppler velocimeter
DDM	digital depth model
DEM	digital elevation model
DFT	discrete Fourier transform
EEZ	exclusive economic zone
EPS	extracellular polymeric substances
MBES	multibeam echosounder
MIMS	membrane-inlet mass spectrometer
MUC	multicorer
SBP	sub-bottom profiler
USBL	ultra-short baseline

1

GENERAL INTRODUCTION

1.1 LEAVE NO GRAIN UNTURNED: THE SHELF SEAFLOOR, A DYNAMIC ECOSYSTEM

Continental shelves are the seam between continental landmasses and oceanic water bodies. On these shallow plains with typical water depths smaller than 150 m (Pinet, 2011), the terrestrial and oceanic regime interact. The border between their domains is not strict – with the cycles of tides, storms and floods, estuarine circulation transports terrestrial material across the shelf and seawater intrudes inland.

Due to the high availability of light, reactive solutes and organic matter, the seafloor in shallow shelf seas is a rich and diverse habitat that provides important ecosystem services and natural resources (Snelgrove, 1999; Muller-Karger et al., 2005). Due to the shallow water depth, it is subjected to strong physical forcing and multiple drivers for particle transport across shelves can be defined (Nittrouer and Wright, 1994). In this energetic environment, sediment is continuously overturned and reworked by waves, tides, and wind or density driven currents (Grant and Madsen, 1986; Kenyon and Stride, 1970; Harris and Wiberg, 2001).

In balance with the physical drivers, seafloor sediments in this environment often consist of mobile sands exhibiting a wide range of pattern in seabed morphology and morphodynamics (Durán and Guillén, 2018). The most common bedforms are wave- or current-generated ripples of centimeter height and decimeter length, which can be found in virtually all sandy environments. Under supercritical conditions for sediment motion, their migration in the dominant current direction overturns the upper seabed up to a depth equal to their height.

As a habitat for numerous benthic species, the shelf seafloor is also marked by intense bioturbation due to their burrowing and foraging activities (Mermillod-Blondin and Rosenberg, 2006; Meysman et al., 2006b). The benthic organisms continuously rework the upper few decimeters of the seabed and enhance exchange processes across the benthic interface between sediment and water column.

As former coastal plains with rich vegetation during glacial lowstands, continental shelves are rich in hydrocarbon resources. In combination with groundwater discharge, they are hot spots for submarine fluid expulsion often leading to vigorous overturning of seafloor sediments (Judd and Hovland, 2009).

The economic exploitation and use of natural resources, such as hydrocarbons, minerals and seafood, creates a substantial anthropogenic pressure on the seafloor worldwide (Halpern et al., 2008). The growing demand for renewable energy provided by wind,

waves and currents has brought the shelf seafloor into focus as valuable building ground for offshore energy facilities (Bilgili et al., 2011).

Coastal and shelf systems receive a large input of nutrients and pollutants in the form of particulate matter and solutes from river runoff. These materials are cycled by advective and diffusive transport processes across the benthic interface (Nixon, 1981; Jahnke et al., 2005; O'Driscoll et al., 2013; Ahmerkamp et al., 2017). Frequent reworking by physical, biogenic and anthropogenic forcing drives the exchange between seafloor sediments and water column. Organic and inorganic matter is periodically entrapped in the pore space and released back into the water column. Thus, depending on the time scale of the relevant reworking cycles, the upper seabed acts as temporary sink, source or retention space.

Sediment deposition, transport and reworking of shelf sediments occurs on temporal scales ranging from *instantaneous* (e.g. wave period) over *historical* and *engineering* (e.g. land reclamation and coastal protection) to *geological* (e.g. infill of glacial channels) (Cowell and Thom, 1997). Length scales range from the size of a few millimeters (e.g. macrofauna burrows) to several hundred kilometers (e.g. coastline transgression). Although the typical length scale of an individual process such as ripple morphodynamics is small, its ubiquity may be bridging the scales towards a process with regional impact. The reworking processes addressed in this thesis are illustrated in Figure 1.1.

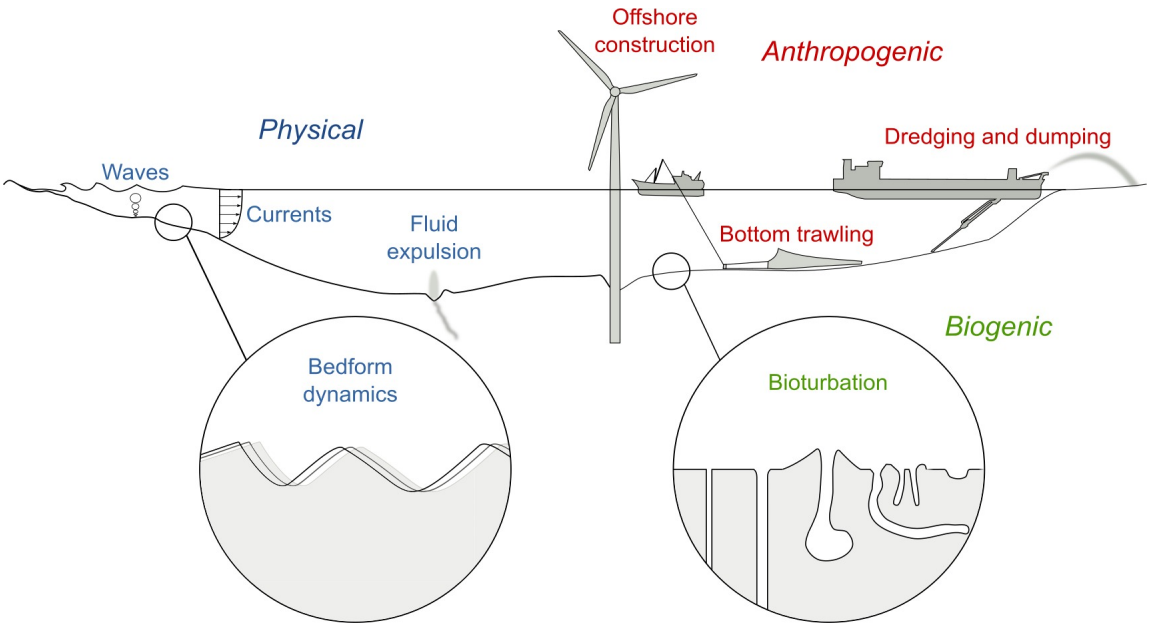

Figure 1.1: Sediment reworking processes on continental shelves

1.2 AIM AND OBJECTIVES

The aim of this thesis is to investigate the importance of relevant reworking mechanisms for sandy sediments in shallow shelf environments on different spatial and temporal

scales. On the basis of coherent data from in situ observations of physical forcing and morphodynamic response in the southeastern North Sea, the effects of three mechanisms are studied:

1. RIPPLE MORPHODYNAMICS: Wave- and current-induced bedload transport becomes apparent in the morphology and morphodynamics of active, small scale bedforms (ripples). In situ observations of ripple dimensions are analyzed to show the gap between inherently simplified empirical relations derived from lab studies and the complex three-dimensional ripple morphology under natural forcing. Furthermore, different methods to measure representative dimensions of natural ripples and their implications for the estimation of seafloor roughness and bedload transport rates are discussed.

2. PHYSICAL AND BIOGENIC SEDIMENT REWORKING: New high-resolution measurements of the seafloor micro-bathymetry unveil the activities of benthic organisms in a morphologically active environment. In a quantitative comparison with physically driven reworking via ripple migration, the relative importance of bioturbation for the overturning of shelf sediments is demonstrated. The analysis of reworking rates from different habitats in the German exclusive economic zone (EEZ) over different seasons reveals interactions between physical and biogenic processes.

3. SUBMARINE FLUID DISCHARGE: A large pockmark field in the shallow, sandy environment at Helgoland Reef, related to the sudden expulsion of methane, was discovered in Summer 2016. The reworking potential imposed by submarine fluid discharge is evaluated and its implications for habitat diversity are discussed.

With the discussion of the driving mechanisms, scales and impacts of sediment reworking mechanisms, this thesis contributes to the understanding of exchange processes at the benthic interface and the role of the shelf seafloor as an important ecosystem under complex physical, biogenic and anthropogenic forcing.

1.3 THESIS STRUCTURE

The study area and methods of data collection are introduced in Chapter 2. Additionally, the background for different reworking mechanisms on continental shelves is illustrated. While anthropogenic action, bioturbation and fluid expulsion are direct mechanical impacts, ripple migration is driven by wave and current shear stress in the bottom boundary layer. The concept of a threshold shear stress for the initiation of motion and uncertainties included in the empirical formulation from the perspective of sedimentological properties and from the perspective of hydraulic forcing are addressed.

In Chapter 3–5, two published manuscripts and one manuscript prepared for submission are presented. The first manuscript describes methods for in situ measurement of

ripple topography in combination with driving forces and compares ripple dimensions predicted by empirical formulations with the range of measured dimensions (Chapter 3).

K. Krämer and C. Winter. Predicted ripple dimensions in relation to the precision of in situ measurements in the southern North Sea. *Ocean Science* 12(6), 2016.

In the second manuscript, biogenic sediment reworking is quantified from laserscans of the micro-bathymetry and biogenic reworking rates are evaluated in comparison to physically driven sediment reworking (Chapter 4).

K. Krämer, S. Ahmerkamp, U. Schückel, M. Holtappels, and C. Winter. The relation of physical and biogenic reworking of sandy sediments in the southeastern North Sea.

In the third manuscript, the sudden emergence of a pockmark field in the area of Helgoland Reef is reported. The expulsion of methane from shallow reservoirs caused a relocation of around 6.9 million cubic meters of sediment (Chapter 5).

K. Krämer, P. Holler, G. Herbst, A. Bratek, S. Ahmerkamp, A. Neumann, A. Bartholomä, J.E.E. van Beusekom, M. Holtappels and C. Winter. Abrupt emergence of a large pockmark field in the German Bight, southeastern North Sea. *Scientific reports* 7(1), 2017.

A fourth manuscript, to which an evaluation of measurements of current shear stress was contributed, is not included here. It is, however, taken up in the discussion as it explains the importance of ripple morphology and morphodynamics on benthic oxygen fluxes (Section 6.2).

S. Ahmerkamp, C. Winter, K. Krämer, D. de Beer, F. Janssen, J. Friedrich, M.M.M. Kuypers and M. Holtappels. Regulation of Benthic Oxygen Fluxes in Permeable Sediments of the Coastal Ocean. *Limnology and Oceanography* 62(5), 2017.

The main findings of the manuscripts are summarized in Chapter 6. The detailed insights are complemented by a general conclusion regarding the scales and the relevance of the individual processes for sediment reworking. Finally, an outlook is given towards new research questions and tools for an enhanced understanding of sediment reworking across multiple scales (Chapter 7).

2

BACKGROUND

2.1 STUDY AREA AND DATA COLLECTION

The North Sea is a shallow semi-enclosed shelf sea, connected to the northeast Atlantic. The German EEZ is located in the southeastern North Sea (Fig. 2.1). Its bathymetry is characterized by shallower slopes along the North and East Frisian coasts with depth of up to 30 meters, incised by the deeper Elbe palaeovalley with depth of around 40 meters. It stretches towards the Dogger Bank with shallower water depths of around 30 meters in its northwest corner. Seafloor sediments consist mostly of fine sand in the shallower regions while muddy sand and sandy mud can be found in the deeper Elbe valley (Figge, 1981) (Fig. 2.1).

The physical forcing is dominated by semi-diurnal tides, wind waves and wind-driven currents (Zeiler et al., 2000; Van der Molen, 2002). Tidal current magnitude and current-induced shear stresses acting on the seafloor are smallest near the amphidromic point located south of Jutland bank and increase towards the coasts. Pattern of wave-induced shear stresses scale largely with water depth, thus areas in the deeper Elbe palaeovalley are less affected by wave action than the shallower nearshore regions along the East and North Frisian coasts. In the sandy regions of the entire German EEZ, small-scale bedforms such as sand waves (McCave, 1971; Terwindt, 1971) and ripples (Kösters and Winter, 2014; Krämer and Winter, 2016) indicate active bedload transport conditions.

Since 2013, repeated surveys with by shipboard multibeam echosounder (MBES) at nine reference stations were carried out to characterize the state of the seafloor habitat and the dynamic range of benthic processes in the scope of project *NOAH – North Sea Observation and Assessment of Habitats*. The emergence and evolution of a pockmark field at Helgoland Reef (Chapter 5) was detected by comparing successive MBES surveys recorded with R/V *Heincke* of a reference area covering around 2 by 2 kilometers over a period of three years. After high methane concentrations in the sediment had suggested the eruption of gas, the final trigger mechanism was identified by evaluating long-term data of wave parameters in the area made available via the *COSYNA* portal (Helmholtz-Zentrum Geesthacht Zentrum für Material- und Küstenforschung GmbH (HZG), 2016).

The assessment of macro- (bedform dynamics, Chapter 3) and micro-scale sediment reworking processes (bioturbation, Chapter 4) acting on hourly to tidal timescales involved the deployment of two autonomous benthic observatories (landers) *SedObs* (Krämer and Winter, 2016; Baschek et al., 2017) and *Lance* (Ahmerkamp et al., 2017) (Fig. 2.2). These four-legged platforms were designed to allow undisturbed near-bed flow and are equipped with optical and hydro-acoustic instruments to obtain coherent measurements

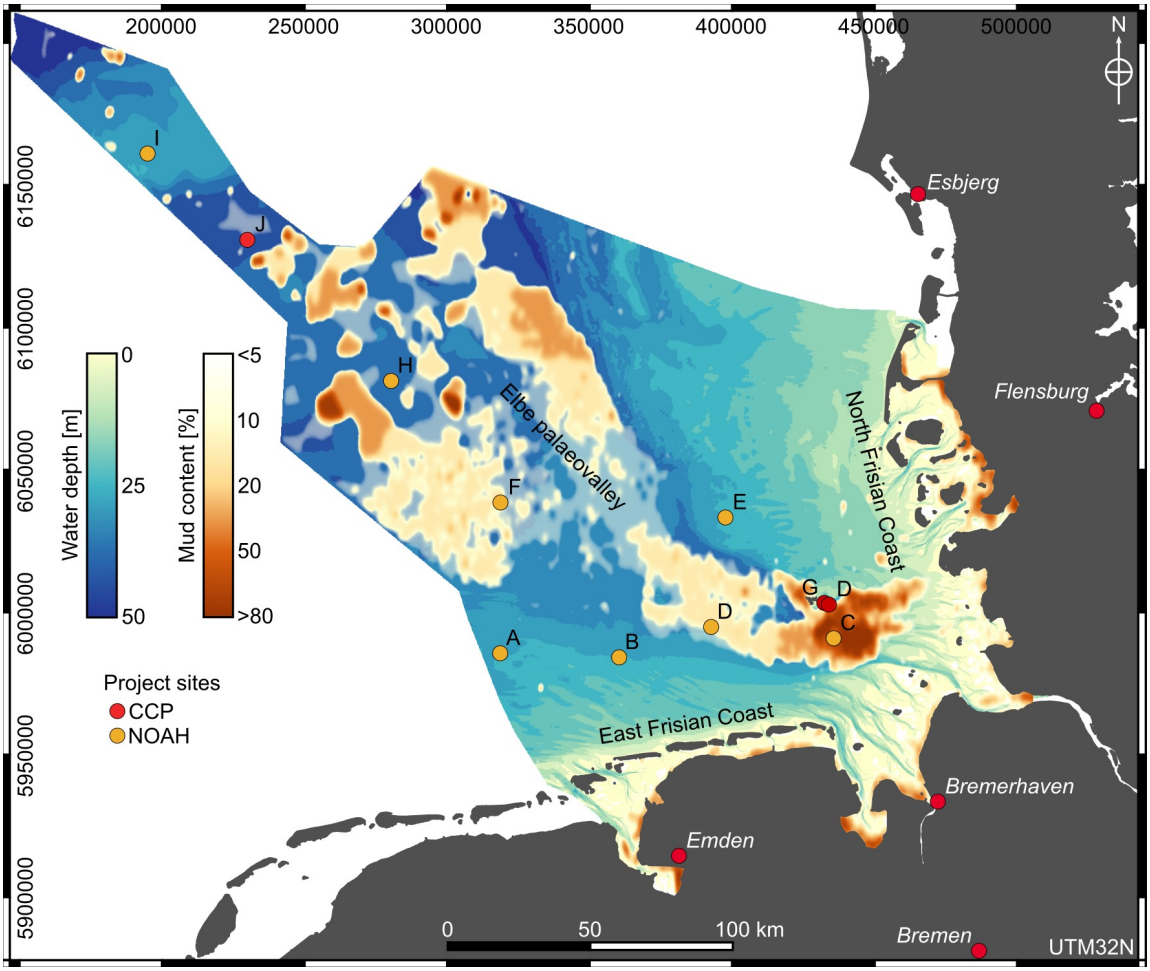

Figure 2.1: Map of the German EEZ in the southeastern North Sea. (a) Bathymetry and mud content in surface sediment. (b) Anually averaged current-induced and (c) wave-induced shear stress from model hindcast.

of the forcing (hydrodynamics) and the corresponding morphodynamic response. The micro-bathymetry was acoustically recorded with centimeter resolution (*SedObs*) and optically with millimeter resolution (*Lance*). To compare successive scans, the scattered raw data were converted into digital elevation models (DEMs) by interpolation with an equidistant cell size. Reworked sediment volumes were then calculated by subtracting successive DEMs.

Wave height and period measured by an upward-looking acoustic Doppler current profiler (ADCP) were used to compute wave shear stress acting on the seafloor. When the instrument did not provide good quality data, model-hindcast data validated by measurements were used. Current-induced shear stresses were derived using a logarithmic fit to 10-minute-averaged near-bed vertical velocity profiles obtained from downward-looking ADCPs. Sediment samples were taken by Shipek and van Veen grab or multicorer (MUC). The median grain size d_{50} was later determined from the grain size distribution obtained by laser-diffractometer analysis in the laboratory.

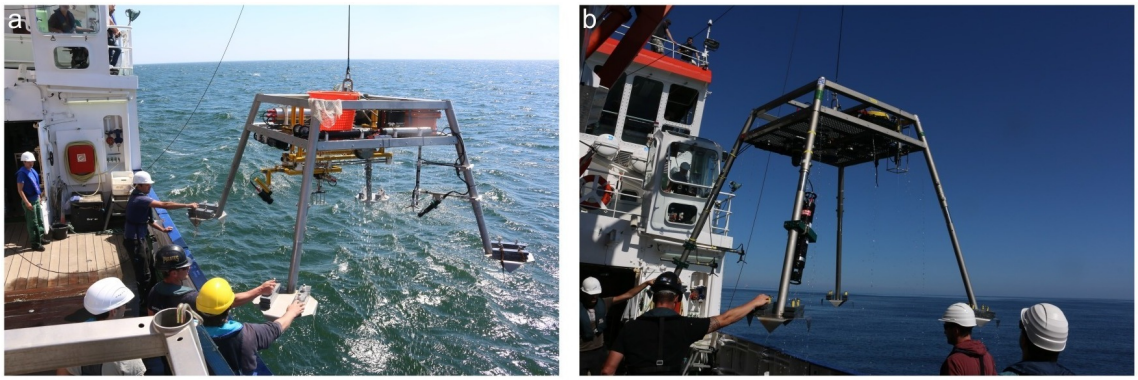

Figure 2.2: Autonomous benthic observatories *Lance* (left) and *SedObs* (right). The landers are equipped with hydroacoustic and optical sensors for coherent measurements of forcing hydrodynamics and the morphodynamic response of the seafloor.

2.2 STRESS AND RESISTANCE: INITIATION OF SEDIMENT MOTION

Relocation and transport of non-cohesive granular sediments is caused either by direct mechanical impact or shear stress exerted on the sediment surface. At the scale of individual sediment particles, the initiation of motion under current or wave forcing is determined by the balance of buoyancy, lift and drag forces against the gravitational force and the contact with its neighboring grains (Luckner and Zanke, 2007; Lamb et al., 2008). The evaluation of this approach requires detailed inspection of the short-term turbulent forces and bedding parameters of individual grains and remains of theoretical value for most practical considerations.

Observing the transition from a state of rest to a fully mobilized upper bed layer, the relation between flow and sediment is described using the critical shear stress. This concept evaluates time-averaged shear stress against the maximum sustainable shear stress representing the resistance of the sediment matrix (Vollmer and Kleinhans, 2007). Historically, the threshold of motion was defined in flume experiments. A layer of sediment was subjected to increasing discharge until the motion of grains could be observed (Hjulstrom, 1935; Shields, 1936). The results can be arranged in the classical Hjulström-diagram and variations thereof, where the depth-averaged flow velocity is plotted over a characteristic grain size. The critical shear stress marks the threshold between an immobile and mobile bed. However, it is rather a gradual transition with increasing probability of sediment motion than a binary change of state. The evaluation of a critical shear stress implicitly reduces the hydraulic forcing and the resistance of the bed to averaged quantities and do not consider temporal or spatial variations of the turbulent flow characteristics and sediment properties. This introduces a high degree of uncertainty in all practical sediment transport applications. For individual observations, the following effects have to be considered.

The availability of measurements leads to a common usage of temporal and depth-averaged quantities of hydraulic parameters. Measurements of high spatial and temporal

resolution highlight the importance of short-term variability of turbulent characteristics, and events with typical time scales of seconds for the suspension of bed material (Nikora and Goring, 2002; Zanke, 2003; Amirshahi et al., 2017). Another degree of uncertainty is introduced by the nonlinear interaction of wave and current flow. For sediment transport and initiation of motion, wave-averaged and maximum shear stress are of relevance, respectively. The magnitude of combined shear stress ranges over a factor of two, depending on the empirical relation used (Soulsby, 1997).

The median grain size d_{50} may be a suitable parameter to describe nearly uniform, well-sorted sediments. However, it is geometrically meaningless already for bi-modal distributions of sand and mud. Natural combinations of two or more well-defined grain sizes introduce hiding and armoring effects where smaller grains are sheltered between bigger ones and larger grains are stabilized by smaller grains filling their pore space (Wiberg et al., 1994).

Due to the global dominance of muddy sands over pure, non-cohesive sands (Schindler et al., 2015), cohesive forces due to clay content in the sediment matrix have to be taken into account when predicting initiation of motion, bedform development and bedload transport. Silt and clay particles making up the muddy sediment fraction introduce cohesive behavior in sediments. Relatively low mud contents significantly increase the threshold of erosion (Mitchener and Torfs, 1996) and impede the formation of bedforms (Baas et al., 2013). Mud contents from 5-10% change the sediment structure in such a way that a transition from non-cohesive to cohesive behavior can be observed (Van Ledden et al., 2004). The erosion behavior of mixtures of sand and mud can be predicted by combining the formulations for pure sand and mud relative to their respective contents (Ahmad et al., 2011).

Biogenic cohesion caused by surficial films of algae prohibiting erosion has a large impact on sediment dynamics in intertidal areas (Davies, 1970; Underwood and Paterson, 1993; Paterson, 1994). Recently, the importance of extracellular polymeric substances (EPS) mixed *into* the sediment matrix has come into focus (Fig. 2.3). Laboratory flume studies show that very low EPS concentrations (<1%) suffice to slow down bedform development by two orders of magnitude (Malarkey et al., 2015; Parsons et al., 2016). In environments with reversing flow and limited time for bedform growth, this means that the observed bedform morphology at a given point in time may significantly differ from equilibrium dimensions predicted by empirical formulae.

2.3 SEDIMENT REWORKING MECHANISMS

Bedload transport and ripple dynamics

Ripples are small scale bedforms of centimeter amplitude and decimeter length, generated by currents at the interface between granular bed materials and overlying fluids (Fig. 2.4). The study of bedform morphology and morphodynamics is important for

Figure 2.3: Sediment surface with biogenic cohesion. Individual grain are glued together by EPS, increasing the critical shear stress of the sediment.

understanding the balance between hydraulic forcing and sedimentological properties. Ripples in recent sediment surfaces (Grotzinger and Milliken, 2012; Pähtz and Durán, 2017) and in the rock record (Immenhauser, 2009; Baas et al., 2016) are evidence of supercritical flow and bedload sediment transport. From a hydraulic perspective, bedforms act as roughness elements in the boundary layer influencing turbulent characteristics of the overlying flow an order of magnitude larger than mere grain roughness (Vanoni and Hwang, 1967; van Rijn, 1984; Styles and Glenn, 2002).

The interaction between near-bed flow and rippled topography influences advective pore-water flow and associated cycling processes (Rocha, 2008). The presence of ripples enhances fluxes across the sediment-water interface up to a factor of ten (Huettel et al., 1996; Ahmerkamp, 2016) and their migration leads to cyclic entrapping and release of suspended particles and pore water (Boudreau et al., 2001). The investigation of bedform morphology and morphodynamics therefore helps to understand the role of ripples as important mediators in the interaction of physical, biological and chemical processes on the seafloor.

Two mechanisms for the initiation of bedforms can be differentiated. First, the apparently spontaneous initiation from a previously flat bed, and second, the development in the wake of a small defect in the bed surface (Venditti, 2013). The initiation of bedforms from a flat bed is a state that can be generated in physical and numerical studies and may occur in quasi-steady, unidirectional river flow after high discharge events eliminating bedforms by wash-out. In estuarine, coastal and shelf environments however, the constantly changing magnitude and direction of hydraulic forcing will rather re-initialize existing bedforms after an inactive period or imprint a new set with a different direction or mode of forcing (wave or current dominated) onto an already existing rippled seafloor in any state of topographical complexity and decay. The appearance of ripples observed in the field ranges from regular, long-crested, two-dimensional features in virtually clean sand to complex three-dimensional features with locally heterogeneous sediment distribution and ample signs of bioturbation (Fig. 2.4).

Bedforms are often described as *vessels* for sediment transport. However, bedform migration in the dominant flow direction is rather an effect of bedload transport over the slopes of bedforms (Stehr, 1975). Bedform migration can therefore be seen as the morphological expression of bedload transport but the bedform migration does not necessarily encompass the bulk bedload transport. However, as in situ bedload transport rates are hard to measure directly, transport rates are estimated from bedform migration rates and their idealized geometries (Kachel and Sternberg, 1971; Hoekstra et al., 2004). The quality of the estimated sediment transport rate then scales with the accuracy of the measured or predicted bedform dimension.

Energetic wave conditions with large near-bed orbital velocities lead to a fully mobilized upper bed layer and consequently to a wash-out of bedforms (Li and Amos, 1999). While the required wave heights and lengths for a complete removal of a rippled morphology may only be reached during intense storm events, the threshold for sediment motion for a fine sand is more commonly exceeded. If waves shear stresses are high enough to enable transport over a few hours, but are not dominant enough to form a new set of wave ripples, they may reduce bedform heights by relocating sediment from crests to troughs.

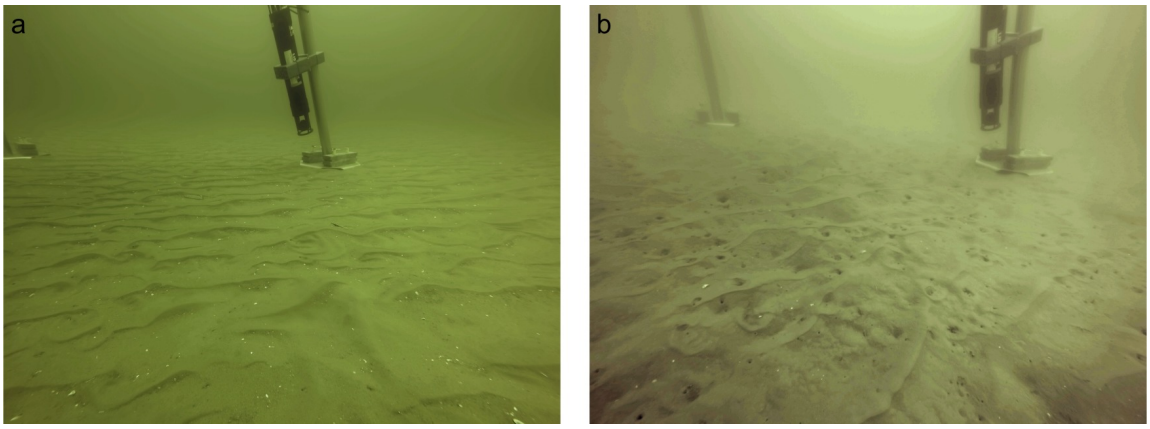

Figure 2.4: Underwater images recorded by the *SedObs* lander showing rippled topography. (a) Active ripples in fine sand. (b) Ripples with signs of surficial bioturbation.

Bioturbation

Bioturbation describes the reworking of terrestrial and marine sediments by burrowing and foraging activities of animals (Fig. 2.5). Organic matter settling to the seafloor is entrapped in the permeable matrix of mobile sand which becomes an important food source for deposit feeders and associated predators. During their search for shelter and food, these benthic species rework the upper few decimeters of sediment and promote the exchange of solutes and particulate matter across the benthic interface (Meysman et al., 2006a). The diffusive relocation of sediment due to biogenic reworking has been shown to be an effective mechanism for the removal of bedform topography. Video ob-

servations prove that a rippled topography can be flattened by burrowing organisms or fish in a matter of a few hours (Amos et al., 1988). The comparison of biogenic and physical reworking rates on an intertidal sandflat shows that biogenic surface reworking rates may reach up to one third of physically driven reworking by bedform migration even in shallow energetic environments (Grant, 1983).

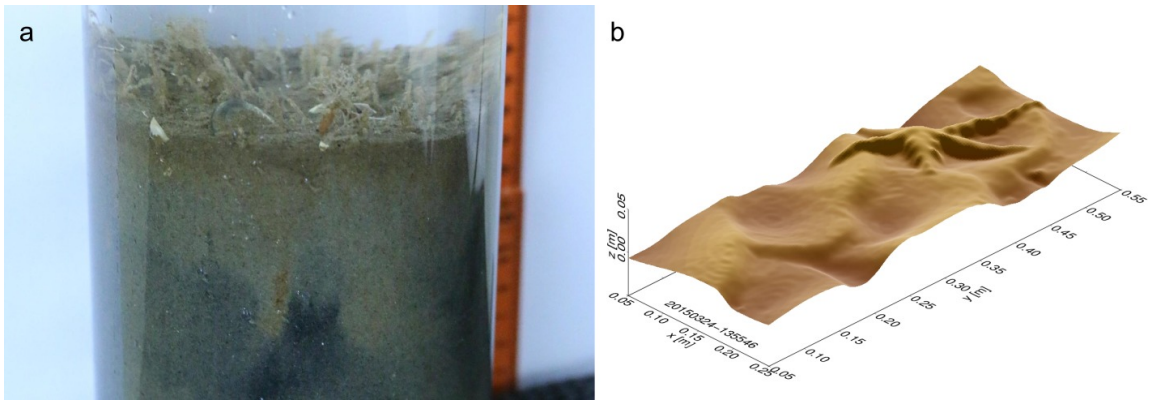

Figure 2.5: Examples of bioturbation by large benthic fauna. (a) MUC sample with *Lanice conchilega*. The upper few centimeters of the seabed have been reworked by the burrowing activity of the worms and oxygen penetrates deeper into the sediment. (b) DEM of the sediment surface (laser-scan) showing a rippled topography and a seastar (*Asterias rubens*).

Submarine fluid flow

As former coastal plains rich in biomass during glacial water level lowstands and as depositional areas during the following sea level rise, shelf seas nowadays contain abundant reservoirs of hydrocarbons (Bernard et al., 1978; Boehm and Requejo, 1986; Isaksen, 2004). In combination with submarine ground water discharge in nearshore regions, they are therefore potential hot spots for submarine fluid expulsion. The most common fluid is methane from bacterial decomposition or geothermic alteration of biomass (Judd and Hovland, 2009). Generally, the seepage of fluids in gaseous or liquid form from the seafloor can be an effective mechanisms for sediment reworking (Fig. 2.6). Sediment stratification is disturbed along the ascension paths from deeper reservoirs. Depending on the pressure of the ejected fluid, seafloor surface sediment can be entrained into the water column. Depending on the strength of local currents, coarse material is deposited nearby and fine material may be carried away from the source in suspension. Fluids vigorously escaping from the seafloor are known to leave characteristic craters named pockmarks which in low shear, cohesive setting may persist over centuries. In coarse environments, pockmarks are not common because the high porosity impedes pressure build-up and rather allows for diffusive seepage (Hovland and Judd, 1988). Additionally, mobile sands are less likely to preserve pockmark features as they are rapidly erased by wave and current action. In areas outside of economic interest such as navigational

channels and offshore construction sites which are not surveyed regularly and with high resolution, any generated pockmark features may therefore vanish before they are detected. Nevertheless, shallow marine sediments are considered an important contributor of global marine methane flux (Hovland et al., 1993).

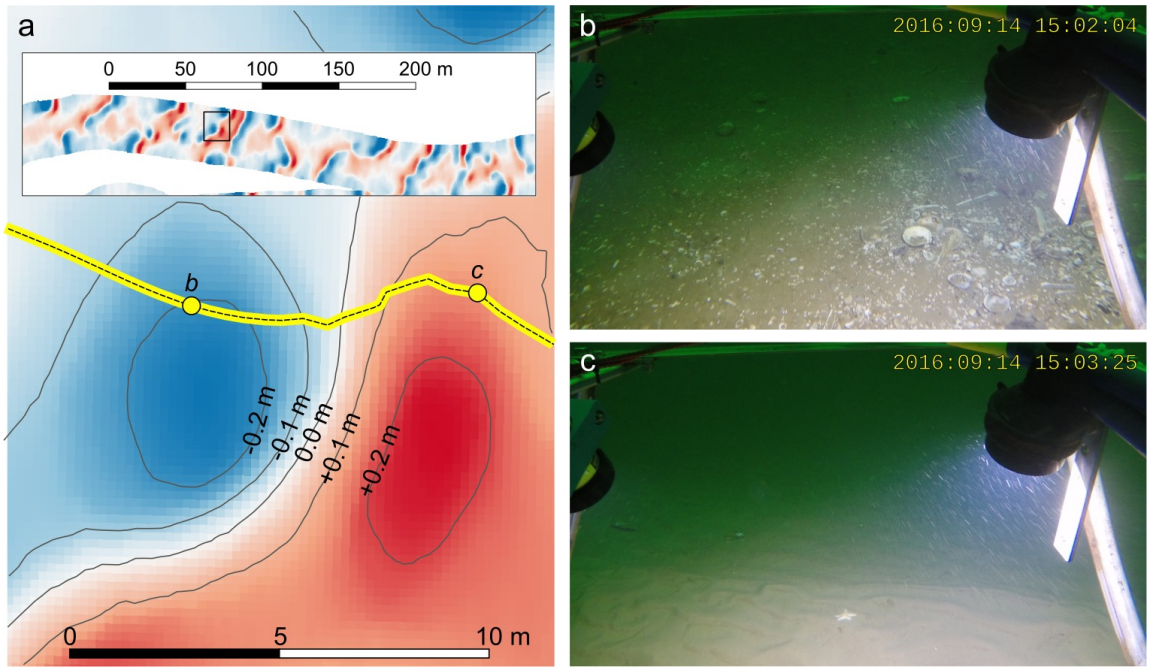

Figure 2.6: (a) Morphology of a single pockmark crater and its neighboring mound as deviation from mean depth. The inset box shows the surrounding bathymetry recorded by shipboard MBES. Video-sled images showing the sorting of (b) coarse sediment and shell debris in the crater and (c) fine sand on the mound.

Anthropogenic impacts

Suitable sediment for land reclamation and coastal protection measures is commonly exploited in coastal areas from designated extraction sites. Material dredged for the maintenance of navigational channels and waterways in estuaries is dumped in equally defined offshore areas. These measures can have a high local impact on sediment characteristics and ecology (Desprez, 2000; Stronkhorst et al., 2003; Simonini et al., 2005; Cooper et al., 2008).

Bottom trawling targeting benthic fish and crustaceans is a common practice on continental shelves. The fishing gear utilized includes devices such as tickler chains or beams to stir up benthic fish and otter boards to keep the mouth of the net open. These heavy mechanical parts plow the sediment surface, leave marks of 10–25 cm depth in the seafloor (Sinclair et al., 2002) and suspend large amounts of fine sediment, leading to an export of sediments from open shelves (Oberle et al., 2016). Highly targeted areas are swept dozens of times per year. Depending on sedimentological properties and hydro-

dynamic forcing, trawl marks may be preserved over periods of several months in low shear environments (Fig. 2.7).

Owing to the global transition from nuclear and fossil to renewable energy resources, offshore wind energy has recently seen a large increase in installed capacity (Bilgili et al., 2011; Kumar et al., 2016). Wind parks are constructed in deeper water farther offshore (Rodrigues et al., 2015), and this trend is expected to continue (Bilgili et al., 2011). In situ and remote sensing observations and modeling studies indicate impacts of offshore wind energy installations on local suspended and bedload sediment transport dynamics (Vanhellemont and Ruddick, 2014; Baeye and Fettweis, 2015; Nagel et al., 2018).

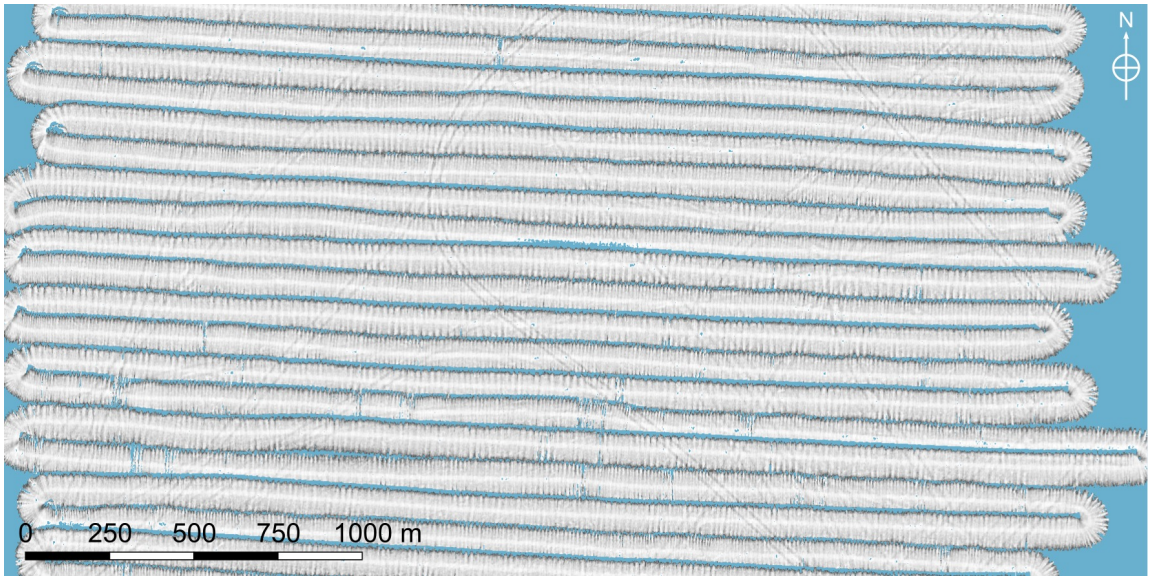

Figure 2.7: Bathymetry recorded by MBES at station NOAH-H (see Fig. 2.1) in September 2014. Bottom trawling gear has left marks in the seafloor. Individual trawl marks could still be detected nine months later during a follow-up survey in June 2015.

3

PREDICTED RIPPLE DIMENSIONS IN RELATION TO THE PRECISION OF IN SITU MEASUREMENTS IN THE SOUTHERN NORTH SEA

Knut Krämer and Christian Winter

Manuscript published in *Ocean Science*, 12(6), 2016.

ABSTRACT: Ripples are common morphological features in sandy marine environments. Their shapes and dimensions are closely related to local sediment properties and forcing by waves and currents. Numerous predictors for the geometry and hydraulic roughness of ripples exist but, due to their empirical nature, they may fail to properly reflect conditions in the field. Here, measurements of tide and wave generated ripples in a shallow shelf sea are reported. Discrete and continuous methods for the extraction of ripple dimensions from DEMs are inter-compared. The range of measured ripple dimensions is quantified and compared to the results of empirical predictors.

The repeatability of a measurement for inactive conditions is taken as the *precision* of measurements of bedform dimensions. The *accuracy* of measurement is assessed via comparison to predicted dimensions. Results from field data show that the precision of measurements is limited to 10% of the absolute ripple dimensions. The application of different methods for the detection of ripple heights may result in form roughness heights differing by up to a factor of two between the traditional statistical estimate and a full evaluation of the spatial bathymetry.

3.1 INTRODUCTION

Small scale bedforms like ripples are ubiquitous morphological features in sandy coastal and shelf sea environments. Their formation and dynamics are controlled by waves and currents, while their equilibrium dimensions are commonly described as being related to a characteristic sediment grain size. The existence and evolution of ripples play important roles in the interaction between the sea bed and water column (Grant and Madsen, 1979; Bartholdy et al., 2015). Hydraulic roughness and extraction of momentum from the mean flow is enhanced beyond the effect of mere grain roughness by orders of magnitude due to the presence of ripples (Zanke, 1982; Soulsby, 1997). Furthermore, the presence of ripples influences turnover rates of nutrients and pollutants in the benthic environment when compared to a flat seabed (Nelson et al., 2013; Ahmerkamp et al., 2015).

If the threshold of motion (expressed as the critical bed shear stress or the dimensionless Shields parameter) for a characteristic grain size is exceeded, sediment is transported

and bedforms develop. As a fundamental understanding of bedform development is still pending and deterministic prediction is not yet possible, equilibrium ripple predictors based on extensive laboratory and field datasets exist for waves (e.g. Soulsby et al., 2012; Nelson et al., 2013), currents (e.g. Soulsby et al., 2012; Bartholdy et al., 2015) or for combined flows (e.g. Li and Amos, 1998). A classification of the type of bedform and corresponding dominant forcing can be made using the ratio of wave and current shear stress. Wave ripples can be subdivided into orbital ripples scaling with wave orbital diameter (Traykovski et al., 1999), anorbital ripples scaling with grain size (Maier and Hay, 2009) and intermediate forms (Clifton and Dingler, 1984). The dimensions of current ripples are usually related to grain size only (Yalin, 1964, 1985). In contrast to dunes, ripple dimensions are described as independent of the flow depth (see classification in Venditti, 2013); however, by applying a virtual boundary layer concept, Bartholdy et al. (2015) recently demonstrated that water depth may actually be a controlling factor along with grain size and flow velocity.

Under nonsteady forcing conditions, bedforms continuously adjust in shape and eventually migrate. Equilibrium ripple predictors may not capture this adaptation process resulting in limited prediction of ripple dimensions during morphodynamically active periods. Groundbreaking flume experiments on the development and adaptation of current ripples in very fine sand have been carried out by Baas (1994), introducing an exponential relaxation scheme for the adaptation of ripple dimensions under changing flow conditions. Time-evolving (nonsteady) ripple predictors have only recently been suggested by Traykovski (2007) and Soulsby et al. (2012). These models also employ an exponential relaxation with a given timescale and rate-of-change coefficients during active conditions. This allows for smooth transitions of bedform dimensions and also include decay processes due to wash-out and sheet flow based on additional critical shear stress levels as well as bioturbation.

Understanding of the dynamics of in situ ripple fields may be impeded by relict ripples, which are observed under conditions not related to their formation. These may be inactive bedforms during low flow conditions (around slack water in tidal environments, or after a storm).

A large number of empirical ripple predictors have been derived from data acquired in flume studies. Hydrodynamic boundary conditions, local sedimentology and (micro-) biological effects in the field however may be different from flume experiments, e.g. in combined current and waves, in tidal environments dominated by periodically changing flow conditions, or in deep sea environments. This makes field data a necessary prerequisite for the understanding, modeling, and assessment of bed conditions (Schindler et al., 2015; Malarkey et al., 2015).

Methods of ripple measurements in laboratory flumes and in the field make use of optical and acoustical instrumentation. Among others, Li and Amos (1998) used underwater cameras in combination with a scale bar to determine ripple wave lengths. Hay and Wilson (1994) and later Hay and Mudge (2005) used rotary side scan sonar images

to describe the evolution of bedform wave lengths during storms. Traykovski (2007) used a sector scanning sonar to measure ripple wave lengths while estimating the height of migrating ripples from the time series of a point measurement of the bed level from an acoustic backscatter sensor. Bell and Thorne (2007) developed a 3D profiling sonar to measure the small scale bathymetry of rippled sea beds. Before that, the same authors employed a 2D scanning sonar to measure ripple dimensions along transects (Bell and Thorne, 1997). Janssen (2004) collected high resolution bathymetry data using a laser line in rectified camera images taken from a moving sledge. Commonly no assessment of measured accuracy is reported in these studies, despite the range of uncertainty in the technical set-up, analysis, and derivation of seabed properties.

In literature, spatially averaged values of ripple dimensions are often reported while the geometric properties of individual bedforms or their statistical distribution are not. However, van der Mark et al. (2008) show that even under laboratory conditions with uniform sediment and stationary flow conditions, bedforms dimensions are far from uniform.

Bedform dimensions and shape can change drastically, when the nature of the dominant forcing changes from current to strong wave dominance or vice versa (Amos and Collins, 1978). This paper is focused on active ripples, i.e. bed conditions in which the shape or dimensions of ripples change over the observation time frame or in which they migrate without changing their general shape or orientation. The time required for the adaptation is a function of the sediment transport rate and thus related to the excess shear stress induced by waves or currents and the sediment properties. For current ripples, Baas (1993, 1994) showed in a flume study that the adaptation time is a function of the inverse power of flow velocity and ranges from a few minutes to several days. Additionally, bedform heights were shown to adapt faster than wave lengths. His dataset was used to calibrate the empirical rate-of-change parameters in the time-evolving scheme by Soulsby et al. (2012) with two expressions for height and length. For wave induced bedforms, Nelson and Voulgaris (2014) show that bedform heights adapt last after wave lengths and orientations have almost reached a new stable equilibrium. The adaptation time scale for wave ripples is related to the wave period by Soulsby et al. (2012) and the rate-of-change parameter is related to the wave mobility number. Recently, Malarkey et al. (2015) further highlighted that bedform development can be significantly slowed down by low concentrations (<1%) of biologically cohesive EPS in the sediment matrix.

The overall aims of this study are:

1. An assessment of the precision of different methods for the detection and measurement of small scale bedforms from high resolution sonar data in a shelf sea environment

2. The comparison of the measurement precision to the dimensions of small scale bedforms calculated by different wave and current ripple predictors

In the following the bathymetry and sedimentary conditions at the study site on a sandy shelf seabed in the North Sea are described. The setup and devices used to measure the relevant data are shortly introduced. Processing steps for different methods to extract bedform dimensions from raw sonar data are detailed. The measured hydro- and morphodynamic data and ripple characteristics collected over two tidal cycles are analyzed. The ranges and error margins determined by the technical specifications of the sensors and different methods employed to derive parameters from raw sensor data are reported. The range of bedform dimensions as a result of different methodology is shown and evaluated. This range is related to the dimensions derived from ripple predictors. Implications for the calculation of bedform roughness from measured ripple dimensions are discussed.

3.2 METHODS

3.2.1 *Study site*

Field data were acquired during cruises on R/V *Heincke* to the German Bight at station D (54.09118° N, 7.35881° E) of the NOAH project[1] (North Sea Observation and Assessment of Habitats). An autonomous lander was deployed during cruise HE441 (20–28 March 2015) over a period of around 36 hours. The station was also visited during cruise HE447 in June 2015 but the bedforms were inactive then.

Station NOAH-D is located in the inner German Bight in a water depth of 35 m (Fig. 3.1). Prior to deployment, a survey of the area surrounding the deployment site by MBES revealed a flat and featureless bathymetry on the larger scale (500 m radius). The grain size analysis of grab samples taken prior to deployment of the lander showed bed sediments of fine sand with a median grain size $d_{50} = 105$ μm (Fig. 3.2). Additional grab samples in the surrounding area exhibit similar sedimentary conditions which is supported by spatially homogeneous backscatter intensity in the multibeam data (not shown).

3.2.2 *Lander deployments*

Intra-tidal hydro- and morphodynamics were observed by the autonomous seafloor observatory *SedObs* (Fig. 3.3a). The lander was developed as part of the COSYNA project[2] (Coastal Observing System for Northern and Arctic Seas) (Baschek et al., 2017). It consists of a steel frame with a 2×2 m grating platform providing space for battery power supply and the installation of sensors. The platform rests on four slim height-adjustable inclined legs to which additional sensors can be attached close to the sea bed. Weighted foot plates

1 See project website for station map and background information: www.noah-project.de
2 www.hzg.de/institutes_platforms/cosyna/index.php.en

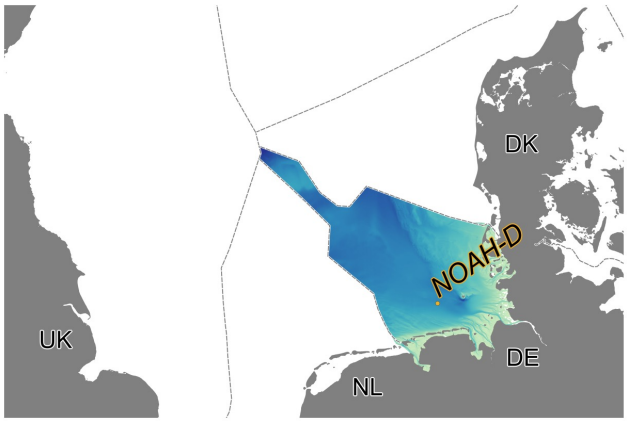

Figure 3.1: Overview map with the location of station NOAH-D in the German Bight.

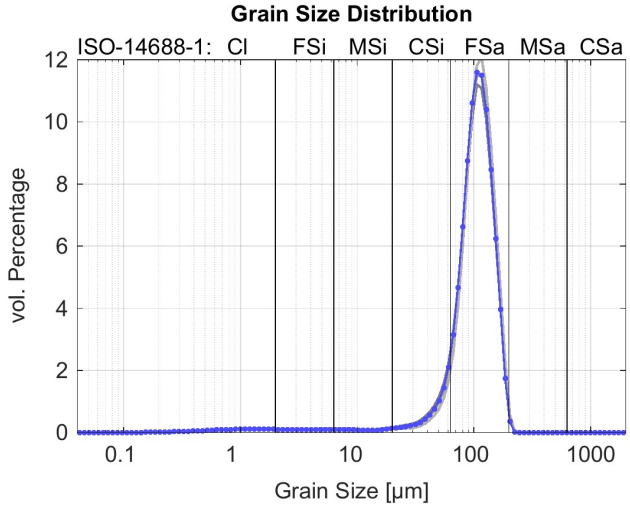

Figure 3.2: Grain size distribution and classification from Coulter laser diffractometer analysis of Shipek grab sample taken at deployment site. Gray curves in the background from grab samples in the surrounding area are shown to indicate spatially homogeneous sedimentology.

provide stable stand, prohibit subsidence and reduce scouring around the legs. For the application described here, the measurement platform was approximately 2 m above the sea floor to minimize distortions of the near-bed velocity profile. The instrumentation comprises optical and acoustic sensors for the measurement of hydrodynamics, small scale bathymetry and environmental conditions such as water temperature, salinity and turbidity. The lander is deployed from shipboard with the help of a launching frame and is recovered by acoustic release of floating buoys.

Minimization of interference with the system under investigation was a key factor in the design process of the lander as a benthic observatory. In contrast to tripod frames, the four-legged structure allows free flow between the legs. During the launch of the lander the heading is monitored to ensure orientation in alignment with the dominant bottom current direction with the help of a tail-fin on the launching frame (Fig. 3.3a).

Bathymetry data were checked for the development of scour in vicinity but such effects were not observed. Flow velocity and turbulence data were evaluated for possible influence by the lander frame or by other devices and removed if any influence was detected (Amirshahi et al., 2016).

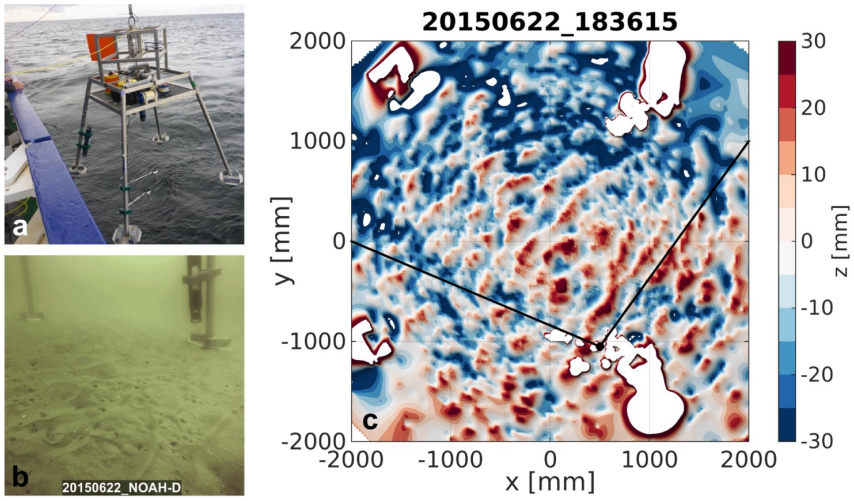

Figure 3.3: (a) Deployment of autonomous sea floor observatory *SedObs*. (b) Underwater photo showing rippled seabed. (c) Cropped sonar image with ripples and lander foot plates visible in the small scale bathymetry. Plane coordinates (x, y) are centered on sonar transducer and elevation z is given as zero-mean. The position and field of view of the camera in (b) are indicated by a black dot and black lines.

3.2.3 *Devices and data*

The devices used in this study are summarized in Table 3.1. An ADCP (Teledyne RDI Workhorse Rio Grande 1200 kHz) was used to record the near-bed velocity profile below the lander. The along-beam resolution of the downward-looking ADCP was 0.1 m and the instrument sampled at a frequency of 1 Hz. Additionally, two acoustic Doppler velocimeters (ADVs) (Nortek Vector ADV) recorded point-wise velocity data at two levels (0.12 m and 0.45 m above seabed) with a sampling frequency of 32 Hz. In combination with the pressure signal recorded, the velocity data was used to calculate wave parameters using the PUV method (e.g. Mudge and Polonichko, 2003).

The small scale bathymetry below the lander was recorded by an 1 MHz 3D acoustic ripple profiler (3D-ARP; Marine Electronics Ltd. (2004); Bell and Thorne (2007)). Its pencil-beam sonar transducer with an effective beam width of 1.8° is mounted on a rotating and tilting mechanism in an oil-filled pressure housing. In a stepwise procedure, the sonar is tilted through a preset arc in 0.9° steps, recording along-beam echo intensities from the water column for every ping (Fig. 3.4a). After completing one swath, the transducer is rotated by 0.9° about the vertical axis and tilted to the arc starting angle to record the next swath. For our applications, the swath arc was limited to 120° because

Table 3.1: *SedObs* lander sensors, measured parameters and sampling rates.

Sensor	Parameter	Sampling rate
ADCP 1200 kHz ↓	Flow velocity (profile) $\vec{u}(z)$	1 Hz
2×ADV	Flow velocity (point), Wave parameters	32 Hz
3D-ARP	Bathymetry x, y, z	$^1/_{12}$ min.
CTD	Conductivity, temperature, pressure (C, T, P)	1 Hz
Digital camera	Underwater photos (first 90 min. of deployment)	0.1 Hz

for grazing angles $\gamma < 30°$ the energy backscattered to the sonar transducer rapidly decreases and the bed echo cannot be detected reliably against background noise. With the sensor installed 1.8 m above the seafloor, a circular area of 6.2 m diameter is covered by the scans. With such settings a full bathymetry scan can be acquired in 11:50 minutes, therefore the scan interval, i.e. the sampling rate of the sonar, was set to 12 minutes. The raw echo intensity data were stored in camera raw format (rw2) with an ASCII header containing sensor settings and meta data and a binary data section listing echo intensity values of successive samples, pings and swaths.

In a morphodynamically active environment, the sampling rate of the bathymetry must be faster than the rate of change of the morphology. Furthermore, as the bathymetry scans are not instantaneous snapshots but rather require a certain time to be recorded, consistency within the scanning period needs to be guaranteed. Although not discussed here in detail, bedform migration with displacement rates of up to 3 cm h^{-1} were observed. At a sampling rate of five scans per hour, this results in a maximum migration distance of 0.6 cm between two successive scans which is lower than the selected resolution of the gridded small scale bathymetries.

3.2.4 *Bed detection methods*

The raw 3D-ARP data are available as a three-dimensional matrix $\vec{S}^{i \times j \times k}$, containing the echo intensities for the number of i samples along the beam, j pings along a swath and k swaths of a full scan. The general form of the echo recorded in individual pings exhibits a high echo level close to the sonar transducer due to ringing. This part of the signal within the near range of the sonar is blanked before further processing. With increasing range from the transducer, the backscattered echo level declines due to signal losses to reverberation and scattering in the water column. At bed range, a steep increase to a maximum level can be observed, followed by a more gentle decline towards a constant background noise level. Averaged echo shapes for variable grazing angles are illustrated in Figure 3.5.

To reduce noise, the raw echo signals are smoothed by a five-point moving average in along-beam direction. The resulting echo intensity profiles are evaluated for the max-

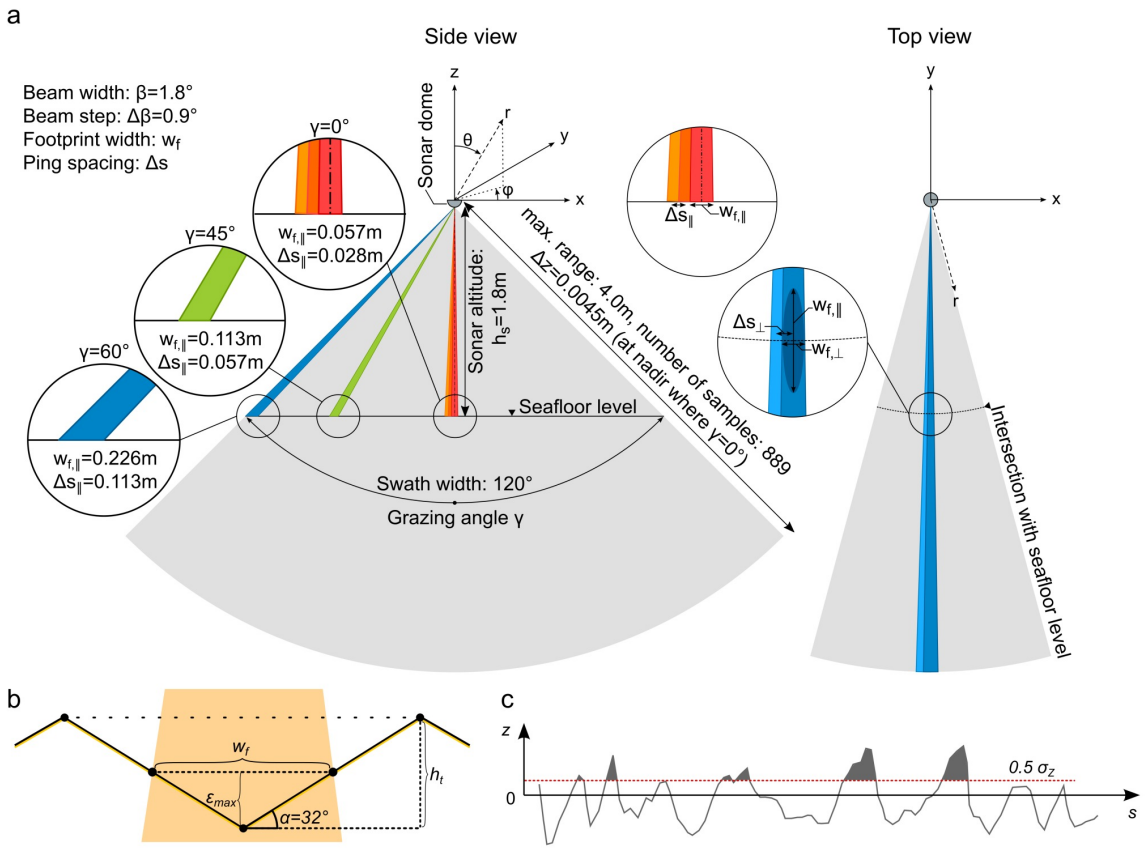

Figure 3.4: (a) Definitions of sonar coordinates and beam footprints on an average seafloor level at different grazing angles. (b) Estimation of maximum error in ripple through depth due to picking of highest elevation within the sonar footprint. (c) Generation of binary image from bathymetry using half the standard deviation of the elevation as cutoff threshold.

imum echo, as the bed usually contributes the strongest reflector. The simplest method of bed detection is therefore to pick the maximum echo in the smoothed ping data. However, as marine life or other instrumentation in the sonar beam may also contribute strong reflectors, the water column echo was only evaluated within a certain depth range around the expected bed level.

Threshold-level methods for bed detection in echo data acquired by similar sonars have been implemented by Smyth and Li (2005) and by Lefebvre (2009). These authors detect the bed level at the depth in which a certain percentage of the maximum ping-wise echo intensity l_{max} is exceeded: $l_p \geq 0.6\ l_{\max}$ (Smyth and Li, 2005) and $l_p \geq 0.8\ l_{\max}$ (Lefebvre, 2009). These approaches are extended to account for the widening of the along-beam target shape with increasing grazing angles γ (see Fig. 3.5). Therefore, a threshold level as a function of the grazing angle is introduced:

$$l_p = \left[1 - \sqrt{(\cos\gamma)}\right] l_{\max} \tag{3.1}$$

with values ranging from $l_p = 0.7$ at the outer swath beams to $l_p = 1.0$ at the central vertical (nadir) beam.

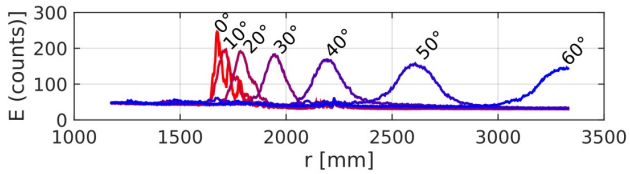

Figure 3.5: Echo intensities over range derived from scan averaged water column echoes for different grazing angles.

Apart from the threshold level, further methods using the first and second along-beam derivatives of the echo intensity, echo gradient and echo curvature, were tested. The maximum echo gradient is usually found midway between background noise level and maximum echo intensity in the rising slope of the signal, given that it is resolved by a sufficient number of samples. The maximum in echo curvature represents the onset of the rising slope of the echo intensity signal.

The last approach for bed detection tested was the cross-correlation with an idealized bed echo model. The bed level is found at the along-beam range where the cross-correlation of the recorded ping echo and the echo model is maximized. Bell and Thorne (1997) designed a model of the bed echo (target) represented by a sine wave accounting for the acoustic pulse length and the incident angle between sonar lobe and seabed. The model echo is cross-correlated with the echo profiles and the index of maximum correlation denoting the best fit between echo model data determines the bed range. To account for variable environmental conditions in the echo data at hand, 200 samples (180° in 0.9° steps) of echoes for every grazing angle were taken into account for every scan. Averaging the individual pings over all swath angles, a data derived echo model without the need to design an idealized echo shape was obtained.

3.2.5 *Coordinate conversion and gridding*

The beam coordinates of the detected bed level are computed considering the sound velocity and two-way travel time of the sonar signal yielding an along-beam range. Together with the tilt and rotation angles for the corresponding ping and swath, the bed level is described in spherical coordinates (r, θ, φ) which then are transferred to Cartesian coordinates (x, y, z) (see Fig. 3.4a).

The along-beam resolution can be estimated from the overall beam range and the number of samples. Typical settings are a beam range of $r_{max} = 4$ m and $n_i = 889$ samples; the resulting vertical resolution for the nadir beam is $\Delta_z = 0.0045$ m. The horizontal resolution is controlled by the area of the sonar footprint as well as tilt and rotation steps. With a beam angle of $\beta = 1.8°$ (±3 dB points conical, Marine Electronics Ltd. (2004)) and a sonar height of $h_s = 1.8$ m above the seabed, the nadir beam ensonifies a circular area of $w_f = 0.056$ m diameter. At the maximum grazing angle $\gamma_{max} = 60°$, the total area ensonified over the echo pulse length has a width $w_{f,\|} = 0.226$ m in the

swath plane. The along-swath beam spacing is set to $\Delta\beta_{\parallel} = 0.9°$ steps, resulting in an along-swath spacing of $\Delta s_{\parallel} = 0.028$ m at nadir (γ =0°), $\Delta s_{\parallel} = 0.057$ m at $\gamma = 45°$ and $\Delta s_{\parallel} = 0.116$ m at the maximum grazing angle (γ =60°). The across-swath beam spacing is controlled by the rotational step of $\Delta\beta_{\perp} = 0.9°$. With the intersection of the outermost beam at γ =60° with the seafloor at $s_{max} = \tan\gamma_{max} \cdot h_s = 3.118$ m it results in a maximum step of $\Delta s_{\perp} = s_{max} \cdot \tan\Delta\beta_{\perp} = 0.049$ m. With $\beta = 2 \cdot \Delta\beta$, the scross-swath footprint width is double the across-swath beam spacing.

As the acoustic pulse is most likely reflected by the highest elevation within the sonar footprint, the depth of troughs may be underestimated (Fig. 3.4b). Assuming a triangular bedform shape and a maximum slope equal to the angle of repose of sand $\alpha = 32°$, the maximum error in underestimating through depths yields $\varepsilon_{max} = 0.5 \cdot w_f \cdot \tan\alpha = 0.017$ m at nadir and $\varepsilon_{max} = 0.070$ m at the outermost beam in our configuration. As ripple troughs are usually more flat, the error is expected to be less pronounced. With a typical aspect ratio (ripple height over length) $\psi = 0.1$ much lower than the angle of repose, the maximum error reduces to $\varepsilon_{max} = 0.003$ m at nadir and $\varepsilon_{max} = 0.011$ m for the outermost ping.

For comparability among successive scans, the scattered data points were gridded resulting in DEMs with consistent grid cells (Fig. 3.3c). With a minimum along-swath sonar step size of 0.028 m at nadir, a grid horizontal grid resolution of $\Delta x = \Delta y = 0.025$ m was selected to maintain the high resolution in the center of the recorded bathymetry even if the effective resolution decreases with increasing beam footprint and spacing towards higher grazing angles.

In the last processing step, the bathymetry is cropped to the central area of 2 m by 2 m for further evaluation of bedform characteristics. This limitation is made because the area outward of the lander legs is shadowed from the sonars field of view and the maximum grazing angle for the cropped area is limited to $\gamma = 30°$, reducing the effects of increasing beam spacing and sonar footprint. To better distinguish local ripple features, the global trend of the larger scale surrounding bathymetry is computed from the average bathymetry of all scans of a deployment and removed. The resulting residual zero-mean bathymetry is evaluated by the following methods.

3.2.6 *Ripple geometry*

Ripple geometry can be described by the orientation φ of crests lines in the horizontal plane and the cross-sectional dimensions; height η, wave length λ and aspect ratio $\psi = \eta/\lambda$. The dominant forcing can be distinguished from ripple cross-sectional shape: In contrast to symmetric wave ripples, current ripples exhibit a steeper downstream (lee) slope and a more gently inclined upstream (stoss) slope. A classification for a number of transitional forms between pure wave and current ripples is given by Amos et al. (1988). The ratio of the stoss and lee slope lengths (symmetry index) can be used to identify

bedform orientation with regard to the dominant forcing and indicate migration in this direction (Knaapen, 2005).

The geometry of the ripples is extracted from the gridded bathymetry datasets. First, the crest-transverse orientation θ of the ripple field is derived: The gridded datasets are transferred into binary image matrices using a threshold equal to half the standard deviation of the global elevation $z_{tr} = 0.5\,\sigma_z$ (Fig. 3.4c). The binary images are processed using 8-connected neighborhoods to identify crest areas of individual bedforms. The detected objects are represented by ellipses of equal area. Small and circular objects are removed by criteria for minimum area and ratio of the ellipses semi-axes. The average orientation of the remaining objects is used as characteristic ripple orientation. Figure 3.6 shows an example for the cropped bathymetry, the binary image with detected ripple orientation and the corresponding distribution of crest-perpendicular orientation in the polar histogram. The precision in orientation detection throughout successive scans, even for inactive bedforms is in the order of 10°. To avoid abrupt changes in the subsequent computation of bedform heights and lengths, the ensemble average ripple orientation is computed for the complete deployment period, given that it does not change significantly over time. Afterwards, the scans are rotated using the average ripple orientation and re-interpolated to the original Cartesian grid for extraction of ripple dimensions using the following three methods:

1. Statistical method ($\eta_{m,s}$)
   The first is a statistical estimate using the distribution of bed elevations. The standard deviation of elevation, multiplied by $k = 2\sqrt{2}$ was used to estimate bedform heights η_s by Traykovski et al. (1999) and Smyth and Hay (2002). This method is usually employed to compute root mean square wave height from water level records and assumes sinusoidal bedform cross sections.

2. Image extrema method ($\eta_{m,i}$)
   The second method finds local extrema in the 3D bathymetry as grid cells surrounded by cells of lower (crest) or higher elevation (trough), similar to finding extreme pixel values in raster images. The averaged ripple η_i height is computed from the range between crests and troughs.

3. Transect method ($\eta_{m,t}$, $\lambda_{m,t}$)
   For the third method, transects are defined perpendicular to the crest orientation and evaluated for local extrema (crest and trough) between zero up- and down-crossings. The computed bedform height η_t is the average range between the elevations of detected maxima and minima per transect. Apart from height, bedform length λ_t is also computed by the transect method as the average along-transect distance between two successive crests. With the DEM spacing and cropping window size used, a total of 80 transects of 2 m length are evaluated.

Methods for the evaluation of bedform dimensions can be divided in continuous and discrete approaches. While statistical methods evaluate the continuum of the bathymetry,

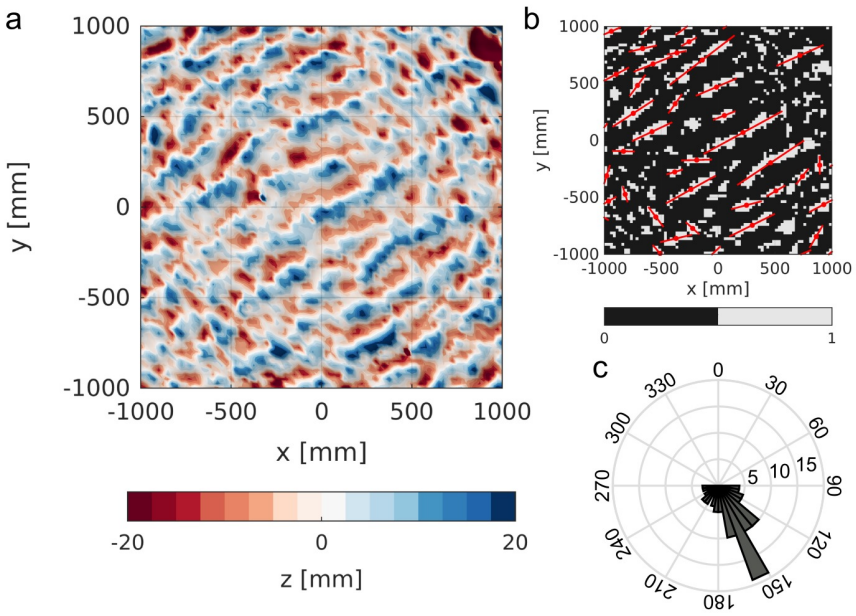

Figure 3.6: (a) Small scale bathymetry cropped to the central 2×2 m below the sonar. (b) Overlay of detected objects in 8-connected neighborhood on binary image with a threshold of $0.5\sigma_z$. Object centers and major axes are marked in red. (c) Polar histogram of ripple crest-perpendicular orientation in degrees from North with percentage of total number of objects on the radial axis.

discrete or direct methods provide dimensions of a limited number of features detected with a given threshold for height and in case of the transect method also length. As described by Friedrich et al. (2007), the disadvantage of discrete methods is the sensitivity of measured dimensions to the thresholds selected. As an alternative, ripple orientation and length can also be determined from spectra obtained from the 2D discrete Fourier transform (DFT) of the gridded bathymetry (Traykovski, 2007; Lefebvre, 2009; Nelson and Voulgaris, 2014) or from 2D autocorrelation. However, these methods require a certain regularity of the bedforms and were not applied here. Especially when primary and secondary bedforms are present, a carefully calibrated direct approach may be more useful than a statistical approach (van der Mark et al., 2008; Ernstsen et al., 2010). The disadvantage of direct approaches is that the selection of thresholds and filter window sizes introduces a certain subjectivity and influences the resulting statistics of bedform dimensions. The advantage of direct methods is that they capture a range of bedform dimensions and therefore yield not only average values for the overall bathymetry but also a distribution of dimensions allowing for a statistical evaluation.

3.2.7 *Predictors for ripple dimensions*

A number of predictors for wave ripple geometry exists in literature and few for current ripples. A recent overview and evaluation of the performance of wave ripple predictors with an extensive dataset from lab and field experiments can be found in Nelson et al.

(2013). Soulsby and Whitehouse (2005) present a literature review of predictors for wave, current and combined ripples and Soulsby et al. (2012) recently developed a combined, time-evolving predictor. After determining the dominant forcing, two formulations for wave or current ripples are employed to determine equilibrium heights which are then used in an exponential relaxation in the time-stepping procedure (Soulsby et al., 2012).

In contrast to comparative studies as e.g. Nelson et al. (2013) we choose a number of common predictors and compare their range to the range of measured ripple dimensions by the different methods described above.

The following ripple predictors are applied with a given median grain size and hydrodynamic data and compared to measured dimensions. The traditional current ripple predictors of Yalin (1964, 1985) (Ya64, Ya85) for length and Flemming (1988) (Fl88) and Baas (1994) (Ba94) for ripple height were selected as they are widely used. For mixed forcing conditions, the recent wave and current ripple predictors of Soulsby et al. (2012) (So12w, So12c) are used by defining the prevailing dominant forcing and selecting the appropriate predictor.

3.2.7.1 *Current ripples*

Current generated ripple dimensions are usually described as independent of hydrodynamic parameters but scaling with grain size and immersed weight only. An early work by Yalin (1964) (Ya64) predicts current ripple length as

$$\lambda_c = 1000 \cdot d_{50} \tag{3.2}$$

and was later revised including additional data (Yalin, 1985) (Ya85) in the form

$$600 \cdot d_{50} \leq \lambda_c \leq 2000 \cdot d_{50} \tag{3.3}$$

While the ratio between bedform height and length may be derived using an empirical relation with the best fit to a large dataset from laboratory and field data by Flemming (1988) (Fl88)

$$\eta_c = 0.0677 \cdot \lambda_c^{0.8098} \tag{3.4}$$

and the maximum bedform height as

$$\eta_{c,\max} = 0.16 \cdot \lambda_c^{0.84} \tag{3.5}$$

Baas (1994) (Ba94) gives bedform height as

$$\eta_c = 18.16 \cdot d_{50} \lambda_c^{0.84} \tag{3.6}$$

Building on this work, Soulsby et al. (2012) (So12c) predict maximum dimensions of current ripples as follows. For height they obtain

$$\eta_{c,\max} = d_{50} \cdot 202 \cdot D_*^{-0.554} \tag{3.7}$$

and length yields

$$\lambda_{c,\max} = d_{50} \cdot (500 + 1881 \cdot D_*^{-1.5}) \tag{3.8}$$

Equation 3.7 and Eq. 3.8 are valid in a range of $1.2 < D_* < 16$, where D_* is the dimensionless grain size

$$D_* = \left[\frac{g(s-1)}{\nu^2}\right]^{1/3} d_{50} \tag{3.9}$$

with the density ratio of sediment and water $s = \rho_s/\rho_w$, gravitational acceleration g and kinematic viscosity of water ν. These maximum ripple dimensions are reduced during wash-out conditions and existing ripples are completely eliminated by sheet flow. The different flow regimes are delineated by respective critical Shields parameters. In the measurements presented here, supercritical Shields parameters for bed load transport were found but they remained far below wash-out and sheet flow conditions, thus only the maximum ripple dimensions are used here.

3.2.7.2 *Wave ripples*

Predicted wave ripple dimensions commonly scale with a dimensionless number derived from wave parameters in relation to sediment grain size and immersed weight. Soulsby et al. (2012) (So12w) found that the use of the ratio of wave orbital amplitude and median grain size $\Delta = A/d_{50}$ as independent variable gives the best representation of a large dataset of measured ripple dimensions from flume and field studies. They use the following empirical predictors for wave induced ripple wave length

$$\lambda_w = \left[1 + 1.87 \times 10^{-3}\Delta(1 - \exp(-(2.0 \times 10^{-4}\Delta)^{1.5}))\right]^{-1} A \tag{3.10}$$

and height

$$\eta_w = 0.15\ (1 - \exp(-(5000/\Delta)^{3.5}))\ \lambda_w \tag{3.11}$$

Earlier works as cited in Li and Amos (1998) based on flume and field data predict wave ripple dimensions as follows. Grant and Madsen (1982) (GM82) predict height as

$$\eta_w = 0.22A(\theta_w/\theta_{cr})^{-0.16} \tag{3.12}$$

and length as

$$\lambda_w = 6.25\eta(\theta_w/\theta_{cr})^{0.04} \tag{3.13}$$

Li et al. (1996) (Li96) give

$$\eta_w = 0.101A(\theta_w/\theta_{cr})^{-0.16} \tag{3.14}$$

for height and

$$\lambda_w = 3.6\eta(\theta_w/\theta_{cr})^{0.04} \tag{3.15}$$

for length. In Eq. 3.12 – 3.15, θ_w is the wave-induced and θ_{cr} the critical Shields parameter.

3.2.8 *Hydraulic roughness*

When bedform dimensions are known, their effect on the flow can be assessed as a hydraulic roughness length using empirical relations (Li and Amos, 1998; Lefebvre et al., 2016). The impact of form roughness due to bedforms is important for numerical models as it can exceed the effect of grain roughness k_g by orders of magnitude (e.g. Soulsby, 1997). A widely used (bed-)form roughness predictor is defined by van Rijn (1984)

$$k_{s,f} = 1.1 \cdot \eta \cdot (1 - e^{-25\eta/\lambda}) \tag{3.16}$$

Another common form of roughness length derived from ripple dimensions is $k_f = f(\eta^2/\lambda)$ with height in a power of two over length (see overview in Lefebvre et al., 2011) with varying scaling scaling factors. Soulsby (1997) presents it as follows

$$z_{0,f} = a_r \frac{\eta^2}{\lambda} \text{ (with scaling factor typically } a_r = 1). \tag{3.17}$$

3.3 RESULTS

3.3.1 *Hydrodynamics and sediment mobility*

Hydrodynamic and meteorological data from the measurement site for a period of 36 hours are displayed in Fig. 3.7. Over the tidal cycle, water depths range from 34 m at low tide to 37 m at hight tide at the position of the lander. Current velocities measured by the lower ADV 0.12 m above the seabed range from 0.1 to 0.3 ms^{-1}. The depth-averaged flow velocities measured by the downward-looking ADCP are 25% higher. The wind direction changes from westerly winds with speeds of up to 15 ms^{-1} during the first day of the deployment through North to Easterly directions with speeds of 5–15 ms^{-1} on the second day. Wave parameters were calculated using the velocity and pressure data from the lower ADV. Significant wave heights range from below 0.5 m in the first half of the measurement up to 2.5 m in the second half with a peak period between 8 s and 10 s.

To relate the hydrodynamic forcing to sediment mobility, Shields parameters were computed for wave (θ_w) and current (θ_c) forcing and the critical Shields parameter (θ_{cr}) was defined for the given median grain size (Fig. 3.8a). For the first 18 hours of the deployment, conditions with excess shear stress were observed only during peak flood and ebb currents. Wave-induced excess shear stress conditions are reached for a period of 4 hours starting around 15:00 h local time on the second day, followed by a period with current-induced excess shear stress lasting for around 4 hours during flood current around 22:00 h local time.

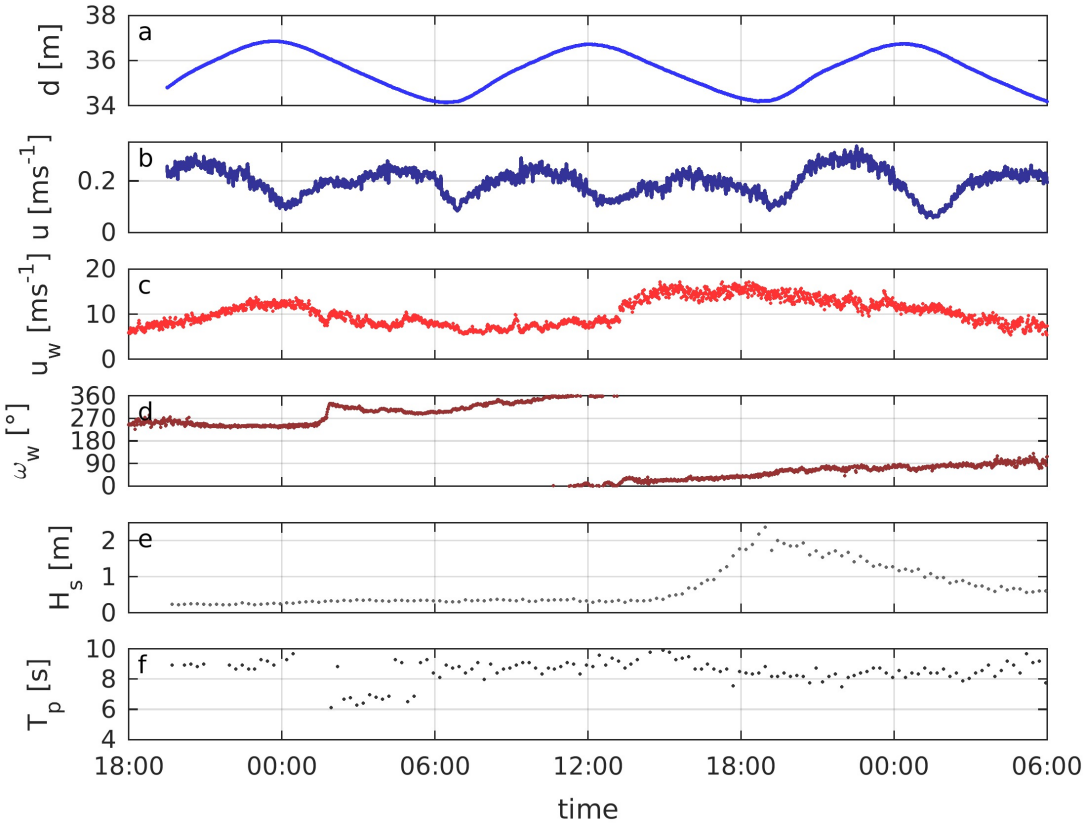

Figure 3.7: Hydrodynamic conditions at station NOAH-D, 20–22 March 2015. (a) Water level, (b) flow velocity at a height of 0.12 m above seafloor (c) wind speed and (d) direction and (e) significant wave height and (f) peak period.

3.3.2 *Bed detection*

An inter-comparison of the different methods for bed detection shows that all threshold level methods reproduce similar characteristics of the rippled seabed (Fig. 3.9). They mainly differ in the absolute level of average depth. The maximum echo gradient, maximum echo curvature and 60% maximum echo method (Smyth and Li, 2005) provide a median depth around 0.025 m higher than the median depth computed by the remaining methods. Additionally, the 60% max. method exhibits a slight dependence on the grazing angle and returns a bowl-shaped bathymetry (see Fig. 3.9b). The comparison of the different bed detection methods revealed that picking the maximum amplitude of a smoothed echo within a certain range of the expected bed level provides the most efficient approach. Level threshold methods do not enhance the bathymetry DEMs and echo gradient and curvature methods are less robust. Bed picking by cross-correlation with an echo model is more computationally expensive than the level threshold methods but it accounts for the shape of the complete bed echo rather than depending on a single value. However, the bed echo model approach is limited to flat seabeds and a perfectly horizontal sonar with a nadir beam normal to the bed, where only the grazing angle determines the incident angle between sonar lobe and bed. For rippled seabeds however,

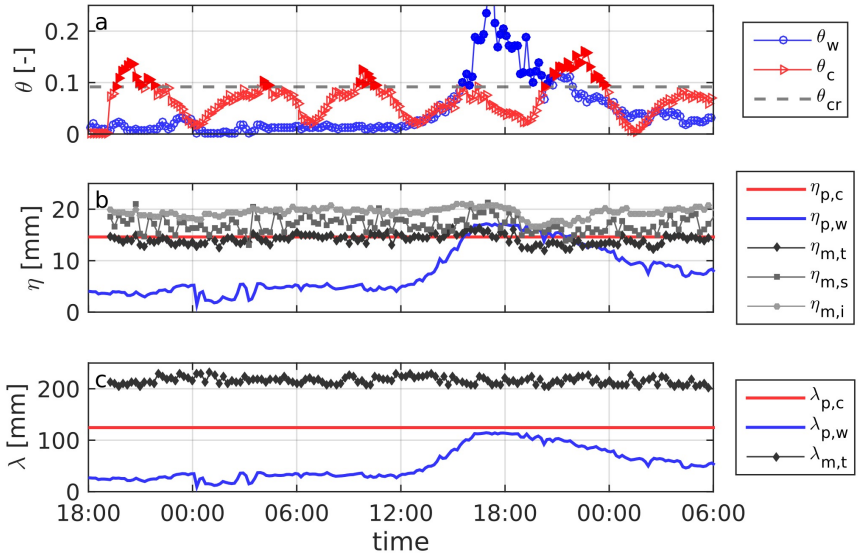

Figure 3.8: (a) Shields parameters for wave orbital velocities θ_w, tidal current θ_c and critical Shields parameter θ_{cr}. During supercritical conditions ($\theta > \theta_{cr}$), filled markers indicate the dominant forcing. (b) Evolution of ripple height and (c) wave length compared to predicted equilibrium dimension for wave and current forcing as given by Soulsby et al. (2012). Indices in the legends of (b) and (c) indicate: p-predicted, m-measured, c-current, w-wave, t-transect, s-statistical and i-image extrema.

the exact morphology within the sonar footprint needs to be known a priori to adapt the echo shape to the true incident angle. Echo model methods may therefore rather serve as enhancement of the bathymetry computed by a threshold level method in a first run.

3.3.3 *Ripple dimensions*

Ripples with a mean wave length of $\lambda_{m,t} = 0.215$ m and a mean height of $\eta_{m,t} = 0.013$ m (aspect ratio $\psi = 0.06$) are measured using the transect method (Fig. 3.8b,c). The largest measured bedform heights of 0.019 m are obtained by the statistical method followed by 0.017 m by the image extrema methods whereas the evaluation of extrema in individual grid transects yields the lowest absolute heights of 0.013 m (Fig. 3.10a). The dimensions remain stable for the first 24 hours of the deployment and the bedforms are considered inactive during this period as $\theta_c < \theta_{cr}$. Thus, the scatter of measured dimensions is used to quantify the precision of the methods used for their detection. With the increasing flood current velocities and wave action on the seafloor from 24 hours onwards, the ripple height decreases by 0.004 m over a period of 2 hours and increases to the initial height over the following 6 hours with increasing tidal current velocity. No significant changes in ripple wave length can be observed. In terms of height evolution the trend of change of ripple height on the second day of the deployment is captured by all three methods. The statistical method returns the most robust results resulting in less scatter between successive measurements.

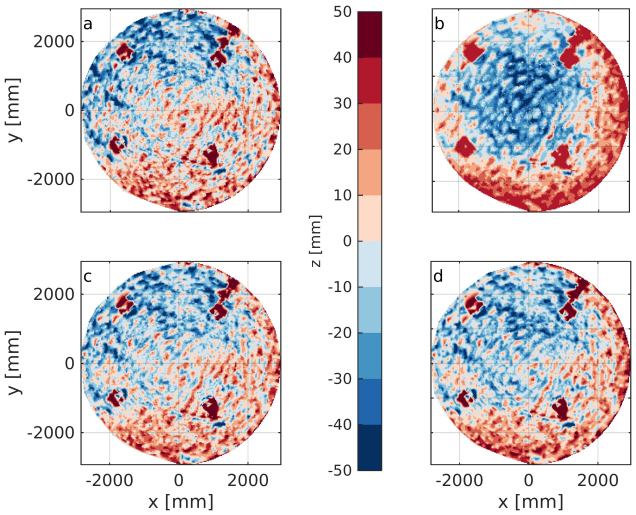

Figure 3.9: Comparison of bathymetries obtained by different bottom-picking methods. (a) Maximum echo, (b) 60% max. echo (Smyth and Li, 2005), (c) 80% max. echo (Lefebvre, 2009) and (d) grazing angle related coefficient of max. echo. Elevation z is given as zero-mean.

All methods of bedform detection produce values that fall within the range between mean (0.011 m) and maximum (0.024 m) bedform height as given by Fl88. Following Ba94, the predicted current ripple height equals 0.015 m. Predicted current ripple dimensions using Eq. 3.7 and 3.8 from Soulsby et al. (2012) result in $\eta_{p,c} = 0.015$ m and $\lambda_{p,c} = 0.124$ m. Predicted wave ripple dimensions from Eq. 3.10 and 3.11 follow the evolution of wave orbital velocities, however waves are expected to be dominant only where $\theta_w > \theta_c$ (Fig. 3.7a: Day 2, 15:00 h – 19:00 h). During this period, the maximum predicted wave ripple dimensions are $\eta_{p,w} = 0.017$ m and $\lambda_{p,w} = 0.115$ m. Wave ripple height predicted by Li96 results in 0.015 m while the height of wave (orbital) ripples by GM82 results in 0.032 m.

Bedform wave lengths derived based on the transect method amount to $\lambda_{m,t} = 0.215$ m (Fig. 3.10b). The mean length for current ripples predicted by Ya64 results in 0.105 m and the range predicted by the relations of Ya85 yields 0.063 m – 0.210 m. Wave ripple length predicted by GM82 yields 0.205 m while the length predicted by Li96 results in 0.054 m and lengths predicted by So12 amount to $\lambda_{p,c} = 0.124$ m for currents and $\lambda_{p,w} = 0.109$ m for waves.

The discrete transect method allows a statistical evaluation of the distribution of measured dimensions. The evolution of dimension histograms along with statistical parameters for bedform height and length are displayed in Fig. 3.11. Due to the relatively large gridding cell size of 0.025 m the distribution of lengths is rather narrow and mostly varying between two cells (Fig. 3.11b). The standard deviation of ripple height increases from 0.005 m to 0.007 m throughout the first day and decreases again to 0.004 m with the wave event (18:00 h – 21:00 h on the second day). This may indicate that the bedforms become more regular due to the pronounced dominance of waves in this period.

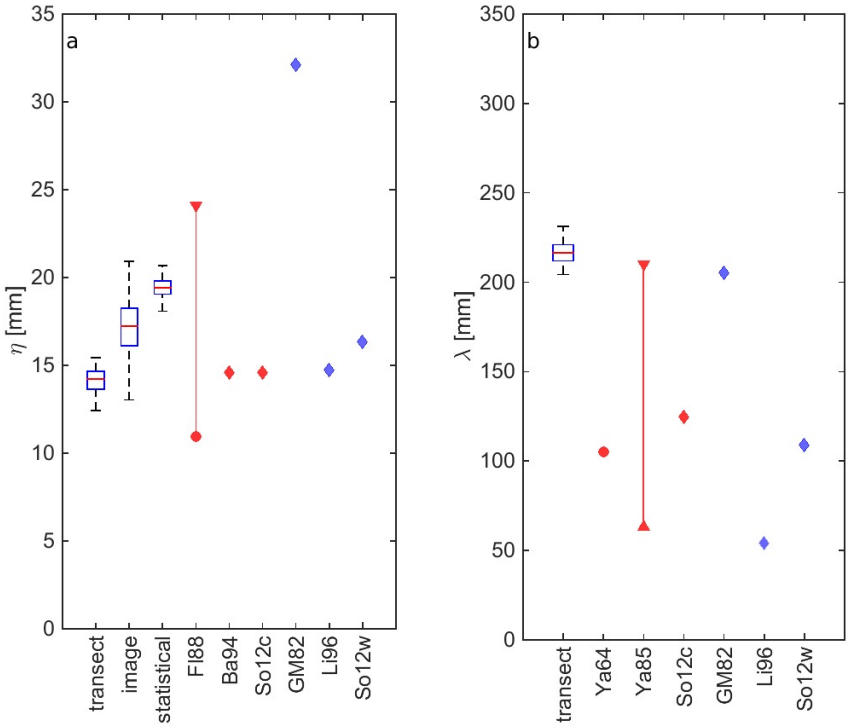

Figure 3.10: Box plots of the precision of measured dimensions during stationary conditions and accuracy in comparison with predicted equilibrium dimension for wave and current dominated conditions using the equations 3.2–3.15. (a) Bedform height, measured by 2D transect wise extrema, 3D image extrema and statistical method. Markers indicate predicted ripple heights using the expressions for currents from Flemming (1988), Baas (1994), Soulsby et al. (2012) and for waves from Grant and Madsen (1982), Li et al. (1996) and Soulsby et al. (2012). (b) Bedform wave length measured from 2D transects. Markers indicate predicted ripple length using the current expressions from Yalin (1964, 1985) and Soulsby et al. (2012) and the wave expressions from Grant and Madsen (1982), Li et al. (1996) and Soulsby et al. (2012). In box plots, red line denotes median, blue box indicates 25^{th} and 75^{th} percentiles and dashed lines extend to extreme values.

3.3.4 *Hydraulic roughness*

Roughness lengths $z_{0,f}$ and Nikuradse's equivalent sand roughness $k_{s,f}$ resulting from the different ripple heights and the length from the transect method are summarized in Tab. 3.2 along with reduction factors with regard to the statistical method. Nikuradse's roughness $k_{s,f}$ (Eq. 3.16) returned using ripple dimensions from the image extrema method is reduced by a factor of 0.8 and by a factor of 0.6 for the transect method. Due to the squared ripple height in Eq. 3.17, the difference between the methods is even more pronounced for roughness height $z_{0,f}$ which returns reduction factors of 0.71 and 0.47 for image extrema and transect methods, respectively.

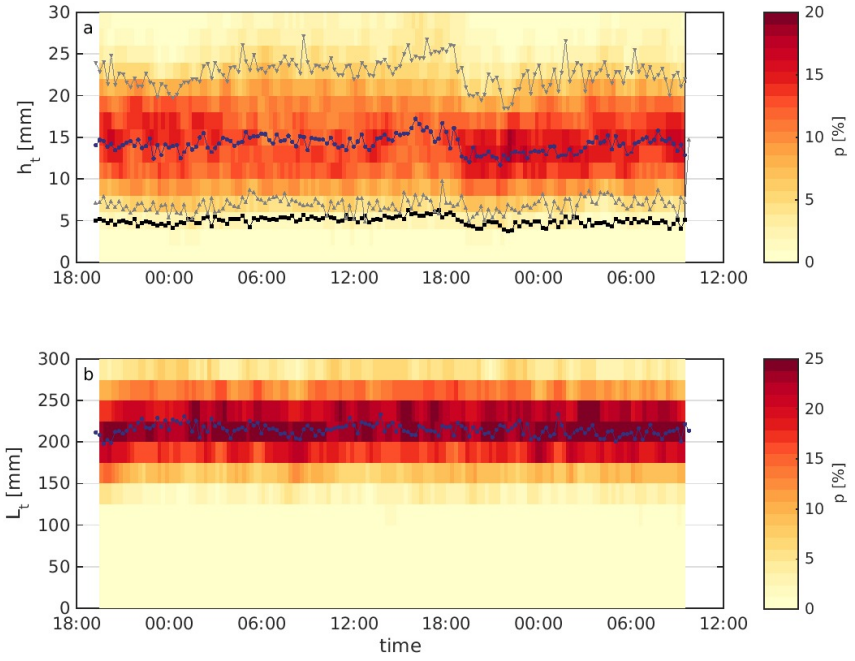

Figure 3.11: Evolution of histograms and statistics of bedform dimensions measured by the transect method. (a) Bedform height and (b) bedform wave length. Blue dot markers indicate median, black squares indicates the standard deviation and gray triangles indicate 5^{th} and 95^{th} quantiles. Due to the large cell size and narrow distribution of bedform lengths, the latter are only displayed for heights.

Table 3.2: Roughness lengths for measured ripple dimensions using Eq. 3.16 and 3.17.

Method	statistical	image extrema	transect
$k_{s,f}$ [-] (Eq. 3.16)	0.01861	0.01486	0.01115
reduction with regard to stat. method	1.00	0.80	0.60
$z_{0,f}$ [m] (Eq. 3.17)	0.00168	0.00119	0.00079
reduction with regard to stat. method	1.00	0.71	0.47

3.4 DISCUSSION AND ASSESSMENT

3.4.1 *Methods for dimension measurement*

Only one method is shown for the analysis of ripple orientation and length from sonar data, but three methods can be compared for the calculation of ripple heights. The statistical method (e.g. Traykovski et al., 1999) assumes a two-dimensional sinusoidal ripple field and computes its root mean square height. The second method picking regional extrema in the bathymetry only measures the height of a limited number of features. The evaluation of transects makes use of the complete scan at the grid resolution and averages over a larger number of regional extrema along the transects.

If bedform dimensions are computed from transects perpendicular to bedform crests, the result depends on the lateral position of the transect. As can be seen in Fig. 3.3b, ripples found in the field often exhibit curved crest lines of limited length rather than being purely two-dimensional features. Furthermore, the instantaneously observed rippled seabed always holds a history of varying dominant forcing drivers, magnitudes and directions. Transitional states may comprise newly formed active ripples superimposed on decaying relict ripples with different orientation. Within a three-dimensional field, any selected transect will cut across individual ripples at an arbitrary position with respect to its lateral elevation profile. The ripple height can only be regarded as meaningful by statistically evaluating multiple transects. This is underlined by van der Mark et al. (2008), who state that bedforms are far from regular features that can be easily described using mean values, even in laboratory flume experiments with uniform sediment and stationary flow conditions.

3.4.2 *Precision of measurement*

To assess the *accuracy* of the measurement, a priori known topography under controlled laboratory conditions would be required. This cannot be achieved under field conditions. However, the *precision* of the different methods described here, i.e. the repeatability of a dimension measurement, can be estimated from the inter-comparison of the different methods and the temporal variability of the dimensions obtained from each individual method during stationary, inactive periods.

The different methods for ripple height measurement yield different absolute values but the magnitude of the change in height is captured by all three methods. For a better assessment of the precision of the methods, bedform dimensions from the first 18 hours of the deployment were summarized in box plots exhibiting the distribution of ripple height and length during stationary conditions. The results shown in Fig. 3.10 indicate that both ripple height and wave length can be measured with a precision smaller than 10% of their absolute dimensions, regardless of the method used. The distributions of ripple height for all three methods are negative-skewed. Judging from 25^{th} and 75^{th} percentiles, the statistical method provides the most narrow range of ripple height while image and transect extrema yield comparable ranges.

As for ripple length, both 2D cross-correlation and DFT did not prove robust thus the transect method remains. Its results fall into the wide range of lengths predicted by Yalin (1985) but is around 60% larger than lengths predicted by Soulsby et al. (2012) for wave ripples and still about 40% larger than length predicted for current ripples scaling with grain size only.

3.4.3 *Form roughness*

The overestimation of ripple height has a significant effect on the calculation of hydraulic roughness due to the fact that height is used in a power of two in common roughness predictors (see list in Lefebvre et al. (2011, 2016)). While the range of predicted heights is in good general agreement with measured average values, the S012 predictor tends to represent maximum heights of individual ripples rather than an along-crest average height given a certain three-dimensionality with varying crest elevation. If ripple height measured as average over individual transects is compared to the results from the statistical method, it is found that the latter gives values 40% larger than the transect method. This corresponds to a roughness height increase by a factor of 1.56 if the ripple dimensions are used to predict form roughness using bedform roughness height as given by Eq. 3.16 (van Rijn, 1984) and an increase of roughness height by a factor of 1.96 using the relation given by Eq. 3.17 (Soulsby, 1997).

3.5 CONCLUSIONS

An in situ setup for measuring ripple dimensions and dynamics was described, as well as several methods for processing the measured data. While the *accuracy* of the measured ripple dimensions cannot be determined without an absolute reference value, both ripple heights and wave lengths can be measured with a *precision* smaller than 10% of their absolute dimensions during inactive conditions. All data processing methods tested are consistent with regard to the ripple dimensions computed. Observed relative changes in height are in the order of several millimeters between successive scans during active periods. The dynamics of ripple dimensions obtained by any of the methods (i.e. their relative changes) can be reliably obtained and linked to changes in the forcing hydrodynamics.

The overall range of current ripple height can be predicted using the empirical relation by Flemming (1988). The current ripple predictors from Baas (1994) and Soulsby et al. (2012) and the wave ripple predictors from Li et al. (1996) and Soulsby et al. (2012) fit measured heights more closely. Measured ripple lengths compare best to the upper end of the wide range given for current ripples by Yalin (1985) and wave ripples by Grant and Madsen (1982) but are somewhat longer than lengths predicted for both wave- (Soulsby et al., 2012) and current dominated ripples (Yalin, 1964; Soulsby et al., 2012). The measured lengths of the ripples are best predicted by the upper end of the range for current ripples given by Yalin (1985) and wave ripples by Grant and Madsen (1982).

The performance of time-evolving predictors introduced by Traykovski (2007) and Soulsby et al. (2012) could not be evaluated. The predictor of Traykovski (2007) was developed for wave-orbital ripples in more energetic environments. Both predictors could not predict the small range of dynamic evolution of ripple heights in the shelf sea area.

This may also be related to the migration of the ripples due to nonlinear interaction of wave and current forcing, which is not covered by the predictors. Additionally, the migration of bedforms observed may result in the opposed trends in the development of ripple heights during the wave dominated conditions (around 18:00 h on the second day) (Fig. 3.8a).

The commonly used statistical estimation of ripple height yields heights 40% larger than average heights obtained by the transect method. This results in calculated form roughness height to increase by a factor of two. To account for the spatial variability of ripple heights, dimensions derived from transects should be considered whenever spatial bathymetry data with sufficient resolution are available.

ACKNOWLEDGEMENTS The lander setup has been supported through the project Coastal Observing System for Northern and Arctic Seas (COSYNA). Data presented here was collected by the MARUM Coastal Dynamics group. Their willingness to suffer in heavy seas is gratefully acknowledged. The authors also appreciate the support from captain and crew on R/V *Heincke*. Processed hydrodynamic ADV data were kindly provided by S.M. Amirshahi. We also thank C. Daly who helped to improve the language of the manuscript. K. Krämer appreciates the support of the BMBF funded research project NOAH – North Sea Observation and Assessment of Habitats and of GLOMAR – Bremen International Graduate School for Marine Sciences.

AUTHOR CONTRIBUTIONS C. Winter conceived the field campaigns and measurement setup on the *SedObs* lander. K.K. and C.W. collected the data during cruises HE441 and HE447 on board R/V *Heincke* with support of the Coastal Dynamics group at MARUM. K.K. performed the data processing and analysis the data. K.K. wrote the manuscript in close discussion with C.W..

4

THE RELATION OF PHYSICAL AND BIOGENIC REWORKING OF SANDY SEDIMENTS IN THE SOUTHEASTERN NORTH SEA

Knut Krämer, Soeren Ahmerkamp, Ulrike Schückel, Moritz Holtappels and Christian Winter

Manuscript prepared for submission.

ABSTRACT Morphodynamics on the seafloor of shallow coastal and shelf seas are mainly driven by the energetic physical forcing due to wave- and current-induced shear stress. As an important habitat for many benthic species searching shelter and food, they are also marked by intense bioturbation. Although this reworking activity is recognized as an important mechanism for the exchange between sediment and water column, quantifications of the relative importance of physical and biogenic reworking of subtidal shelf sediments are rare.

This work presents in situ measurements of volumetric reworking rates from different environments in the southeastern North Sea and over different seasons. Biogenic reworking rates are of the same order of magnitude for different benthic communities and seasons and reach as much as 14% of physically driven reworking via bedform migration. The quantitative comparison of the reworking rates unveil a link between physical and biogenic reworking: Higher physical reworking rates trigger higher biological reworking activity. The diffusive relocation of sediment also influences the topography of ripples and reduce their height up to 10% in a few hours during hydrodynamically inactive conditions.

The observations show that even in an energetic environment such as the southeastern North Sea, the benthic fauna performs an important ecosystem service by overturning upper seafloor sediments and enabling the exchange between sediment and water column. This reworking mechanism becomes particularly important in areas and during periods of sub-threshold conditions for physically driven sediment transport.

4.1 INTRODUCTION

The sea floor in coastal and shelf seas is an important ecosystem which provides many natural resources and important environmental services such as carbon cycling and nutrient degradation (Marinelli et al., 1998; Chen and Borges, 2009; Snelgrove et al., 2014). This energetic environment is characterized by intense morphodynamics, driven by physical forcing due to waves and currents but also by bioturbation (Rhoads and Boyer, 1982; Grant, 1983). The reworking activity of the benthic fauna during its search for food and

shelter is well recognized as an important contributor to sediment turnover (Mermillod-Blondin and Rosenberg, 2006; Meysman et al., 2006b). Many studies investigating the role of bioturbation so far cover laboratory experiments on dedicated species (Wrede et al., 2017) or theoretical considerations about effects of biogenic reworking e.g. on bedform dimensions (Soulsby et al., 2012). In situ observations of biologically driven morphodynamics are scarce and often limited to relatively easy accessible intertidal areas (Grant, 1983; Koo and Seo, 2017).

Laboratory measurements of biogenic reworking rates often use tracer techniques (Maire et al., 2008), which in combination with mathematical models allow for the computation of biodiffusion coefficients. However, they do not readily provide volumetric quantifications that can be compared with physically driven bedload transport. A pioneering study on an intertidal sandflat by Grant (1983) with indirect estimation of sand ripple migration showed that biogenic reworking rates can reach up to one third of physically driven bedload transport. In hydrodynamically less active environments such as deep seas or lakes, the role of bioturbation becomes more dominant Broach et al. (2016). Bioturbators in the benthic community are therefore regarded as important *ecosystem engineers* with a regulating function for geobiochemical cycling at the benthic interface (Solan and Kennedy, 2002).

This study presents in situ measurements of the morphodynamic response of the micro-bathymetry to physical forcing by currents and waves in exemplary areas in the German Bight. Drivers and effects are linked via the concept of a critical shear stress required for sediment motion derived from sedimentological properties. When the combined shear stress from wave and current action exceeds this critical threshold, small-scale bedforms (ripples) begin to migrate in the dominant current direction. During periods with conditions well below the threshold of sediment motion, sediment relocation by benthic fauna is observed, often in characteristic irregular pattern of local erosion and deposition. Volumetric reworking rates are computed as the difference between successive DEMs of the sediment surface. The resulting biogenic reworking rates are used to quantify the effect of biogenic reworking in comparison to physical bedload transport.

4.2 STUDY AREA SETTING

The data presented here was collected at seven locations with characteristic sediment properties in the German Bight in the southeastern North Sea during five cruises with R/V *Heincke* in the scope of projects *NOAH* and *CCP* (Fig. 4.1). Water depths range from 23 m at station CCP-D near Helgoland island to 48 m at station CCP-J in the deep region southeast of the Dogger Tail End.

The seafloor sediment consists mainly of fine sands with increasing mud content for areas located in the Elbe palaeovalley (Figge, 1981). Small-scale bedforms (ripples) of 1–2 cm height and around 20 cm length are present in sandy regions in water depth between 20 and 40 meters (Krämer and Winter, 2016; Ahmerkamp et al., 2017). Morpho-

logical features at the deeper stations with low bottom currents and beyond the reach of surface waves are of mostly of biogenic origin.

4.3 RANGES OF PHYSICAL FORCING

The physical forcing in the southeastern German Bight is determined by tidal and wind-driven currents and wave action (Kösters and Winter, 2014). Its local magnitude depends on the water depth, tidal range, phase in the spring-neap-cycle and seasonal meteorological forcing. Bedload sediment transport is driven by shear stresses generated by wave and current action on the seabed (τ_w, τ_c). Their combined effects on the reworking of sediment can be linked with sedimentological properties via the critical shear stress (τ_{crit}), determined from sedimentological characteristics as e.g. the median grain size d_{50} and immersed weight ρ'_s.

Large-scale pattern of wave induced shear stresses mainly scale with water depths: shallower areas along the North and East Frisian coasts are subjected to stronger wave action than deeper areas (Fig. 4.1b). Seasonal differences in meteorological forcing generate waves, high and long enough to affect the seafloor, more frequent during storm events in the winter season (Van der Molen, 2002). Wave-induced shear stresses therefore usually do not reach supercritical conditions for sediment motion from late spring to early fall.

The spatial distribution of tidal current magnitude scales with tidal range, which is minimal close to the amphidromic point south of Jutland Bank near 55° 25′ N, 5° 15′ E and increases towards the coasts (Fig. 4.1c). In shallow areas with water depth smaller than 25 m, current induced shear stresses above the threshold of motion are regularly exceeded for a few hours around peak flood or ebb flow. Tidal flow velocities and resulting shear stresses additionally vary over the spring-neap cycle. For stations in the intermediate range between 30 and 40 m, this adds a semimonthly timescale determining sub- or supercritical conditions for bedload transport.

Vice versa, this means that for large areas in the southeastern North Sea for a good part of the tidal cycle (current forcing) and a good part of the year (wave forcing), subthreshold conditions for sediment transport prevail.

4.4 DATA AND METHODS

The data discussed in this study was obtained by an autonomous seafloor observatory (lander) *Lance* (see Ahmerkamp et al. (2017) and supporting information). This four-legged platform is deployed from shipboard and afterwards autonomously observes the seafloor. Most deployments were started during low water slack so as to cover the following flood period. The platform is equipped with a downward-looking ADCP to record

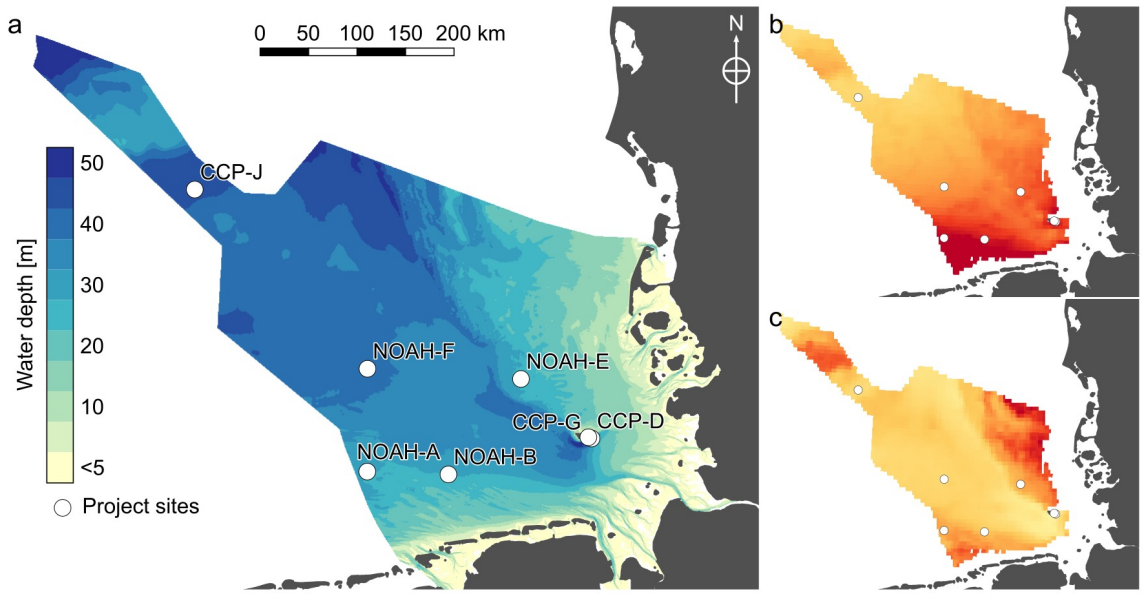

Figure 4.1: Location of deployment stations in the German Bight. (a) Bathymetry of the German EEZ. Qualitative pattern of annually averaged (b) current and (c) wave shear stress retrieved from the coastMap Geoportal (Helmholtz-Zentrum Geesthacht Zentrum für Material- und Küstenforschung GmbH (HZG), 2017) (CC BY-NC 4.0). Bathymetry data was made available by the project Geopotential Deutsche Nordsee (GPDN) (2013). Land polygons ©OpenStreetMap (2016) (Open Database License).

the near-bed velocity profile and a laser scanning system to record the micro-bathymetry. The available battery capacity allows for an observation period of around 12 hours.

4.4.1 *Physical forcing*

Current-induced shear stresses τ_c were computed using a logarithmic fit to 10-minute averaged velocity profiles over a range of 1 m from a downward-looking ADCP (*Teledyne RDI Workhorse Rio Grande* 1200 kHz, with a sampling frequency of 1 Hz) following the procedure described by Soulsby (1997, p.53pp). Only data with regression coefficients $R > 0.9$ was used.

Wave induced shear stresses τ_w were computed using the significant wave height H_s and peak period T_p from a North Sea model (COSYNA). The model results were validated for exemplary periods with waverider buoy measurements recorded near Helgoland. The maximum effect of combined wave and current shear stress is computed following Soulsby (1997, p.87pp) as

$$\tau_{max} = \sqrt{(\tau_m + \tau_w \cdot \cos\theta)^2 + (\tau_w \cdot \sin\theta)^2} \tag{4.1}$$

where

$$\tau_m = \tau_c \cdot (1.2 \cdot \tfrac{\tau_w}{\tau_w + \tau_c})^{3.2} \tag{4.2}$$

Waves defined by significant wave height and peak period from a spectral and stochastic perspective may be physically non-existent or irrelevant for sediment mobilization and transport. To include the effect of less frequent high waves, the wave-induced shear stress generated by the stochastically highest waves with a height of

$$H_{max} = 1.86 \cdot H_s \tag{4.3}$$

following EAK (2002) is also computed.

4.4.2 *Sedimentological properties*

Surface sediment samples taken at the investigated sites prior to deployment of the lander were analyzed in a Coulter Laser Diffractometer (*Beckman Coulter LS^{TM} 13 320*) to obtain grain size distributions. The critical shear stress τ_{crit} of the sediments was computed from the median grain size d_{50} following Soulsby (1997). An earlier study shows the validity of this approach (Krämer and Winter, 2016).

4.4.3 *Micro-bathymetry mapping and sediment reworking*

The micro-bathymetry is recorded at roughly hourly intervals using rectified images of a laser line projected on the seafloor. Laser and camera are mounted on a moving sledge with a horizontal traveling distance of 0.55 m. From the laser scans, DEMs of the bathymetry with an area of ca. 0.35 m $\times$ 0.55 m and a spatial resolution of $\Delta x = \Delta y = 2.5$ mm were generated using the `xyz2grid` function from the *Generic Mapping Tools* program suite (GMT V5.2.1; Wessel et al. (2013)) (Fig. 4.2). The bathymetry scans take around 5 minutes to complete. In relation to the morphodynamic timescale, individual scans are regarded as synoptic. Reworked sediment volumes were computed from the difference between the zero-mean elevation matrices Z recorded at successive time steps i and $i+1$ as

$$\Delta V = 0.5 \cdot \Sigma |Z_{i+1} - Z_i| \cdot \Delta x \cdot \Delta y \tag{4.4}$$

The volumetric reworking rates can be computed as

$$\frac{\Delta V}{A \cdot \Delta t} \tag{4.5}$$

Where Δt is the time between the scans and A is the base area of valid grid cells of the DEMs.

4.4.4 *Classification of reworking mode*

In the difference DEMs, ripple migration shows characteristic regular pattern of erosion on the stoss side and accretion on the lee side of the ripples (Fig. 4.4c–g). Biogenic reworking, in contrast, manifests in irregular patches (Fig. 4.4i–m). In some occasions, the

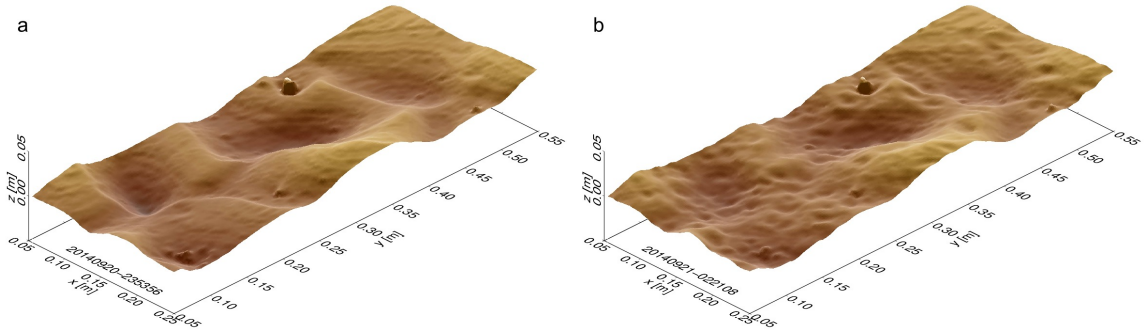

Figure 4.2: False-color DEMs of micro-bathymetry scans at station CCP-G recorded during cruise HE432, 20–21 September, 2014. (a) Active bedforms with smooth slopes at 23:53 local time. (b) Surface roughened by bioturbation at 02:21 local time.

form of large organisms like sea stars or flat fish can be detected in the difference DEMs (Fig. 4.3). For this study, the respective areas were masked in the difference DEMs when they did contribute to sediment relocation. The difference DEMs were classified into pure physically or biologically dominated reworking. Due to the difficulty to spatially separate simultaneous biogenic and physical reworking observed in a single scan, mixed reworking was not evaluated.

4.4.5 *Bedform height*

Ripple heights were determined using a statistical estimate determined by

$$\eta_s = 2 \cdot \sqrt{2} \cdot \sigma(Z) \tag{4.6}$$

This formulation is strictly only valid for 2D sinusoidal signals. Absolute heights in a field of 3D ripples may be overestimated by around 40% (Krämer and Winter, 2016). Nevertheless, this method can provide a stable estimate of relief variability and temporal variations thereof. Changes in ripple height from successive scans were used to compute ripple growth and decay rates.

4.4.6 *Bioturbation potential*

MUC samples (n≥3) were taken at all stations prior to the deployment of the lander. The retrieved cores were divided into 5 cm horizons and sieved to extract the infauna. After the census and classification of the species, their individual bioturbation potentials and reworking modes were determined. Community bioturbation potential was determined following Queirós et al. (2013).

$$BP_c = \sum_{i=1}^{n} \sqrt{B_i / A_i} \cdot A_i \cdot M_i \cdot R_i \tag{4.7}$$

Where B_i is the individual species bioturbation potential, A_i is the abundance, M_i and R_i are traits mobility and reworking mode, respectively. For the comparison with biogenic reworking rates, data from the upper 10 cm of the cores were evaluated.

Pattern of biogenic reworking were compared to descriptions of burrow structures and dimensions to identify the key bioturbators for the observed changes.

4.4.7 *Classification of physical forcing*

The physical forcing situation can be classified by comparing the combined wave and current shear stress to the critical shear stress required for the mobilization of sediment (Fig. 4.5–4.9).

Sub-threshold conditions exist when neither wave nor current induced shear stresses exceed the critical threshold for sediment mobilization. Observed changes in the bathymetry are then classified as biogenic reworking. Current dominated forcing exists when current shear stresses exceed the critical transport threshold during peak tidal flow and waves motion does not reach down to the seafloor. For these situations, more or less well defined slack water periods with little or no flow establish around the turn of the tides. These sub-threshold conditions may persist for several hours.

Combined current and wave forcing can be observed during storm events. Shear stresses may be supercritical leading to constant bedload transport over the entire observation period.

4.5 RESULTS

4.5.1 *Exemplary situations of physical and biogenic reworking*

A close observation of the micro-bathymetry with millimeter accuracy at hourly intervals during periods with sub-threshold conditions for sediment transport shows irregular pattern of sediment erosion and deposition (Fig. 4.2, Fig. 4.4). They manifest in small holes and mounds and a general roughening of previously smooth sediment surface. These pattern are evidence for biogenic reworking of seafloor sediments by benthic organisms during their burrowing and foraging activities. Biogenic reworking pattern were observed for 7 out of 15 evaluated deployments. The physical and biogenic reworking pattern and resulting rates are highly variable depending on the forcing situation and interaction between forcing and fauna activity. To outline the range of reworking rates under different forcing conditions, five characteristic examples are described below. The results from all evaluated deployments are summarized in Tab. 4.1. Although both physical and biogenic reworking mostly just occurs for a few hours between the turn of tides the unit [mm d^{-1}] is chosen for the sake of comprehensible numbers. Reworking rates are reported as *avg.* $\pm$*std. (max.)*.

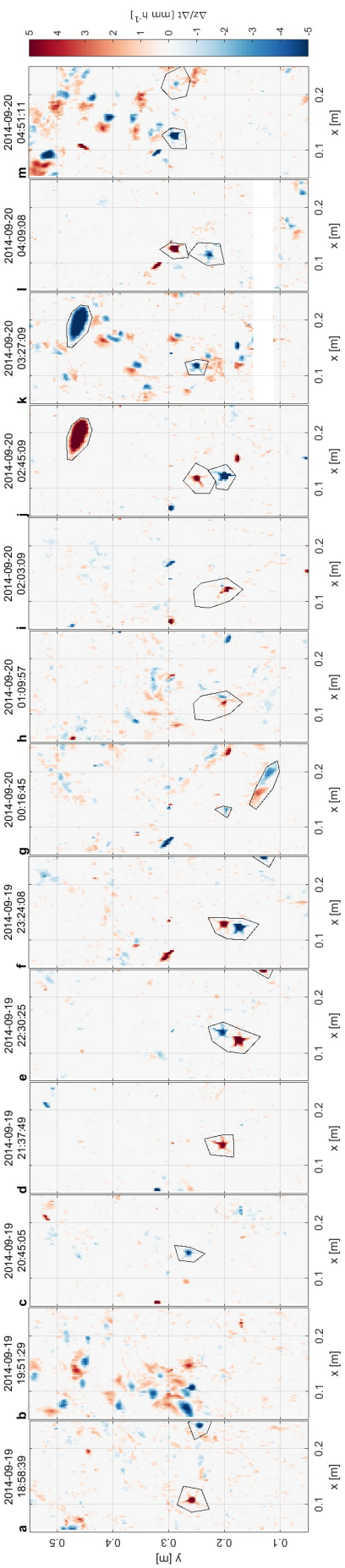

Figure 4.3: Difference DEMs for deployment at station NOAH-E during cruise HE432. Black polygons outline manually masked areas affected by locomotion of large fauna (e.g. *Asteria rubens* (a,c–f,j–m) or *Pleuronectes platessa* (j,k)) without a contribution to sediment relocation.

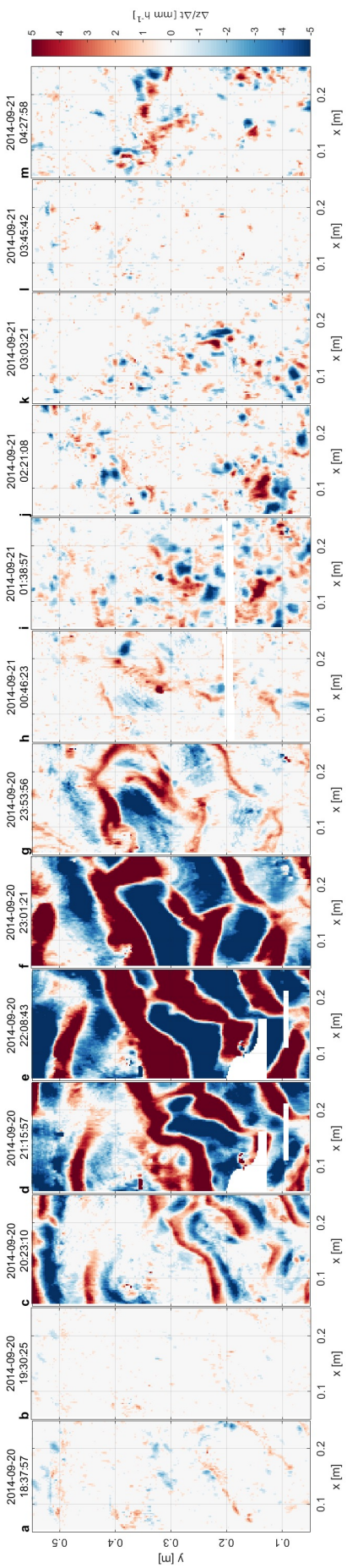

Figure 4.4: Difference DEMs for deployment at station CCP-G during cruise HE432. Characteristic pattern of physical reworking by ripple migration (c–g) and biogenic reworking (h–m) can be observed.

SHALLOW STATION: CCP-G (HE432, 09/2014) Station CCP-G is located in an area of subaqueous dune fields southeast of Helgoland island. With dune heights of around 2 m and lengths of around 50 m, the bathymetry is locally very heterogeneous. This station is dominated by strong tidal forcing.

Current shear stresses were supercritical for a period of around 3 hours during flood (Fig. 4.5a). Wave action did not reach the seabed. After a period of bedform migration, high biogenic reworking activity can be observed. The biogenic reworking rate measured here amounts to 5.7 ± 2.6 mm d^{-1} which is 14% of the physical reworking rate yielding 41.7 ± 27.9 mm d^{-1}. The maximum instantaneous biogenic rate even reaches 10.1 mm d^{-1}.

The characteristic pattern of local erosion and deposition (Fig. 4.4h–m) have a typical diameter of 15–20 mm. In combination with the census of benthic species and their associated bioturbaton potential acquired from MUC samples, *Callianassa subteranea* was identified as the most likely initiator. Assuming a funnel-shaped structure with angle-of-repose slope for the upper part of the burrow, the typical diameter agrees well with an average tube diameter of 6 mm for adult individuals of *C. subteranea* (Forster and Graf, 1995).

INTERMEDIATE STATION: NOAH-E Station NOAH-E is located on the former northeastern bank of the Elbe palaeovalley in a water depth of 30 m in a fine sand setting (d_{50} =242 μm). The magnitude of flow velocity and current shear stress varies over the spring-neap cycle. Waves are only effective for sediment transport during storm events.

The deployment during cruise HE417 (03/2014) was characterized by strong tidal flow in combination with wave action (Fig. 4.6). This leads to supercritical conditions for sediment transport throughout the first six of eight hours of observation. Even during sub-threshold conditions, biogenic reworking pattern cannot be observed. The physical reworking rate is 44.1 ± 39.8 (103.0) mm d^{-1}.

Under neap conditions and without wave action during cruise HE432 (09/2014), the critical shear stress is not exceeded for the entire observation period (Fig. 4.7). The changes observed in the micro-bathymetry are therefore entirely attributed to biological activity. Locomotion of large animals like star fish and flat fish can be observed in the micro-bathymetry scans. Affected areas were manually masked since they do generate a large apparent signal but do not correspond to sediment reworking. The biogenic reworking rate amounts to 2.9 ± 1.0 mm d^{-1} and increases to a maximum value of 4.7 mm d^{-1} during three single events which exhibit characteristic erosion-deposition pattern.

During cruise HE447 (06/2015), current shear stresses are supercritical but wave action does not reach the seabed (Fig. 4.8). The physical reworking rate amounts to 18.7 ± 20.2 mm d^{-1}. Biogenic reworking pattern can only be identified for one scan. The shape suggest that sediment is relocated due to the movement of an individual of *Amphiura filiformis*. The resulting instantaneous reworking rate is 2.6 mm d^{-1}.

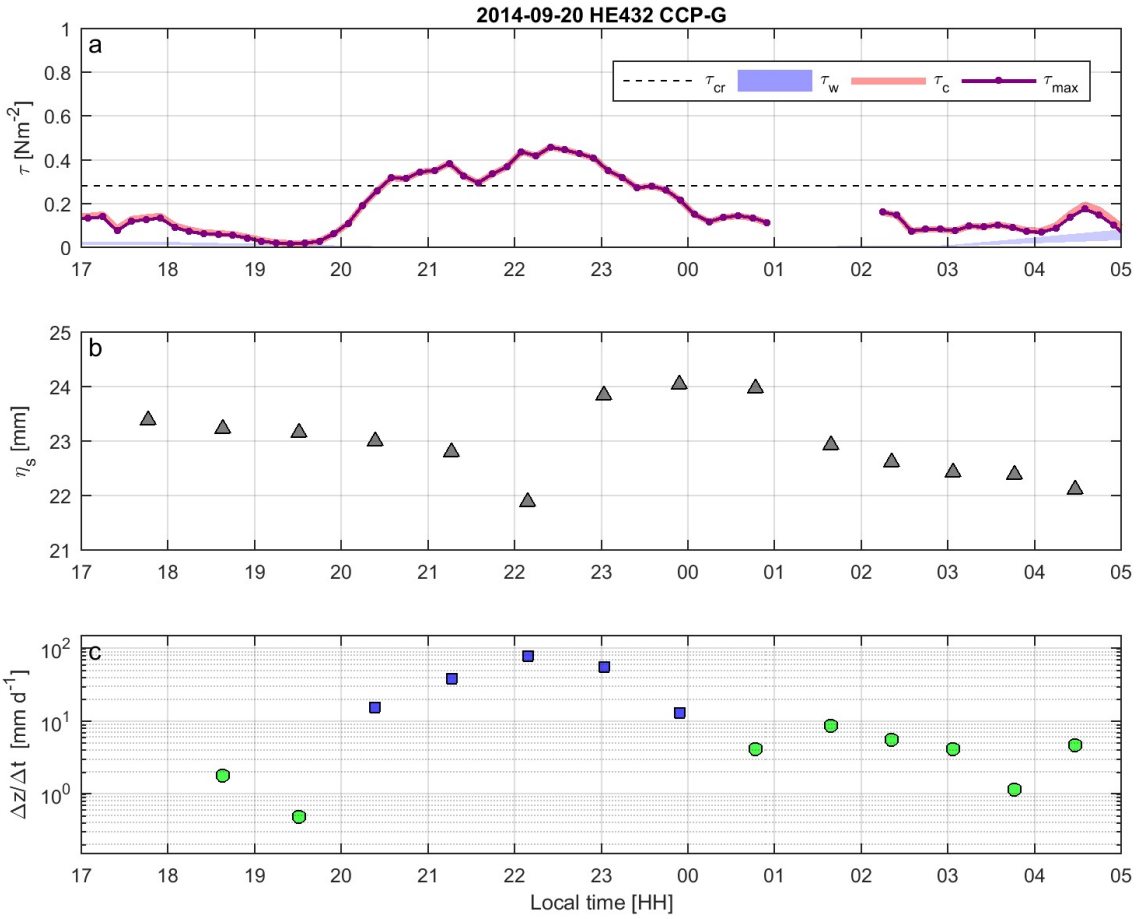

Figure 4.5: Deployment at station CCP-G during cruise HE432. (a) Wave, current and maximum combined shear stress. (b) Ripple height. (c) Physical (blue squares) and biogenic (green circles) reworking rates.

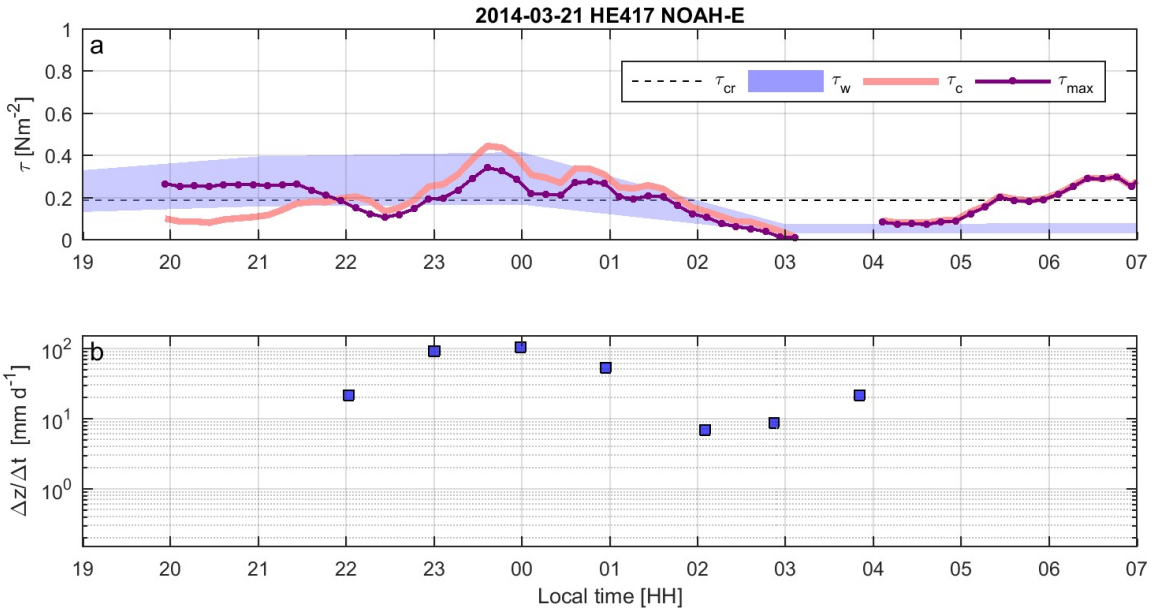

Figure 4.6: Deployment at station NOAH-E during cruise HE417. (a) Wave, current and maximum combined shear stress versus critical shear stress. (b) Reworking rates.

DEEP STATION: CCP-J (HE432, 09/2014) Located southeast of the Dogger Bank, station CCP-J lies in a water depth of 48 m. The seafloor sediment consists of fine sand (d_{50} =131 μm) with a mud content of 5–10% (Figge, 1981). As the sediment is not fully consolidated, the lander settles over the first five hours of the deployment (Fig. 4.9). Apparent reworking rates from this period cannot be used. Wave action can be neglected and current shear stresses do not exceed the critical threshold. The observed biogenic reworking pattern result in a rate of 1.5 ± 0.1 (1.9) mm d^{-1}.

4.5.2 *Bedform decay and form roughness*

A significant reduction of bedform heights due to biogenic sediment reworking was observed only during cruise HE432 (09/2014) at station CCP-G. Here, the bedform height is reduced by around 10% (from 24 to 22 mm) in a matter of 3 hours during the high water slack period (Fig. 4.5b). The previous flood had increased bedform heights from a similar level, indicating a dynamic equilibrium between physical growth and biogenic decay.

The reduction of bedform heights results in a reduction of form roughness $k_{s,f}$ by 10% using the relation of van Rijn (1984) and a reduction of roughness height $z_{0,f}$ by 16% using the relation of Soulsby (1997).

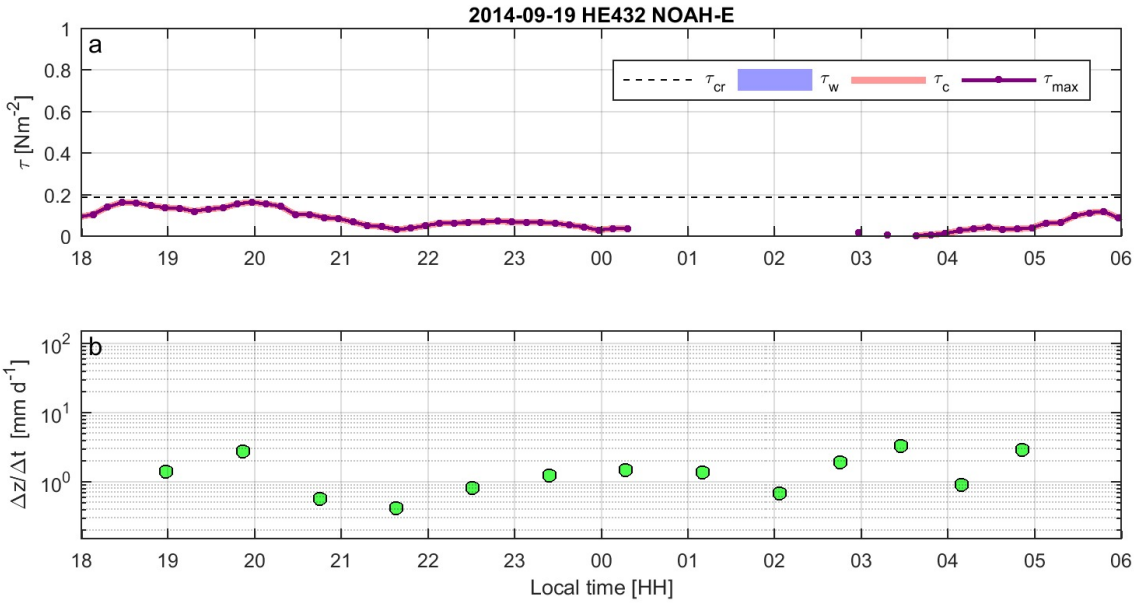

Figure 4.7: Deployment at station NOAH-E during cruise HE432. (a) Wave, current and maximum combined shear stress versus critical shear stress. (b) Reworking rates.

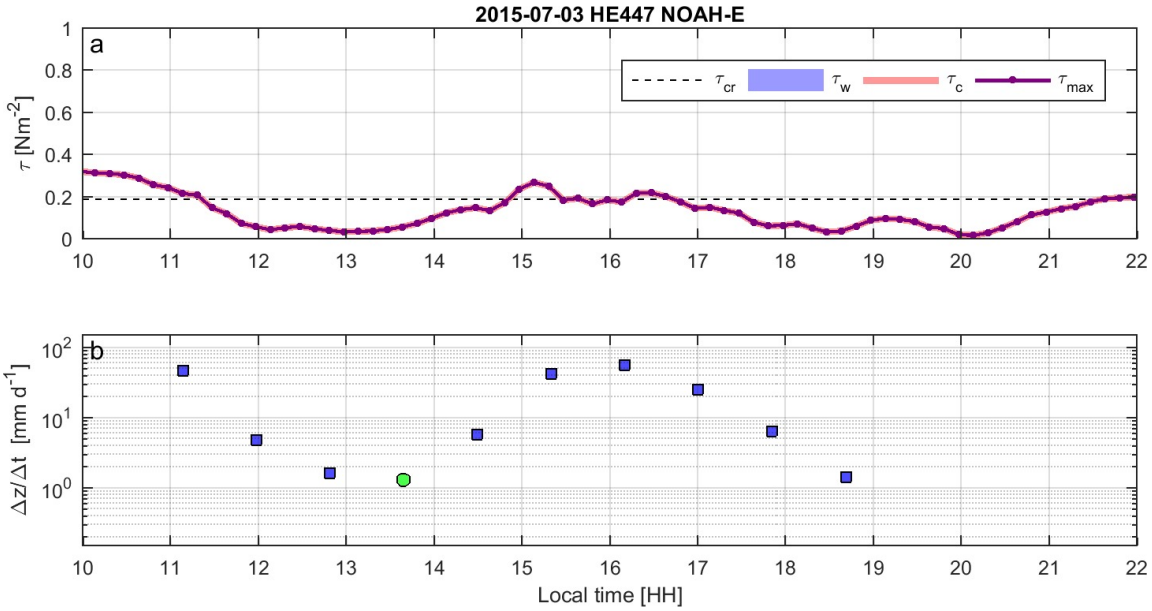

Figure 4.8: Deployment at station NOAH-E during cruise HE447. (a) Wave, current and maximum combined shear stress versus critical shear stress. (b) Physical (blue squares) and biogenic (green circles) reworking rates.

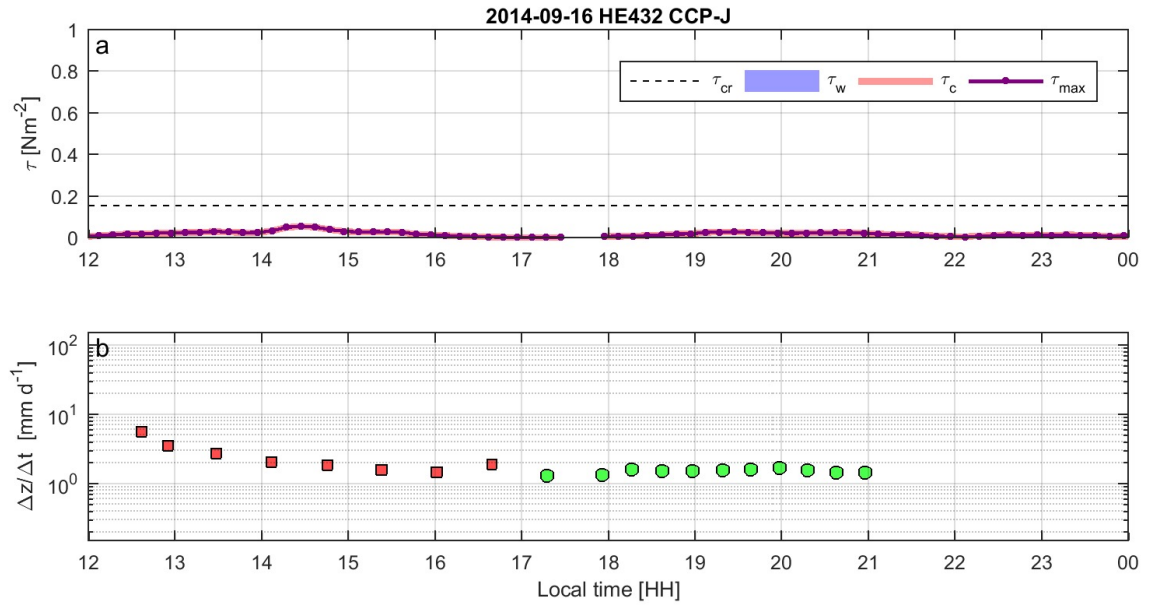

Figure 4.9: Deployment at station CCP-J during cruise HE432. (a) Wave, current and maximum combined shear stress versus critical shear stress. (b) Biogenic reworking rates (green circles). Red squares indicate invalid data due to the settling of the lander into the unconsolidated sediment during the first five hours of the deployment.

Table 4.1: Deployment meta data and physical and biogenic reworking rates obtained from difference DEMs. Rates are given in the form: *avg.* ±*std.* *(max.)*. The forcing classification indicates active sediment transport conditions ($\tau > \tau_{crit}$) by current (c), wave (w) or both wave and current (w+c), or sub-threshold conditions (s). Community bioturbation potential BP_c is given only for observations of biogenic reworking.

			Deployment				Environment			Reworking rate						Bioturbation
Cruise	Station	Site	Date	Duration	Position		Depth	Grain size	Forcing	Physical			Biogenic			potential
				[hh:mm]	Lat [°]	Lon [°]	d [m]	d_{50} [μm]		dZdT [mm d^{-1}]			dZdT [mm d^{-1}]			BP_c
HE417	0018-3	NOAH-B	2014-03-13	03:39	53.98650	6.86783	29.5	211	c	9.5	±2.3	(13.5)				
HE417	0036-1	CCP-D	2014-03-17	09:31	54.16850	7.98850	23.1	458	w+c	85.8	±13.0	(106.3)				
HE417	0044-1	CCP-G	2014-03-20	07:30	54.17317	7.95867	25.3	559	w+c	56.6	±44.3	(109.7)				
HE417	0066-1	NOAH-E	2014-03-21	08:06	54.44433	7.41450	29.5	242	w+c	44.1	±39.8	(103.0)				
HE432	0005-11	CCP-J	2014-09-16	08:30	55.25833	4.74967	48.4	131	s				1.5	±0.1	(1.9)	4589
HE432	0010-6	NOAH-E	2014-09-19	10:45	54.43750	7.42267	29.3	247	s				2.9	±1.0	(4.7)	2380
HE432	0011-1	CCP-G	2014-09-20	10:42	54.17317	7.95867	25.3	559	c	41.7	±27.9	(80.4)	5.7	±2.6	(10.1)	3834
HE432	0018-1	NOAH-B	2014-09-23	08:29	53.98717	6.87050	29.5	211	w+c	54.6	±37.2	(110.5)				
HE441	0010-1	NOAH-D	2015-03-20	02:13	54.09250	7.35850	37.2	107	w+c	52.0	±22.5	(80.4)				
HE441	0026-1	NOAH-E	2015-03-24	05:56	54.44133	7.41250	29.6	242	w+c	55.6	±45.4	(110.1)	5.1	±0.0	(5.1)	n/a
HE441	0043-1	NOAH-A	2015-03-26	09:01	53.98717	6.22483	32.0	392	w+c	10.7	±6.0	(24.8)				
HE447	0077-1	NOAH-A	2015-06-28	08:18	53.98850	6.23083	31.9	354	s				3.5	±1.0	(5.3)	4270
HE447	0101-1	NOAH-F	2015-06-29	12:20	54.46850	6.19300	41.2	129	c				5.1	±1.0	(6.6)	7216
HE447	0129-1	NOAH-E	2015-07-03	08:39	54.43883	7.42300	29.3	240	c	18.7	±20.2	(51.3)				
HE470	0088-2	NOAH-E	2016-08-28	11:50	54.44117	7.41817	29.5	242	c	4.7	±1.0	(5.6)	4.3	±1.5	(7.4)	n/a

4.6 DISCUSSION

4.6.1 *Physical and biogenic reworking*

Physical reworking by ripple migration is an omnipresent process in the sandy, shallow (d<30 m) areas of the German Bight. Active ripples adapt to the direction of tidal flow and migrate in an order of their length scale over a period of a few hours during flood and ebb flow. In intermediate areas in water depths between 30 and 35 m, the activity and migration rate of ripples is controlled by the magnitude of tidal flow, varying over the spring-neap cycle. Although they may not often become the dominant driver in ripple generation, the stirring effect of waves facilitates ripple migration. Areas in the Elbe palaeovalley located in water depths of around 40 m and with higher mud contents do not exhibit active ripples and wave driven sediment transport only occurs during intense storm events.

The average physical reworking rates observed range from 9.5 to 85.8 mm d^{-1}. The average biogenic reworking rates are one order of magnitude lower and range from 1.5 to 5.7 mm d^{-1}. Where both physical and biogenic reworking was observed, higher average physical reworking rates coincide with higher average biogenic reworking rates: Biogenic rates under undisturbed conditions are lower (2.9–3.5 mm d^{-1}) than under conditions with low physical reworking (4.3 mm d^{-1}) and further increase during high physically driven reworking (5.1–5.7 mm d^{-1}) (Fig. 4.10a).

When combined current and wave action drive bedload transport, small benthic organisms may not find calm enough conditions at or near to the sediment surface and little biogenic reworking can be observed. Where tidal currents generate transport conditions only for a few hours around peak tidal flow, intermittently mobile bedforms set the table for deposit feeders by entrapping oxygen and nutrient rich water. Without previous ripple migration, the surface sediment may be rapidly depleted of food resources and thus become unattractive for deposit feeders and associated predators. Additionally, as a response to the overturning of the upper few centimeters of the seabed by migrating bedforms, burrowing suspension feeders are periodically forced to renew or clean out the upper part of their burrows to regain access to the water column. Both processes lead to increased biogenic reworking rates under mobile bedform conditions. Observations at station NOAH-E under immobile bedform conditions during HE432 (09/2014) with low biogenic reworking rates and with weak bedform migration during HE447 (07/2015) with higher biogenic rates hint in this direction.

The observed bioturbation pattern cannot be related to any of the three key bioturbators in the German EEZ, *Amphiura filiformis*, *Echinocardum cordatum* and *Nucula nitidosa*, identified by Wrede et al. (2017). However, none of said species has an high individual contribution to bioturbation potential in the investigated areas (compare Wrede et al., 2017, Fig. 2B–D). Due to the small area covered by the scans, the contribution of relatively large organisms is likely underestimated if they are not present in the scan area by

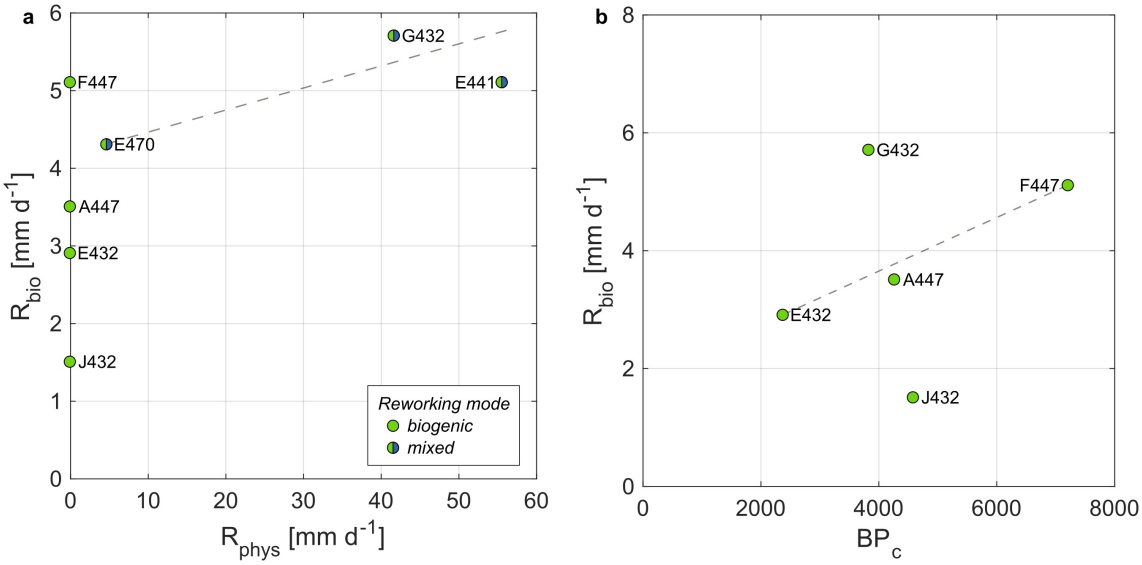

Figure 4.10: (a) Reworking rates for deployments with only biogenic and both physical and biogenic reworking. (b) Biogenic reworking rate versus community bioturbation potential BP_c (Queirós et al., 2013). Dashed lines were inserted as guide to the eye.

chance. The method presented here rather provides an estimation of the cumulative background reworking activity provided by smaller species than by one or few key species.

For one observation (HE432 CCP-G), *Callianassa subteranea* was identified as the species presumably responsible for the characteristic reworking pattern. Both biogenic reworking rates and community bioturbation potential are available for five stations (Fig 4.10b). When the shallow station CCP-G ($d = 25.3$ m) and the deep station CCP-J ($d = 48.4$ m) are excluded, the observed biogenic surface reworking rates scale with community bioturbation potential. However, the dataset is to sparse to accept this as a general trend.

The range of biogenic reworking rates for individual species of benthic fauna reported in literature ranges over several orders of magnitude (Tab. 4.2). The strong seasonal variability of reworking activity of individual species has been shown to correlate with environmental conditions (Nichols, 1974; Cadée, 1976; Berkenbusch and Rowden, 1999). The observations presented here return strikingly similar average biogenic reworking rates, independent of location (benthic community) and season (environmental conditions).

4.6.2 *Biogenic bedform decay*

In consequence of the relatively small observational area in comparison to the typical ripple length, the appearance of a new ripple can lead to a seemingly increasing or decreasing height. Therefore, results have to be interpreted carefully during phases of active ripple migration. Changes in bedform height are therefore only meaningful for periods when sub-threshold conditions for transport exist and the ripples are not active. Lee slope angles of mobile bedforms may exhibit local angles above the critical slope angle of the sediment because they are stabilized by flow reversal in the flow separation

Table 4.2: Biogenic reworking rates for individual species reported in literature. The units of original values were converted to [mm d^{-1}]. Where the reworking rate in the original study was given as dry mass, a bulk density of 2.65 kg m^{-3} (quartz sand) and a porosity of 0.35 was assumed for the conversion.

Study	Location	Organism	Reworking rate [mm d^{-1}]
Rhoads (1963)	Buzzards Bay, US	*Yoldia limatula*	5.000 – 6.000
	Long Island Sound, US		23.000 – 51.000
Nichols (1974)	Pudget Sound, US	*Pectinaria californiensis*	13.679
Cadée (1976)	Wadden Sea, NL	*Arenicola marina*	0.384 – 0.904
Cadée (1979)	Wadden Sea, NL	*Heteromastus filiformis*	0.100 – 2.500
Kudenov (1982)	Tomales Bay, US	*Axiothella rubrocinta*	290.276
Grant (1983)	Debidue Flat, US	*Saccoglossus kowalevskii*	0.043
		Acanthohaustorius millsi	1.663
		Pseudohastorius caroliensis	1.454
		Paraomis fulgens	10.368 – 93.264
Berkenbusch and Rowden (1999)	Otago Harbour, NZ	*Callianassa filholi*	152.693
Koo and Seo (2017)	Gomso Bay, KR	*Perinereis aibuhitensis*	0.085
This study	German Bight, DE	*n/a*	1.500 – 5.700

zone. When current shear stresses drop below the critical threshold for sediment transport, the slopes are left in an unstable state and easily avalanche towards the lower stable angle of repose. This behavior can be shown to reduce bedform height up to 10% over the sub-threshold phase and without evidence of biological activity.

The declining bedform height observed during HE432 at station CCP-G (Fig. 4.5b) highlights that the decay rates of ripple height due to the redistribution of sediment by benthic organisms may equally reach up to an order of up to 10% of the height within a few hours. Physically driven initialization, growth and decay of wave and current ripples are relatively well understood and included in semi-empirical models. Although formulations exist for biogenic bedform decay (Soulsby et al., 2012), absolute rates cannot be specified without field observations. The process of biogenic reworking is influenced by many factors and acts on various spatial and temporal scales, the reduction rate observed here may serve as a first estimate of the order of magnitude of biogenic ripple decay by bioturbation.

Theoretically, this decay rate would flatten out a rippled seabed of 2 cm height within two to three days. However, current ripples in tidally dominated environments become periodically active and after a reduction quickly grow towards their equilibrium height (Bartholdy et al., 2015). The tidal forcing therefore interrupts biogenic decay and a dynamic equilibrium between may be reached. Given enough time under sub-threshold conditions for transport, e.g. under neap tide conditions or after a flood event in an otherwise calm environment, one might expect to see a complete flattening of a rippled topography. However, this cannot be observed during HE432 at station NOAH-E (Fig. 4.7).

This may be explained by a different benthic community composition or reworking mode less effective for bedform decomposition.

4.7 CONCLUSIONS

Physically driven reworking rates are in an order of magnitude from 10 to 100 mm d^{-1}. Biogenic reworking rates are one order of magnitude lower (1 to 10 mm d^{-1}).

The high biogenic reworking rates observed at station CCP-G (HE432) show the important contribution of the benthic community to overall reworking in an environment with intense physical forcing. As bedload transport and ripple migration occur around peak tidal flow, the benthic organisms step in during the hydrodynamically calm phases and continue to overturn sediment. As the observations under neap conditions at station NOAH-E during cruise HE432 (09/2014) show, biogenic reworking is at times the only mechanism for sediment reworking for areas where transport conditions are only reached during spring tide. For deeper areas with low current forcing, which are only affected by high wave action during seasonal storm events, the role of the biogenic reworking becomes even more important. By reworking under hydrodynamically calm conditions, the benthic fauna sustains cycling processes at the benthic interface and provides an important ecosystem service.

Recent studies highlight that the activity of benthic communities responsible for bioturbation are highly variable on both temporally and spatially over several orders of magnitude : The temporal scales of variability in benthic fauna activity range from semidiurnal and diurnal cycles as a response to tides and daylight to seasonal cycles as a response to environmental parameters such as water temperature and food availability (Oehler et al., 2015; Gogina et al., 2017; Morys et al., 2017). This makes a general assessment of bioturbation potential or even a quantification of biogenic reworking rates very complex. Nevertheless, the data discussed here shows a striking similarity between biogenic reworking rates at different stations and across different seasons.

Measured biogenic reworking rates show a cumulative bioturbation effort by a part of the benthic community as the contribution of large bioturbators is possibly underestimated by the sampling method. The contribution of individual species cannot be determined as e.g. in lab studies (Wrede et al., 2017). This method rather provides a first estimate of the range of biogenic surface reworking under natural conditions and shows its relevance in comparison to physically driven bedload transport in an energetic environment. More frequent or long-term observations of this kind in representative areas can help to determine realistic ranges and averages for biogenic reworking rates which can be extrapolated to larger areas and longer time scales. In combining these rates with the concept of evaluating the critical shear stress of the bed sediment versus the actual sustained wave and current shear stress, locations and occasions can be identified where or when bioturbation locally or temporarily dominates sediment turnover. When the physical boundary conditions can be defined e.g. from sediment databases and

hydro-numerical models, large-scale ecosystem services provided by benthic fauna can be assessed.

While Ahmerkamp et al. (2017) showed a link between ripple migration and microbial activity via variations of oxygen penetration, this study highlights a link on a larger scale, between ripple migration and surface reworking activity of the benthic fauna.

ACKNOWLEDGEMENTS This study was carried out in the framework of project *NOAH – North Sea Observation and Assessment of Habitats*. The authors appreciate the support from captain and crew of R/V *Heincke* and a good and professional working atmosphere during the cruises.

AUTHOR CONTRIBUTIONS C.W. (HE417, HE441, HE447, HE470) and M.H. (HE432) planned and lead the cruises and conceived the sampling strategies. M.H. and S.A. operated the *Lance* lander. S.A. processed raw laserscan data. U.S. collected benthic fauna samples, identified species and calculated bioturbation potentials. K.K. analyzed laserscan and hydrodynamic data. K.K. conceived and wrote the manuscript in close discussion with C.W. and with input from M.H., S.A. and U.S..

5

ABRUPT EMERGENCE OF A LARGE POCKMARK FIELD IN THE GERMAN BIGHT, SOUTHEASTERN NORTH SEA

Knut Krämer, Peter Holler, Gabriel Herbst, Alexander Bratek, Soeren Ahmerkamp, Andreas Neumann, Alexander Bartholomä, Justus van Beusekom, Moritz Holtappels and Christian Winter

Manuscript published in *Scientific reports*, 7(1), 2017.

ABSTRACT A series of multibeam bathymetry surveys revealed the emergence of a large pockmark field in the southeastern North Sea. Covering an area of around 915 km^2, up to 1,200 pockmarks per square kilometer have been identified. The time of emergence can be confined to 3 months in autumn 2015, suggesting a very dynamic genesis. The gas source and the trigger for the simultaneous outbreak remain speculative. Subseafloor structures and high methane concentrations of up to 30 μmol l^{-1} in sediment pore water samples suggest a source of shallow biogenic methane from the decomposition of post-glacial deposits in a paleo river valley. Storm waves are suggested as the final trigger for the eruption of the gas. Due to the shallow water depths and energetic conditions at the presumed time of eruption, a large fraction of the released gas must have been emitted to the atmosphere. Conservative estimates amount to 5 kt of methane, equivalent to 67% of the annual release from the entire North Sea. These observations most probably describe a reoccurring phenomenon in shallow shelf seas, which may have been overlooked before because of the transient nature of shallow water bedforms and technology limitations of high resolution bathymetric mapping.

5.1 INTRODUCTION

Pockmarks are morphological expressions of vigorous fluid escape from subaqueous sediments. Since first detections in the 1970's and the coining of the term (King and MacLean, 1970), pockmarks have been documented in lakes (Reusch et al., 2015), estuaries (Rogers et al., 2006), on continental shelves (Brothers et al., 2014) as well as in coastal (Andrews et al., 2010) and deep sea environments (Dimitrov and Woodside, 2003; Sultan et al., 2014). The bedforms are described as cone-shaped craters in the seabed (Hovland, 1989; Judd and Hovland, 2009) with diameters in the order of centimeters up to 100s of meters and depths from a few decimeters to 10s of meters (Sultan et al., 2014; Judd and Hovland, 2009; Hovland et al., 1984; Scanlon and Knebel, 1989). Their morphological expression varies from isolated elliptical features to coherent clusters or strings. The emergence of pockmarks and associated fluid seepage influences the entire

local environment (Hovland and Judd, 1988), especially seabed flow structures (Fandel et al., 2017a), morphodynamics (Fandel et al., 2017c), biogeochemistry (Niemann et al., 2005) and ecology (Dando et al., 1991). Many occurrences of pockmarks can be linked to the seepage of fluids including carbon dioxide and groundwater but the majority of reported pockmarks have been related to the expulsion of biogenic methane from the microbial degradation of organic matter (Judd and Hovland, 2009; Fleischer et al., 2001).

In contrast to continuous diffusive seepage, the presence of pockmarks indicates a more vigorous escape of fluids from the seabed. The formation mechanism of gas induced pockmarks can be divided into three phases (Hovland, 1989): During the first phase, pressure is built up as gas rises from deeper reservoirs and accumulates below the seabed. When the interstitial gas pressure exceeds the load of the overlying sediment and water column, the gas erupts locally, suspending sediment into the water column and a crater remains at the eruption site. The post-eruption phase can either be a period of continuous seepage through the created vents or a dormant period until the critical pressure is exceeded again.

Identified triggers for the eruption of pockmarks include earthquakes (Field and Jennings, 1987; Hasiotis et al., 1996), tides (Ellis and McGuinness, 1986) and storm waves (Hovland and Judd, 1988). In shallow water, pressure oscillations from waves of sufficient height and wave length may penetrate into the sediment to a depth equal to the wave amplitude (Okusa, 1985). The cyclic loading and unloading of pressure leads to regular compaction and extraction of the subseafloor inducing a pumping effect and allowing gas bubbles to rise through the sediment (Hovland, 1989). Finally, the release of pressure under a wave trough may lead to over-stressing and mechanical failure of the sediment matrix.

The sedimentological setting of pockmark fields is often characterized by a cohesive, clay-rich surface sediment (Fleischer et al., 2001) which is also considered a good recording medium for the pockmarked morphology (Hovland et al., 1984). Pockmark dimensions scale with the characteristic grain size of the seafloor sediments (Judd, 2001). Larger and deeper pockmarks with diameters in the order of 100 meters and depths in the order of 10 meters have been found in fine-grained sediment (Judd and Hovland, 2009). Pockmarks in coarser, e.g. sandy sediments are usually in the order of 10 m in diameter and less than 1 m in depth (Judd and Hovland, 2009; Szpak et al., 2015).

In the North Sea, pockmarks have previously been reported on the Dutch, the Danish, the UK and Norwegian shelf, along the Norwegian continental margin and in the Norwegian trench (Judd and Hovland, 2009; Hovland and Judd, 1988; Fleischer et al., 2001; Judd, 2001; Schroot et al., 2005; Hovland, 1993; Masoumi et al., 2014). Most of these occurrences are located in deeper waters and fine grained seafloor sediments. In the German North Sea sector, no occurrences of pockmarks have been reported to date.

5.2 THE HELGOLAND REEF POCKMARK FIELD

The Helgoland Reef area is located around 45 km northwest of Helgoland Island in the southeastern German Bight of the North Sea (Fig. 5.1a,b and supplementary Fig. A.1). Water depths range from 25 m to 40 m. The seafloor sediments consist largely of fine to medium sands with low mud content (<5%). Occasionally, the seabed exhibits mobile ripples of centimeter amplitude, indicating a morphodynamically active environment (Krämer and Winter, 2016; Ahmerkamp et al., 2017). Toward southwest, the area is delimited by the deeper channel of the Elbe estuary with water depths of up to 45 m and with increasing mud content. The post-glacial (10,000–8,700 y BP) confluence of the rivers Eider and Elbe was located in this region as indicated by seismo-acoustic records and drilling cores (Figge, 1980; Köhn, 1991; Tietze, 1983) (Fig. 5.1b).

Successive surveys with MBES between 2013 and 2016 revealed that the formerly flat and largely featureless sandy seafloor of the Helgoland Reef was transformed into an extensive pockmark field between July and November 2015 (see supplementary Fig. A.2 and Fig. A.3). When the area was surveyed after the first fall storms in November 2015, the seafloor was densely covered with elliptical depressions of around 10 m by 20 m horizontal extent and a maximum depth of around 0.2 m with respect to the surrounding bathymetry. Each depression was accompanied by a neighboring mound of similar shape and amplitude (Fig. 5.2c,d).

When the site was revisited in August 2016, an area of 34.25 km^2 was surveyed with MBES with full seafloor coverage (Fig. 5.1a, Fig. 5.2a). 15,506 pockmarks were detected in the digital depth models (DDMs). The depressions cover about 6% of the surveyed seafloor area. The average area of an individual pockmark depression is 140 m^2 and the average volume is 17 m^3. The average areal density is 453 pockmarks per square kilometer while local clusters exhibit densities of up to 1,200.

The gross volume of relocated sediment from the detected pockmark depressions amounts to around 260,000 m^3. To delimit the overall extent of the pockmarked area, MBES surveys were continued in a wider spaced grid (Fig. 5.1a). The overall pockmark region covers around 915 km^2 in water depths ranging from 25 m to 39 m. The areal density of pockmarks increases with the local water depth. Although dense accumulations are found in different absolute depths, local depressions and channels in the bathymetry exhibit denser agglomerations than mounds and ridges which are often completely free from pockmarks. Extrapolating the average pockmark density to the extended pockmark region amounts to a total of more than 410,000 pockmarks, with a gross volume of around 6,900,000 m^3 of relocated sediment equaling about 12,000,000 t of sand (assuming a quartz sand bulk density of 2,650 kg/m^3 and a porosity of 0.35).

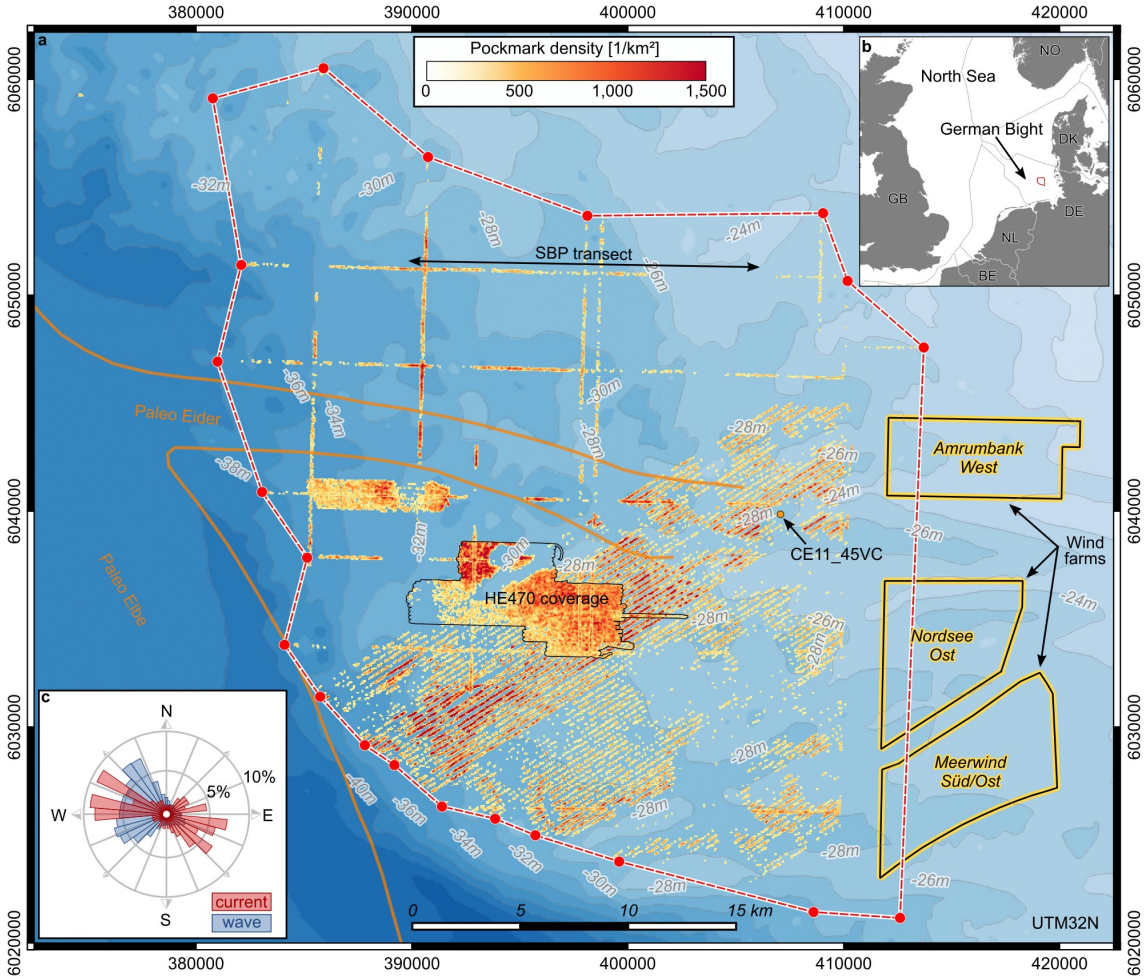

Figure 5.1: The Helgoland Reef pockmark field. (a) Extent of the field and pockmark density in relation to the course of the Paleo Eider and Paleo Elbe valley (Figge, 1980). The location of the SBP transect and location of core CE11_45VC from Fig. 5.4 are indicated. (b) Location of the Helgoland Reef pockmark field in the North Sea. (c) Histogram of the hydrodynamic climate at Helgoland Reef. The data were provided by the COSYNA system (Helmholtz-Zentrum Geesthacht Zentrum für Material- und Küstenforschung GmbH (HZG), 2016) operated by Helmholtz-Zentrum Geesthacht Zentrum für Material- und Küstenforschung GmbH. The maps in this figure were generated using QGIS Version 2.14.11 (QGIS Development Team, 2016). Bathymetry data was made available by project Geopotential Deutsche Nordsee (GPDN) (2013). Maritime boundaries and wind farm polygons were made available by the EMODnet Human Activities project (European Marine Observation and Data Network (EMODnet), 2017), funded by the European Commission Directorate General for Maritime Affairs and Fisheries. Wind farm data were collected by the OSPAR Commission. Maritime boundaries were provided by the European Environment Agency. Land polygons ©OpenStreetMap (2016) (available under the Open Database License; see www.openstreetmap.org/copyright).

5.3 HYDRO-ACOUSTIC EVIDENCE FOR SHALLOW GAS AND ACTIVE SEEPAGE

Shallow subseafloor records of a SBP indicate potential migration pathways facilitating the ascent of the gas from shallow reservoirs (Fig. 5.4b). Nine months after the presumed

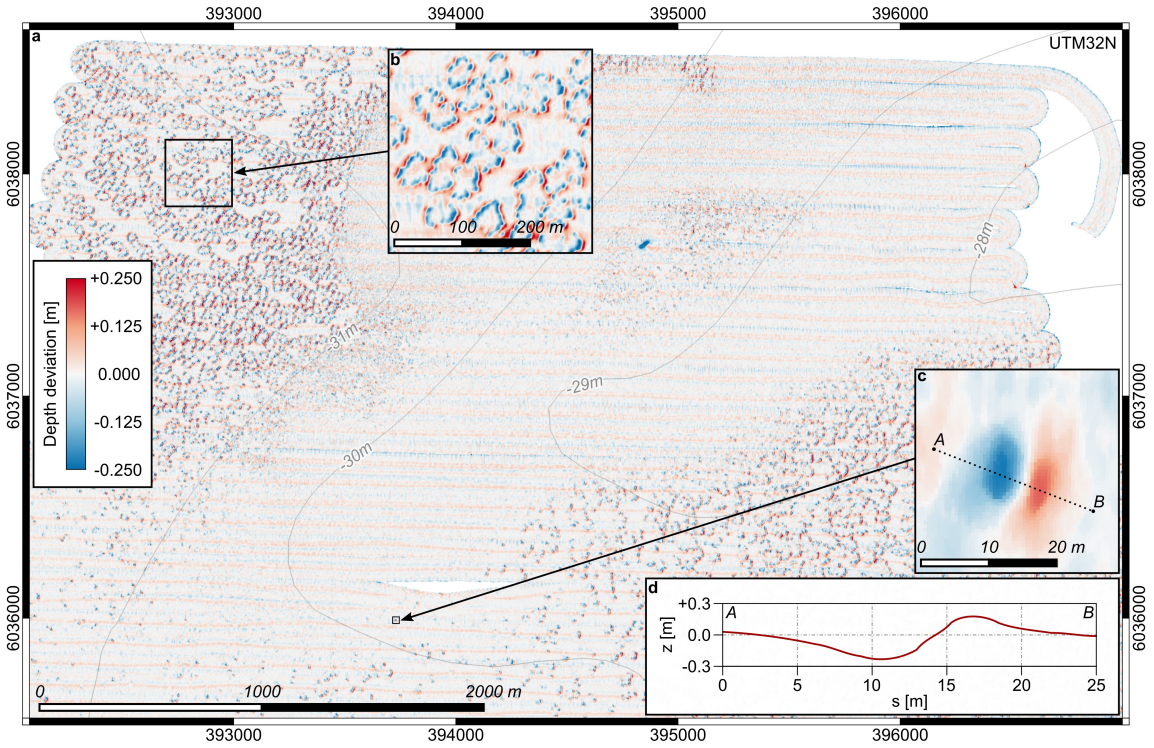

Figure 5.2: Pockmark density and morphology. (a) Zero-median bathymetry with full seafloor coverage from cruise HE470, August 2016. (b) Detail of pockmark cluster. (c) Detail of an individual pockmark. (d) Cross section along transect A–B. The maps were generated using QGIS Version 2.14.11 (QGIS Development Team, 2016). Depth contours were made available by project Geopotential Deutsche Nordsee (GPDN) (2013).

outbreak in autumn 2015, hydro-acoustic evidence for active seepage of gas was found only for a single pockmark. A two meter high flare was identified in both frequencies (LF: 8 kHz and HF: 100 kHz) of the SBP (Fig. 5.4b). In long transects crossing the pockmark field, a strong reflector located a few meters below the seafloor was commonly observed in the low frequency of the SBP (Fig. 5.4a,c). Drilling cores suggest that it indicates the transition from the Holocene to the Pleistocene sequence (Landesamt für Bergbau, Energie und Geologie (LBEG), 2014) (Fig. 5.4d). No pockmarks were found where the Holocene layer exceeded a critical thickness of around one meter (Fig. 5.4a).

5.4 POCKMARK MORPHOLOGY

The individual pockmarks consist of a well-defined crater with a neighboring mound (Fig. 5.2c,d). The majority of the mounds is located southeast of their associated troughs i.e., in the lee of the flood current and the dominant wave direction. A smaller part is located northwest i.e., in the lee of the ebb current (Fig. 5.1c). The plan of individual features is elliptical with the semi-major axis oriented northeast. Especially in regions of high areal density, the pockmarks appear in coherent ring-like structures and elongated troughs (Fig. 5.2b).

Backscatter intensity from MBES indicates zones of higher reflectivity inside the depressions, so called eyed pockmarks (Hovland and Judd, 1988). In underwater images, these zones were identified as accumulations of shell detritus. In contrast, the mounds consist of well-sorted fine sand virtually free from any shell detritus. This visual evidence supports a vigorous eruption process with subsequent settling of the suspended material as a function of grain size in the respective wave or current lee direction.

5.5 METHANE CONCENTRATIONS IN THE SEDIMENT AND IN THE WATER COLUMN

Within the pockmarked area, dissolved methane concentrations of 11.0 μmol l^{-1} to 30.4 μmol l^{-1} were detected in the pore water and overlying bottom water samples taken from sediment cores (Tab. A.1). These values are around ten times higher than reference concentrations outside the pockmark field in the southeastern German Bight where values between $<$0.1 μmol l^{-1} and 4.4 μmol l^{-1} were measured.

Gas measurements in the water column were carried out using a membrane-inlet mass spectrometer (MIMS). Seawater from 25 m water depth was pumped on board and continuously analyzed with the MIMS but no significant change of carbon dioxide or methane could be associated with pockmark locations, suggesting that gas seepage had ceased at the time of the survey.

5.6 POTENTIAL PRECONDITIONS AND TRIGGER MECHANISMS FOR POCKMARK FORMATION

The most probable gas source is biogenic methane from the microbial decomposition of wetland plant remains often found in the post-glacial river confluence of ancient rivers Eider and Elbe (Fig. 5.4d). Comparatively high bottom water temperatures in 2014 and 2015 (Fig. 5.3a) may have facilitated its ascent toward a shallow depth beneath the seafloor where it remained in an unstable state until it was released by a final trigger. The region is not affected by earthquakes, but man-made tremors were generated during the pile-driving works for the construction foundations of three offshore wind farms at the eastern end of the pockmark field between 2012 and 2014 (Fig. 5.1a). There are no records of magnitude of the vibrations on the seafloor but the energy of the blows is considered too low and presumably dampened too fast i.e., exponentially with increasing distance from the source (Masoumi and Degrande, 2008) to cause an ascent of gas as far as 30 km away from the wind farms.

The proposed trigger for the final outbreak of the gas from the shallow subsurface is a series of storms in November 2015 (Fig. 5.3b). Wave model hindcasts indicate significant wave heights exceeding 7 m in the pockmarked field (Helmholtz-Zentrum Geesthacht Zentrum für Material- und Küstenforschung GmbH (HZG), 2016). Typical wave peak periods measured during the winter storms in this area are in the order of 8 s to 12 s.

Following linear wave theory, this results in a wave length L of 96 m to 177 m for an average water depth d of 30 m and transitional conditions ($0.05 < d/L < 0.5$). The effect of wave orbital motion and pressure oscillations reaches depths of 48 m to 89 m. The surface pressure oscillations and the horizontal component of the orbital velocity are reduced to around 48% by wave attenuation at a depth of 30 m. Assuming a Raleigh distribution for the wave height spectrum, the highest 1% of the waves reach 11.7 m and a maximum wave height of 14 m is possible. This allows a penetration depth of the wave-induced effective stress of up to 3.5 m for the significant and 7 m for the maximum wave (Okusa, 1985).

From the evidence described above, the following formation mechanism for the characteristic pockmark craters and mounds can be deduced. Triggered by a relief of pressure under a passing wave trough, the stored gas erupts and ejects sediment into the water column. The suspended material then settles in the lee of wave or current direction (whichever is dominant at that time) in a distance from the eruption point as a function of grain size. While the coarser shell debris settles back into the eruption crater, the sandy fraction is settled in a well-defined mound and the fine fraction is transported further away. An alternative mechanism for the generation of the characteristic trough-mound structures is the generation of subsidence depressions after the gas is released and a generation of the mounds as secondary sorted bedforms from the initial defects (Venditti et al., 2005). Measured near-bottom current velocities measured reach 0.3 ms^{-1} during ebb and 0.4 ms^{-1} during flood. The resulting shear stresses are capable of moving the seafloor sediment and of generating small scale bedforms with centimeter height and decimeter length scales. The dimensions and morphology of the pockmarks are different from the typical triangular bedform cross-sections. Furthermore,a number of scour holes of around 0.5 m depth found in the area throughout all MBES surveys do not indicate any lateral mounds (Fig. 5.3c,d). Therefore, this formation mechanism is unlikely.

The storm events in fall 2015 that must have triggered the eruption of the pockmark field were not exceptionally extreme events. Wave heights of equal amplitude also occurred in the winters of 2013 – 2016 (Fig. 5.3b), but no pockmarks were found in the respective subsequent MBES surveys (see supplementary Fig. A.3). Although pockmarks have been observed for the first time in November 2015, it can be assumed that their emergence is a reappearing phenomenon. Following the release of the potential energy stored by the gas beneath the seafloor due to a storm event, a certain recovery period may be required to accumulate enough gas to create a new instable state. In the meantime, the shallow pockmarks as morphological symptoms of the gas release are leveled by wave and current action on the mobile sands.

As the exact date of the eruption cannot be determined, the recent morphology of the pockmarks depicts the combined effect of gas expulsion and successive scouring of the initial defects in the seafloor. While individual features can be traced throughout the calm period between February and August 2016, there is no overlap of pockmark morphologies from surveys at the beginning (HE455, Nov. 2015) and at the end (HE456, Feb.

2016) of the stormy season. The latest observed extent and the distribution of pockmarks within the field may be controlled by a) the extent and local source strength of the presumed methane reservoir, b) the thickness of the overlying Holocene layer and porosity and permeability of the sediment, c) the absolute water depth as lower limit for wave impact and d) the local variation of water depth and slope of the bathymetry providing exposure toward or shelter from wave and current action.

As this is the first description of pockmark emergence in the Helgoland Reef area, future surveys will have to shed light on the fate of the pockmarks after seepage has ceased and possible recurrence cycles of this phenomenon.

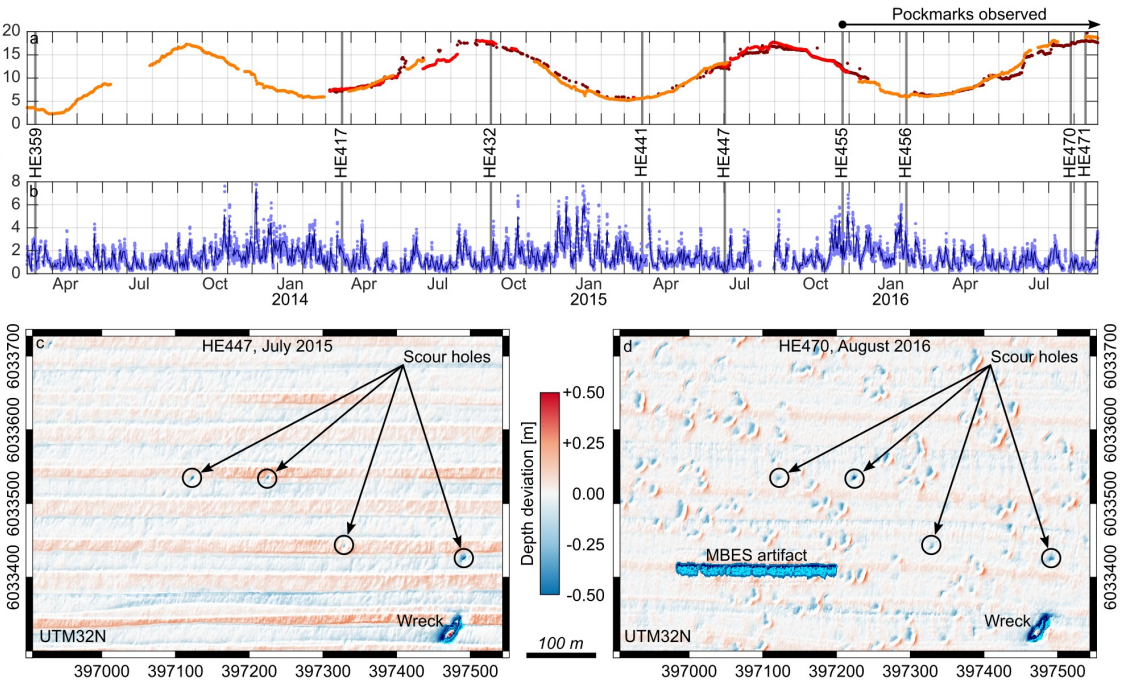

Figure 5.3: Emergence of the Helgoland Reef pockmarks. (a) Time series of bottom water temperature records from three stations in the German Bight. (b) Time series of significant wave height at Helgoland Reef from model hindcast. The data were provided by the COSYNA system (Helmholtz-Zentrum Geesthacht Zentrum für Material- und Küstenforschung GmbH (HZG), 2016) operated by Helmholtz-Zentrum Geesthacht Zentrum für Material- und Küstenforschung GmbH. (c,d) Zero-median bathymetries showing the emergence of the pockmarks. For the complete record of MBES bathymetries see supplementary Fig. A.3. The maps in this figure were generated using QGIS Version 2.14.11 (QGIS Development Team, 2016).

5.7 ESTIMATION OF RELEASED GAS VOLUME

The presumed trigger mechanism suggests that the eruption of the gas occurred in a short period of time and, except for a single pockmark, ongoing continuous seepage was not observed. For a conservative estimate of the volume of the released methane, it is assumed that no cavities but only the pore space of the relocated sediment was entirely

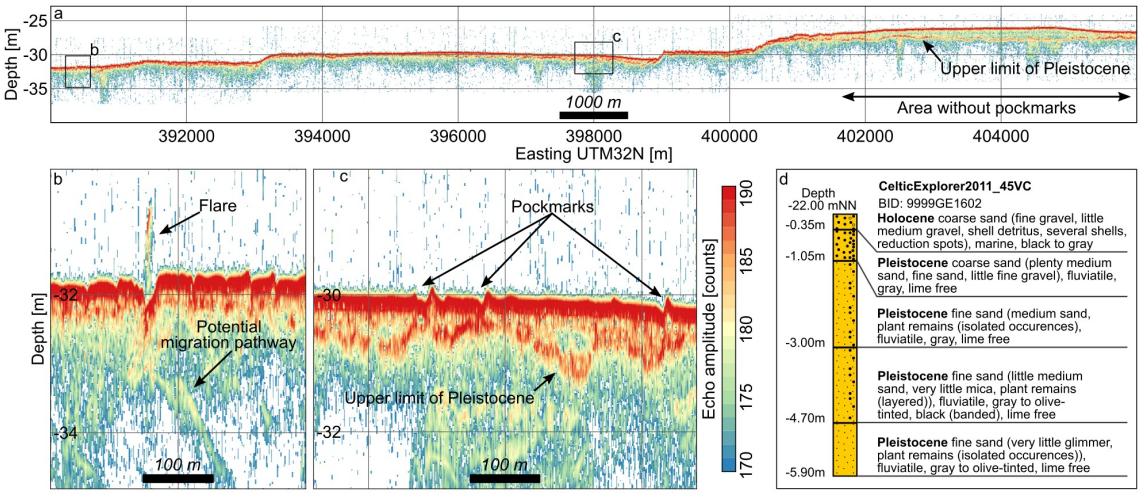

Figure 5.4: Geological setting of Helgoland Reef. (a) SBP transect across the pockmark field. (b) Detail of the methane flare. (c) Exemplary detail of pockmarks. (d) Description of core CE11_45VC (Landesamt für Bergbau, Energie und Geologie (LBEG), 2014). See Fig. 5.1 for the location of the SBP transect and the core.

filled with gas. This may define the upper physical limit of gas stored before eruption of the pockmarks. Assuming a density of 2.067 kg/m^3 (at 10°C and 30 m water depth) and a porosity of 0.35, the estimated gas phase removed with the relocated sediment amounts to around 5,000 t of methane. This is equivalent to 67% of the previously estimated annual methane flux from the entire North Sea (ca. 7,500 t/yr; (Bange et al., 1994)).

Methane seepages are often reported in water depth larger than 100 m and under stratified conditions (Fleischer et al., 2001). Such settings extend the period of availability of the gas for methane oxidizing bacteria and archaea which delays diffusive emission to the atmosphere (Steinle et al., 2016). Due to the shallow water depth and the energetic conditions at Helgoland Reef a large amount of the methane released from the subseafloor must have been emitted to the atmosphere (Borges et al., 2016).

An exact assessment of the marine contribution to atmospheric methane emissions is pending (Bange et al., 1994). High methane concentrations recently observed in coastal waters (Borges et al., 2016) may indicate an additional source of marine methane that has been neglected so far. Shallow methane reservoirs may be abundant in the post-glacial lowlands in the southern North Sea and other comparable shelf sea and coastal environments with organic-rich deposits worldwide (Szpak et al., 2015; Fandel et al., 2017b; Brothers et al., 2016). However, the abrupt and simultaneous emergence of more than 300,000 pockmarks in less than five months has not been reported so far. A possible explanation is that pockmarks, like other bedforms, are transient features especially in shallow and morphodynamically active shelf areas. The short appearance of pockmarks may not match the frequency of bathymetric surveys. In addition, the detection of the 0.2 m shallow pockmarks at the Helgoland Reef was only possible due to recent advances in mapping technology (Pratson and Edwards, 1996; Ernstsen et al., 2006). Similar pock-

mark fields in coastal areas and on continental shelves may have been overlooked to date.

5.8 METHODS

Bathymetry mapping and pockmark detection

The bathymetric surveys were conducted with a *Kongsberg EM® 710* multibeam echo sounder coupled with differential GPS positioning onboard R/V *Heincke*. Raw data were processed and gridded using the multibeam processing suite MB-System. The DDMs were further processed using GMT Version 4.5.1. To identify the shallow pockmark features against the larger variability in the bathymetry, a moving median filter with 50 m diameter was applied using the *grdfilter* function. The resulting background bathymetry was subtracted from the original DDMs producing zero-median DDMs. A depth contour of -0.05 m was selected to detect pockmarks in the zero-median DDMs. The resulting polygons were filtered in QGIS Version 2.14.11 (QGIS Development Team, 2016) to remove artifacts caused by ship motion that remain after motion compensation. Features with a minimum depth of less than 0.15 m, a median depth of less than 0.075 m and an area of less than 10 m^2 or greater than 500 m^2 were removed. Finally, obvious remaining artifacts were manually removed after visual inspection. The centroids of the remaining polygons were used to generate heat maps of pockmark density using the `gdal_grid` algorithm. Points were counted within a radius of 56.4 m, equaling an area of 0.01 km^2. The volume of relocated sediment was calculated from the zero-median DDMs using the *zonal statistics* function in QGIS with the -0.05 m contour lines as mask layer.

MBES data quality and scour holes

Prior to the first detection of the pockmarks during cruise HE455, an area of 5.5 km^2 had been surveyed with MBES repeatedly during cruises HE417, HE432, HE441, HE447 (Fig. 5.3 and supplementary Fig. A.2). The only notable morphological features, apart from a shipwreck at the bottom of a scour, were a number of circular depressions of around 0.5 m depth (Fig. 5.3c,d). On a recent high-resolution survey we found what we believe to be rounded boulders in their deepest points. The ability to resolve these features can be taken as proof of quality for the multibeam data. Although some of the surveys (especially HE455 and 456) were carried out in heavy sea state and exhibit artifacts from badly compensated ship motion, the ability to resolve the scour holes proves the reliability of the system. The holes can be found throughout all MBES surveys. When compared to the pockmarks, they are easily distinguishable as they are more circular in shape and lack the lateral mound.

Sub-bottom profiling

Sub-bottom profiles were recorded with a parametric echosounder (*Innomar SES-2000 medium*) with acoustic frequencies of 8 kHz and 100 kHz. The penetration of the low-frequency signal into the sandy seafloor was around 5 m below the seabed.

Methane detection

The sediment cores were taken with a MUC from the positions MUC1 to MUC6 inside the pockmark field and from several additional stations in the German Bight (Supplementary information, Tab. A.1, Fig. A.1). An acoustic ultra-short baseline (USBL) transponder (*iXblue GAPS Carbon V.1*) was used to record the position of the MUC on the seafloor. Pore water samples from MUC cores were taken at a depth of 0.05 m, transferred bubble-free and without a headspace into Exetainer (5.9 ml), fixated with 100 μl ZnCl (1 M) and stored cool and dark. In order to avoid methane loss or contamination, the samples were neither filtered nor was a vacuum applied during pore water sampling. Bottom water samples were taken from the overlying water of the MUC cores and treated in the same way as the pore water samples. The samples were analyzed in a MIMS under fully controlled temperature conditions. Calibration for methane concentration was carried out using standard methane mixtures (1.725 ppm (0.07 μmol l^{-1}); 209.7 ppm (8.8 μmol l^{-1}) and 1004 ppm (42.02 μmol l^{-1})).

During cruise HE470, MIMS measurements were performed on board measuring carbon dioxide and methane concentrations of bottom water that was pumped on deck. Due to lack of correct standard gas mixtures, only the potential changes in concentrations were studied.

ACKNOWLEDGEMENTS This study is funded through MARUM, the DFG Research Center and Cluster of Excellence 'The Ocean in the Earth System', the Max-Planck-Society, and by the BMBF FONA project NOAH. Ship time on R/V *Heincke* was made available based on proposals from FONA project NOAH and ASKAWZ II (funded by BSH) The authors express their sincere thanks to captain and crew of R/V *Heincke* who enabled the measurements even under severe weather conditions. A.Br. thanks Christian Knoblauch, Universität Hamburg for providing methane standards. The processing of multibeam data used for the preparation of this manuscript and the generation of maps was done entirely with free and open source software. K.K. thanks the developers behind MB-System, GMT, GDAL and QGIS.

AUTHOR CONTRIBUTIONS K.K. and C.W. drafted the manuscript with input from P.H., A.Br., A.N., A.B. and J.v.B. and in close discussion with G.H., S.A. and M.H.. K.K., G.H. and C.W. collected primary MBES data. K.K. processed and analyzed MBES data.

G.H. provided invaluable technical support during cruises HE395, HE417, HE441, HE447, HE470 and HE471. C.W. was scientific coordinator on cruises HE395, HE417, HE441, HE447 and HE470 and developed the survey and sampling procedure. J.v.B. coordinated cruise HE471. A.N. and A.Br. collected sediment cores during HE471. A.Br., A.N. and J.v.B. analyzed and interpreted methane concentrations in pore and bottom water samples. P.H. was scientific coordinator on cruises HE455 and HE456. M.H. and S.A. collected and analyzed water column MIMS data.

6

SUMMARY AND CONCLUSIONS

6.1 RIPPLE MORPHOLOGY

The overall range of ripple dimensions measured in the field can be predicted by empirical formulae. In direct comparison with measured average ripple heights, the current ripple predictors from Baas (1994) and Soulsby et al. (2012) and the wave ripple predictors from Li et al. (1996) and Soulsby et al. (2012) give the best results. Due to the spectral nature of 3D ripple morphology, heights of individual ripples may deviate significantly from the average value.

Detailed analysis of in situ measurements shows that average height of individual three-dimensional ripples under mixed wave and current forcing and possibly biogenic decay is overestimated by up to 40% when classical estimation based on the standard deviation of relief height is used. This leads to an overestimation of bedform related roughness by up to a factor of 2. Also, the recently described inhibiting influence of physical (Baas et al., 2013) and biogenic cohesion (Malarkey et al., 2015; Parsons et al., 2016) on bedform development is not covered by the classical bedform prediction models. Detailed in situ observations of the micro-bathymetry with high temporal (Δt~1 h) and spatial resolution ($\Delta x, \Delta y$~1 cm) are therefore required to obtain meaningful (average) ripple dimensions and to study their dynamic evolution.

From the observations of micro-bathymetry with acoustic (lander *SedObs*) and optical methods (lander *Lance*), it can be concluded that for sandy seafloor areas in the investigated depth range between 20 and 40 meters, bedform migration and related overturning of the upper few centimeters (the ripple height) of the seafloor is an omnipresent phenomenon. Bedform migration can be observed when the combined wave and current shear stress is above the critical threshold of motion for the sediment. The magnitude of the morphodynamic response is controlled by the variation of tidal forcing over the spring-neap cycle and seasonal variations of surface wave energy. Waves play an important role in enabling bedform migration rates in an order of their length scale over the period with supercritical tidal current shear stress of a few hours. While current shear stress is the driving force in defining the direction of migration, wave induced shear stress rather contributes a stirring effect enabling easier mobilization of the sediment. Waves may also be an important factor in reducing physical and biogenic cohesion by winnowing of fines and EPS from the sediment matrix.

6.2 BEDFORM-MODERATED BENTHIC OXYGEN FLUXES

The presence of a rippled seafloor topography enhances oxygen penetration depth by enhancing advective pore water flow driven by pressure gradients along the bedform. Whenever supercritical shear stresses for sediment transport exist, the migration of the ripples leads to temporal fluctuations of the penetration depth and generates a layer of up to 2.5 cm thickness with variable oxygen concentrations. Additionally, bedform migration reduces volumetric oxygen consumption by up to 50% as organic carbon, entrapped in the sediment pore space, is washed out of the overturned sediment.

6.3 PHYSICAL AND BIOGENIC REWORKING

Highly resolved observations of seafloor micro-bathymetry allow for a detection and quantification of physically (ripple migration) and biologically driven reworking (bioturbation) of the surface sediments. A number of observations at different locations and during different seasons in the German EEZ show that biogenic reworking is an omnipresent phenomenon. While previous studies (Rhoads, 1963; Cadée, 1976; Grant, 1983) have focused in reworking rates by individual species in specific areas, this study shows that bioturbation is a process of regional importance. Characteristic relocation pattern of surface sediment can be observed whenever wave and current shear stress are below the critical threshold of motion.

At the investigated sites, biogenic reworking rates are one order of magnitude smaller than physically driven reworking by bedform migration and reach up to 14% of the latter. The rates are strikingly similar among different locations and over different seasons, although one might expect differences between different benthic communities (Dauwe et al., 1998) and a response to environmental conditions (Maire et al., 2007). From the observations reported here, biogenic reworking can be described as a background process. Regularly or long-term observations at a specific site are required to further investigate the interrelations of physical and biogenic reworking.

Reduced biogenic reworking rates for immobile ripples under neap conditions and without measurable wave action suggest that the magnitude of biogenic reworking is linked to physical reworking by means of bedform migration. This may be caused either by increased maintenance activity of burrowing organisms who need to regain access to the water column or increased activity of deposit feeders to a replenished food source due to the entrapment of nutrients in the pore space of migrating bedforms.

Bioturbation is also active during periods of sub-threshold conditions for physical bedload transport. Therefore, it can be regarded as an efficient mechanism for sediment reworking, ventilation of the surface sediment and exchange of solutes and particles across the benthic interface, especially, at locations and during periods when wave- and current-induced shear stresses do not contribute to sediment overturning. It therefore

becomes important when making large scale estimations of e.g. microbial activity and benthic fluxes.

6.4 POCKMARK FORMATION

Successive MBES surveys over the same area at Helgoland Reef over a period of three years showed the abrupt and simultaneous emergence (between July and November 2015) of an estimated number of more than 300,000 pockmarks in an overall area covering around 915 km^2. The morphological features consist of shallow elliptical craters of around 10 by 20 m in semi-axis diameter and up to 0.25 m depth and lateral mounds of equal dimensions towards the lee side of dominant flood and wave direction in this area.

Methane concentrations of up to 30 μmol l^{-1} in the surface sediment, a factor of 10 higher than the background concentration in the surrounding inner German Bight (Tab. A.1), suggest vigorous methane eruptions as mechanism for the suspension of sediment and formation of the craters. Possible migration pathways linked with the surficial craters were detected as impedance disturbances by SBP in the upper few meters of the seafloor. During the eruption and possible secondary development of the initial defects into bedforms (Brothers et al., 2011), around 6,900,000 m^3 of sediment were relocated.

The first emergence coincides with the first notable storms with wave action able to reach the seafloor in around 35 m water depth. The eruption of the gas from shallow reservoirs is therefore suggested to be triggered by wave-induced pressure oscillations. Follow-up surveys in 2016–2018 show that *old* features generated during fall and possibly winter are preserved over the calm summer season but are leveled out after the next storm season. Comprehensive surveys of the entire field have not been repeated since 2016. Exemplary data recorded during passages of the field in 2017 and 2018 suggest that new pockmarks have appeared in the respective storm seasons.

Potential deeper gas reservoirs, triggers for the upward migration and reasons for pressure built-up in the shallow subsoil remain speculative. Due to the transient nature of the shallow features, they may have been overlooked as an important mechanism for sediment reworking and methane emissions on the seafloor in shallow sandy shelf areas. The fate of the pockmark field is undetermined to date, yet recent surveys indicate that the formation rate of new pockmarks has lessened if the eruptions have not fully ceased. The methane source may have been depleted or the field may have returned to a dormant state until enough pressure is rebuilt by further ascension of gas from a deeper source to start a new series of eruptions. Possible cycles or return periods can only be determined by repeated long term surveys.

6.5 GENERAL CONCLUSIONS

DRIVERS AND SCALES OF REWORKING MECHANISMS The examples presented in this thesis outline the wide range of temporal and spatial scales of recent sediment reworking mechanisms in shallow shelf seas. Relevant drivers for sediment reworking can be categorized as *physical*, *biogenic* and *anthropogenic*. In shallow shelf seas with energetic hydraulic forcing, the most dominant driver are wave- and current-induced shear stresses responsible for the generation and migration of small scale bedforms (ripples). Biogenic reworking, induced by burrowing and foraging activities of benthic fauna, yields rates an order of magnitude smaller and the time frame for undisturbed activity of the benthic macro fauna is limited to a few hours in tidally dominated areas.

Reworking rates can be expressed as overturned sediment volume per area and time [$m^3\ m^{-2}\ d^{-1}$], resulting in an apparent velocity [$m\ d^{-1}$]. The measured reworking rates due to ripple morphodynamics are in the order of 1×10^{-3} – 1×10^{-2} $m\ d^{-1}$. The rates of biogenic reworking are one order of magnitude lower and in the range of 1×10^{-4} – 1×10^{-3} $m\ d^{-1}$. Depending on the time frame of their emergence (days to months) the reworking rate by gas expulsion and generation of pockmarks at Helgoland Reef lies in a range of 1×10^{-4} – 1×10^{-3} $m\ d^{-1}$.

BRIDGING SCALES Ripple morphodynamics and bioturbation are small scale *instantaneous* processes acting over millimeters to decimeters and on governing cycles of seconds (wave period) over hours (tides) and weeks (spring-neap cycle) to months (seasonal meteorological forcing). Both spatially and temporarily highly resolved measurements are required to observe their dynamics and to evaluate their reworking potential. The ubiquity of these phenomena, however, makes their impacts important on regional (shelf wide) scale.

With bioturbation and fluid expulsion, two mechanisms are discussed here that have received less attention with respect to their meaning for sediment reworking in shallow coastal and shelf waters so far. Their impact may be an order of magnitude lower than that of bedload transport but they act in periods and regions not affected by wave and current forcing and therefore contribute an important share to overall overturning of seafloor sediments with implications for ecosystem functions of the seafloor.

INTERACTION BETWEEN DRIVERS AND ECOSYSTEM DYNAMICS Although occasionally the most dominant drivers of morphodynamics and boundary conditions for an ecosystem can be identified, the interaction between different drivers needs to be better understood to investigate the complex response of affected ecosystems. The impact of bedform topography and migration on oxygen dynamics and their implications for microbial processes was shown by Ahmerkamp (2016). The reaction of benthic macro-fauna on ripple migration presented in this thesis reveals another link between physical and biogenic mechanisms on larger (millimeter to centimeter) scale.

The eruption of methane and the formation of pockmarks are sudden disruptive events with high local impact on seafloor morphology and sediment sorting (Fig. 2.6). The newly generated heterogeneity, however, may serve as a long-term boost for diversity in the ecosystem (Dando et al., 1991; Wildish et al., 2008; Webb et al., 2009).

With respect to anthropogenic interests, the growing demand for suitable offshore building ground for renewable energy facilities may be adversely affected by the disturbances in geotechnical properties of the subsoil caused by upward migration of gas (Hovland, 1989). Although the surficial craters observed in the sandy sediment at Helgoland Reef are of small amplitude, their emergence may offset the morphodynamic equilibrium toward the formation of stable large scale bedforms eventually endangering the stability of offshore constructions by reducing their embedment depth.

FUTURE DEVELOPMENT The shelf seafloor worldwide is under high and increasing pressure: The challenge of feeding a growing world population has led to a large growth in fishing sector (Hollingsworth, 2018) and efforts to reduce its ecological impact proceed rather slowly (Boonstra et al., 2018). The growing demand for energy and the transition from nuclear and fossil towards renewable energy leads to an intense growth in the marine energy sector (Bilgili et al., 2011) and a search for suitable buildings grounds in offshore areas. Potentially rising frequencies and intensities of storm events in a changing climate (Leckebusch et al., 2006; Dettinger, 2011) may lead to increased wave action on seabed. A careful observation of changes in the main driving mechanisms is required to predict future implications for sediment dynamics which are a key element in the ecosystem function of the seafloor.

Due to many nonlinear interactions, a complex and dynamic system such as the shelf seafloor is sensitive to changing boundary conditions: The example of the sudden emergence of a large pockmark field in the shallow nearshore waters of the German Bight shows, that even though happening right at our doorstep, important phenomena on continental shelves have so far remained hidden from our view. In this context, a slow transition e.g. in bottom water temperatures may facilitate the ascent of gas from deeper reservoirs and lead to similar expulsions of methane in other shelf areas worldwide.

Given the meaning of shelf seafloor sediments as valuable resource and rich habitat, the study of sediment reworking mechanisms is needed to assess the boundary conditions for the interaction between physical, biological and chemical processes at the benthic interface.

7

OUTLOOK

NEW QUESTIONS This thesis gives an overview over recent sediment reworking mechanisms on continental shelves. While the relative importance and overall range of three exemplary processes have been discussed, the observations introduce a number of new questions.

Bedload sediment transport and ripple morphodynamics have been studied for more than 200 years. Yet, new observations show the gap between predictions based on empirical relations and conditions observed under natural conditions. Sedimentological properties such as the effect of multi-modal grain size distribution, physical and biogenic cohesion on the critical shear stress and initiation of motion have to be taken into account to enhance the prediction of sediment transport and reworking.

Systematic observations of biogenic reworking rates across different environments and seasons are required to understand effects of different benthic communities and temporal variations of their activity.

Future surveys are also needed to investigate the future development of the Helgoland pockmark field. A verification of the suggested initial geological setting, trigger mechanisms for the eruption of methane and possible recurrence intervals can help to identify other shelf areas in a similar state and eventually assess the contribution of this phenomenon to the global methane budget.

INTEGRATION OF METHODS AND TOOLS Detailed in situ observations are an important tool for the parametrization and quantification of reworking processes. Due to the great range of scales, appropriate methods and sampling strategies have to be selected to address specific processes. Large-scale and long-term effects can be observed with the help of shipboard hydroacoustics such as multibeam echosounder or sidescan sonar surveys. Short range optical methods such as photogrammetry or laser-scanning are valuable tools to obtain information on short-term dynamics of the micro-bathymetry and interaction of physical and biological processes (Schönke et al., 2017). Large-scale hydraulic and morphodynamic numerical models can be a helpful tool to assist the identification of representative areas and the definition of sampling strategies. In turn, in situ data is required for the parametrization and quantification of reworking processes which, integrated in large-scale models can be used for upscaling of results from exemplary data to obtain regional and global estimates of reworking rates and the exchange of nutrients and pollutants across the benthic interface. Weighing spatial and temporal coverage against required resolution, future challenges lie in the integration of local situ observations and regional numerical models.

A

APPENDIX

A.1 SUPPLEMENTARY MATERIAL

Methane concentrations from MUC samples can be found in Tab. A.1. The corresponding stations are marked in Fig. A.1. An overview of the seafloor coverage of the various MBES surveys mentioned is given in Fig. A.2. The evolution of the seafloor throughout the surveys and the appearance of pockmarks can be found in Fig. A.3.

Table A.1: Methane concentrations in pore and bottom water samples from the Helgoland Reef area and the wider German Bight during cruise HE471, September 2016

Sample	Method	C [$\mu mol\ l^{-1}$]
	Helgoland Reef	
Core 1	incubation	18.7
Core 2	incubation	36.5
MUC2	bottom water	30.4
MUC3	pore water	26.3
MUC4	bottom water	28.1
MUC4	pore water	11.0
MUC5	bottom water	28.8
MUC5	pore water	27.9
MUC6	bottom water	26.2
MUC6	pore water	16.8
	German Bight	
CCP-G	bottom water	4.4
CCP-G	pore water	3.0
NOAH-A	bottom water/incubation	1.0
NOAH-C	bottom water/incubation	3.2
NOAH-D	bottom water/incubation	<0.1
Tonne E3	bottom water/incubation	<0.1

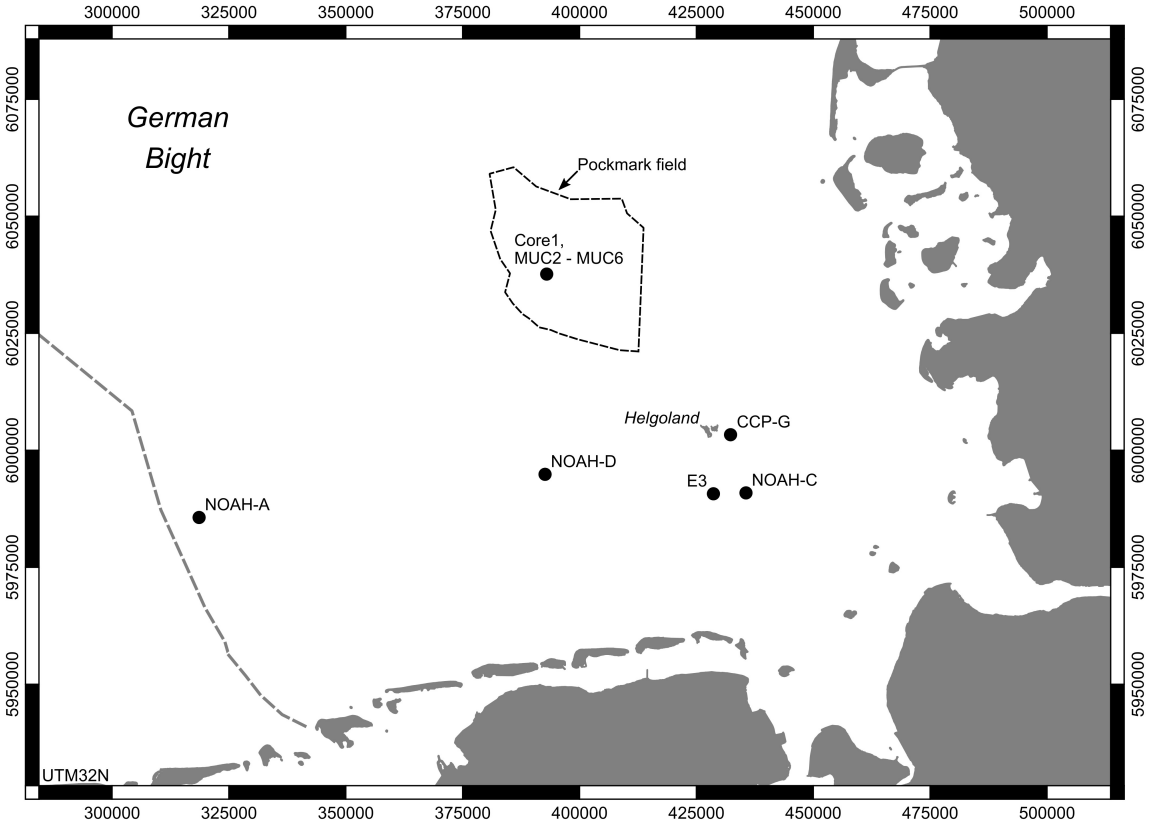

Figure A.1: Locations of sediment samples from Tab. A.1. The map was generated using QGIS Version 2.14.11 (QGIS Development Team, 2016). Maritime boundaries were made available by the EMODnet Human Activities project (European Marine Observation and Data Network (EMODnet), 2017), funded by the European Commission Directorate General for Maritime Affairs and Fisheries. Data were provided by the European Environment Agency. Land polygons ©OpenStreetMap OpenStreetMap (2016) (available under the Open Database License; see `www.open-streetmap.org/copyright`).

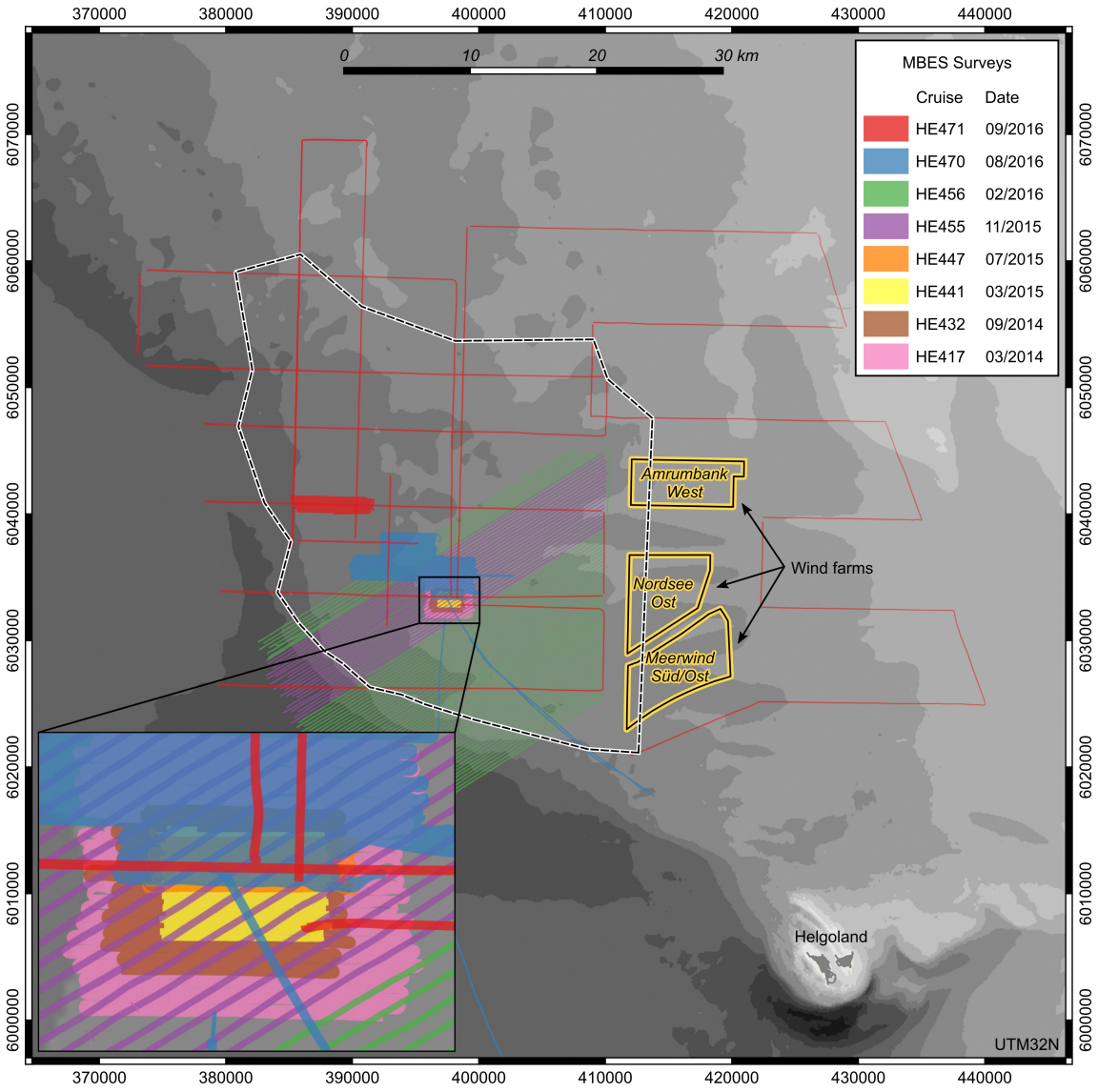

Figure A.2: Overview of MBES surveys. The seafloor coverage of MBES swaths is given in different color coding for the respective cruises. The map was generated using QGIS Version 2.14.11 (QGIS Development Team, 2016). Wind farm polygons were made available by the EMODnet Human Activities project(European Marine Observation and Data Network (EMODnet), 2017), funded by the European Commission Directorate General for Maritime Affairs and Fisheries. Wind farm data were collected by the OSPAR Commission. Bathymetry data were made available by the GPDN project4. Land polygons ©OpenStreetMap OpenStreetMap (2016) (available under the Open Database License; see www.openstreetmap.org/copyright).

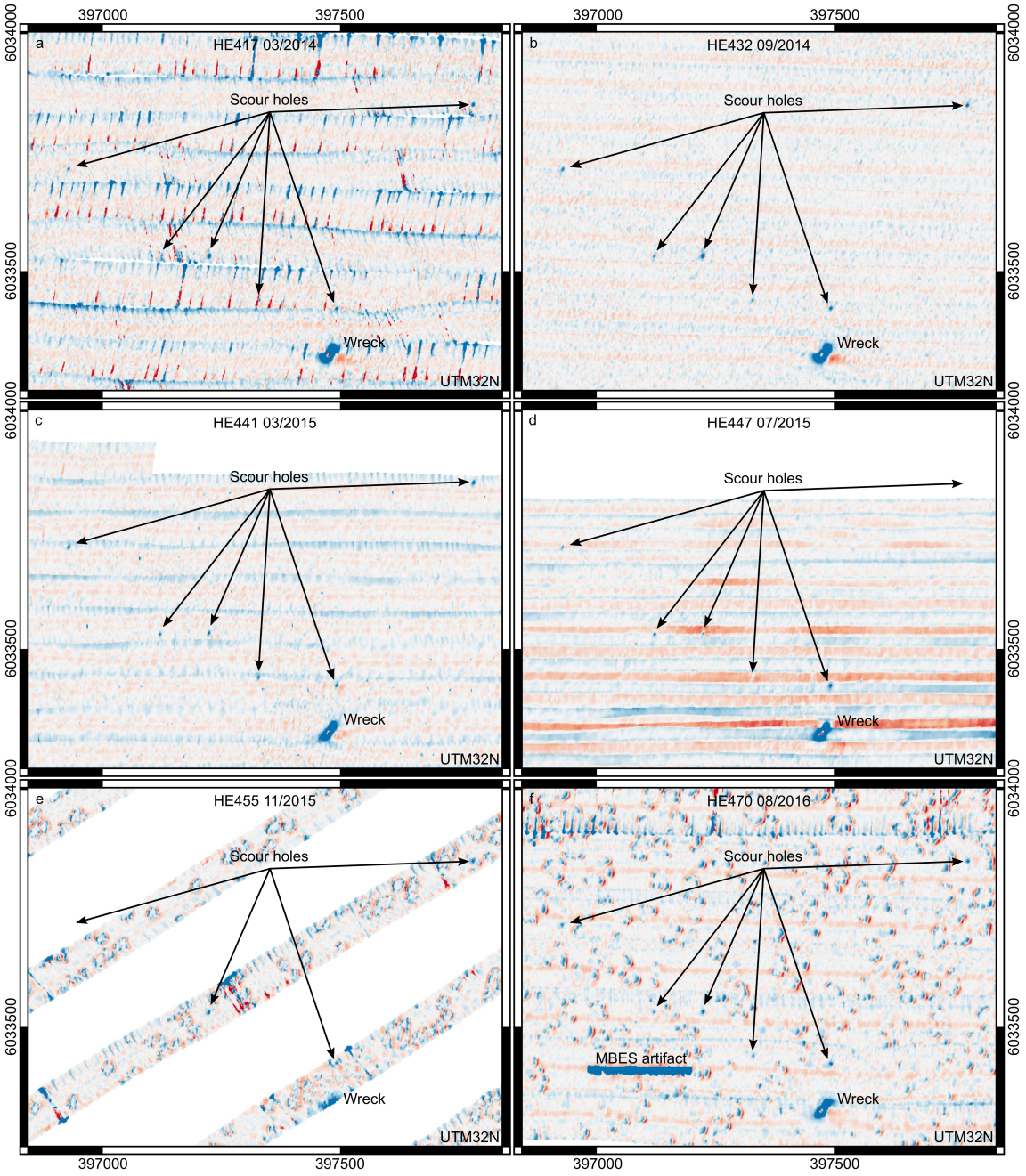

Figure A.3: Seafloor evolution and appearance of pockmarks. Pockmarks were first observed during cruise HE455 in November 2015 (e). In this area, they have changed in location and morphology when last observed during cruise HE470 in August 2016 (f). Some features are persistent: In the lower part of the figure the scour around a small ship wreck can be located as well as a few other small scour features possibly connected to boulders on the seafloor. The maps in this figure were generated using QGIS Version 2.14.11 (QGIS Development Team, 2016).

B

BIBLIOGRAPHY

M. Ahmad, P. Dong, M. Mamat, W. Wan Nik, and M. Mohd. The critical shear stresses for sand and mud mixtures. *Applied Mathematical Sciences*, 5(2):53–71, 2011.

S. Ahmerkamp. *Regulation of oxygen dynamics in sandy sediments*. PhD thesis, Universität Bremen, 2016.

S. Ahmerkamp, C. Winter, F. Janssen, M. M. M. Kuypers, and M. Holtappels. The impact of bedform migration on benthic oxygen fluxes. *J. Geophys. Res. Biogeosci.*, 120(11): 2229–2242, Jan. 2015.

S. Ahmerkamp, C. Winter, K. Krämer, D. de Beer, F. Janssen, J. Friedrich, M. M. Kuypers, and M. Holtappels. Regulation of benthic oxygen fluxes in permeable sediments of the coastal ocean. *Limnol. Oceanogr.*, 62(5):1935–1954, 2017.

S. Amirshahi, C. Winter, and E. Kwoll. Characteristics of instantaneous turbulent events in southern German Bight. In G. Constantinescu, M. Garcia, and D. Hanes, editors, *River Flow 2016*. Taylor & Francis, 2016.

S. M. Amirshahi, E. Kwoll, and C. Winter. Near bed suspended sediment flux by single turbulent events. *Cont. Shelf Res.*, 152:76–86, 2017.

C. Amos, A. Bowen, D. Huntley, and C. Lewis. Ripple generation under the combined influences of waves and currents on the Canadian continental shelf. *Cont. Shelf Res.*, 8 (10):1129–1153, 1988.

C. L. Amos and M. B. Collins. The combined effects of wave motion and tidal currents on the morphology of intertidal ripple marks; The Wash, U.K. *Journal of Sedimentary Research*, 48(3):849–856, Sept. 1978.

B. D. Andrews, L. L. Brothers, and W. A. Barnhardt. Automated feature extraction and spatial organization of seafloor pockmarks, Belfast Bay, Maine, USA. *Geomorphology*, 124(1–2):55–64, 2010.

J. H. Baas. *Dimensional analysis of current ripples in recent and ancient depositional environments*. PhD thesis, University of Utrecht, 1993.

J. H. Baas. A flume study on the development and equilibrium morphology of current ripples in very fine sand. *Sedimentology*, 41(2):185–209, 1994.

J. H. Baas, A. G. Davies, and J. Malarkey. Bedform development in mixed sand-mud: The contrasting role of cohesive forces in flow and bed. *Geomorphology*, 182:19–32, 2013.

J. H. Baas, J. L. Best, and J. Peakall. Predicting bedforms and primary current stratification in cohesive mixtures of mud and sand. *Journal of the Geological Society*, 173(1): 12–45, 2016.

M. Baeye and M. Fettweis. In situ observations of suspended particulate matter plumes at an offshore wind farm, southern North Sea. *Geo-Marine Letters*, 35(4):247–255, 2015.

H. W. Bange, U. H. Bartell, S. Rapsomanikis, and M. O. Andreae. Methane in the Baltic and North Seas and a reassessment of the marine emissions of methane. *Global Biogeochem. Cycles*, 8(4):465–480, 1994.

J. Bartholdy, V. B. Ernstsen, B. W. Flemming, C. Winter, A. Bartholomä, and A. Kroon. On the formation of current ripples. *Scientific Reports*, 5:11390, 2015.

B. Baschek, F. Schroeder, H. Brix, R. Riethmüller, T. H. Badewien, G. Breitbach, B. Brügge, F. Colijn, R. Doerffer, C. Eschenbach, J. Friedrich, P. Fischer, S. Garthe, J. Horstmann, H. Krasemann, K. Metfies, N. Ohle, W. Petersen, D. Pröfrock, R. Röttgers, M. Schlüter, J. Schulz, J. Schulz-Stellenfleth, E. Stanev, C. Winter, K. Wirtz, J. Wollschläger, O. Zielinski, and F. Ziemer. The Coastal Observing System for Northern and Arctic Seas (COSYNA). *Ocean Science*, 13(3):379, 2017.

P. Bell and P. Thorne. Application of a high resolution acoustic scanning system for imaging sea bed microtopography. In *Seventh International Conference on Electronic Engineering in Oceanography. Technology Transfer from Research to Industry*, Southampton, UK, June 1997.

P. S. Bell and P. D. Thorne. Field measurements of wave induced sand ripples in three dimensions. In *2nd International Conference on Underwater Acoustic Measurements: Technologies & Results*, Crete, Greece, June 2007.

K. Berkenbusch and A. A. Rowden. Factors influencing sediment turnover by the burrowing ghost shrimp *Callianassa filholi* (Decapoda: Thalassinidea). *Journal of Experimental Marine Biology and Ecology*, 238(2):283–292, 1999.

B. B. Bernard, J. M. Brooks, and W. M. Sackett. Light hydrocarbons in recent Texas continental shelf and slope sediments. *Journal of Geophysical Research: Oceans*, 83(C8): 4053–4061, 1978.

M. Bilgili, A. Yasar, and E. Simsek. Offshore wind power development in Europe and its comparison with onshore counterpart. *Renewable and Sustainable Energy Reviews*, 15(2): 905–915, 2011.

P. D. Boehm and A. Requejo. Overview of the recent sediment hydrocarbon geochemistry of Atlantic and Gulf Coast outer continental shelf environments. *Estuarine, coastal and shelf science*, 23(1):29–58, 1986.

W. J. Boonstra, M. Valman, and E. Björkvik. A sea of many colours – How relevant is Blue Growth for capture fisheries in the Global North, and vice versa? *Marine Policy*, 87:340–349, 2018.

A. V. Borges, W. Champenois, N. Gypens, B. Delille, and J. Harlay. Massive marine methane emissions from near-shore shallow coastal areas. *Sci Rep*, 6:27908, 2016.

B. P. Boudreau, M. Huettel, S. Forster, R. A. Jahnke, A. McLachlan, J. J. Middelburg, P. Nielsen, F. Sansone, G. Taghon, W. Van Raaphorst, et al. Permeable marine sediments: Overturning an old paradigm. *EOS, Transactions American Geophysical Union*, 82 (11):133–136, 2001.

K. H. Broach, M. F. Miller, and S. S. Bowser. Bioturbation by the common antarctic scallop (*Adamussium colbecki*) and ophiuroid (*Ophionotus victoriae*) under multi-year sea ice: Ecologic and stratigraphic implicationsantarctic epifauna bioturbation. *Palaios*, 31 (6):280–290, 2016.

D. S. Brothers, C. Ruppel, J. W. Kluesner, U. S. ten Brink, J. D. Chaytor, J. C. Hill, B. D. Andrews, and C. Flores. Seabed fluid expulsion along the upper slope and outer shelf of the U.S. Atlantic continental margin. *Geophys. Res. Lett.*, 41(1):2013GL058048, 2014.

L. L. Brothers, J. T. Kelley, D. F. Belknap, W. A. Barnhardt, and P. O. Koons. Pockmarks: Self-scouring seep features? In 7^{th} *International Conference on Gas Hydrates*, Edinburgh, Scotland, July 2011.

L. L. Brothers, C. Legere, J. E. H. Clarke, J. T. Kelley, W. A. Barnhardt, B. D. Andrews, and D. F. Belknap. Pockmarks in Passamaquoddy Bay, New Brunswick, Canada. *Geological Society, London, Memoirs*, 46(1):111–112, 2016.

G. Cadée. Sediment reworking by *Arenicola marina* on tidal flats in the Dutch Wadden Sea. *Netherlands Journal of Sea Research*, 10(4):440–460, 1976.

G. Cadée. Sediment reworking by the polychaete *Heteromastus filiformis* on a tidal flat in the Dutch Wadden Sea. *Netherlands Journal of Sea Research*, 13(3-4):441–456, 1979.

C.-T. A. Chen and A. V. Borges. Reconciling opposing views on carbon cycling in the coastal ocean: Continental shelves as sinks and near-shore ecosystems as sources of atmospheric CO_2. *Deep Sea Research Part II: Topical Studies in Oceanography*, 56(8-10): 578–590, 2009.

H. E. Clifton and J. R. Dingler. Wave-formed structures and paleoenvironmental reconstruction. *Marine Geology*, 60(1):165–198, 1984.

K. M. Cooper, C. R. B. Froján, E. Defew, M. Curtis, A. Fleddum, L. Brooks, and D. M. Paterson. Assessment of ecosystem function following marine aggregate dredging. *Journal of Experimental Marine Biology and Ecology*, 366(1-2):82–91, 2008.

P. J. Cowell and B. G. Thom. Morphodynamics of coastal evolution. In R. W. G. Carter and C. D. Woodroffe, editors, *Coastal evolution: Late Quaternary shoreline morphodynamics*, pages 33–86. Cambridge University Press, 1997.

P. Dando, M. Austen, R. Burke Jr, M. Kendall, M. Kennicutt, A. Judd, D. Moore, S. O'Hara, R. Schmalijohann, and A. Southward. Ecology of a north sea pockmark with an active methane seep. *Mar. Ecol. Prog. Ser.*, 70(1):49–63, 1991.

B. Dauwe, P. M. Herman, and H. Heip. Community structure and bioturbation potential of macrofauna at four North Sea stations with contrasting food supply. *Mar. Ecol. Prog. Ser.*, 173:67–83, 1998.

G. Davies. *Algal-laminated sediments, Gladstone Embayment, Shark Bay, Western Australia*. AAPG Special Volumes, 1970.

M. Desprez. Physical and biological impact of marine aggregate extraction along the French coast of the Eastern English Channel: Short-and long-term post-dredging restoration. *ICES Journal of Marine Science*, 57(5):1428–1438, 2000.

M. Dettinger. Climate change, atmospheric rivers, and floods in California – A multimodel analysis of storm frequency and magnitude changes. *JAWRA Journal of the American Water Resources Association*, 47(3):514–523, 2011.

L. Dimitrov and J. Woodside. Deep sea pockmark environments in the eastern Mediterranean. *Marine Geology*, 195(1–4):263–276, 2003.

R. Durán and J. Guillén. Continental Shelf Landforms. In *Submarine Geomorphology*, pages 185–206. Springer, 2018.

EAK. Empfehlungen A 2002 – Äußere Belastung als Grundlage für Planung und Bemessung von Küstenschutzwerken. *Die Küste*, 65:1–302, 2002.

J. P. Ellis and W. T. McGuinness. Pockmarks of the Northwestern Arabian Gulf. In *Oceanology*, volume 6 of *Advances in Underwater Technology, Ocean Science and Offshore Engineering*, pages 353–367. Springer, 1986.

V. B. Ernstsen, R. Noormets, D. Hebbeln, A. Bartholomä, and B. W. Flemming. Precision of high-resolution multibeam echo sounding coupled with high-accuracy positioning in a shallow water coastal environment. *Geo-Mar Lett*, 26(3):141–149, 2006.

V. B. Ernstsen, C. Winter, M. Becker, and J. Bartholdy. On the dynamics of compound bedforms in high-energy tidal channels: Field observations in the German Bight and the Danish Wadden Sea. In *EGU General Assembly Conference Abstracts*, volume 12, page 13739, 2010.

European Marine Observation and Data Network (EMODnet). EMODnet Human Activities, 2017. URL http://www.emodnet-humanactivities.eu.

C. L. Fandel, T. C. Lippmann, D. L. Foster, and L. L. Brothers. Observations of pockmark flow structure in Belfast Bay, Maine, Part 3: Implications for sediment transport. *Geo-Mar Lett*, 37(1):23–34, 2017a.

C. L. Fandel, T. C. Lippmann, D. L. Foster, and L. L. Brothers. Observations of pockmark flow structure in Belfast Bay, Maine, Part 2: Evidence for cavity flow. *Geo-Mar Lett*, 37 (1):15–22, 2017b.

C. L. Fandel, T. C. Lippmann, J. D. Irish, and L. L. Brothers. Observations of pockmark flow structure in Belfast Bay, Maine, Part 1: Current-induced mixing. *Geo-Mar Lett*, 37 (1):1–14, 2017c.

M. E. Field and A. E. Jennings. Seafloor gas seeps triggered by a northern California earthquake. *Marine Geology*, 77(1–2):39–51, 1987.

K. Figge. Das Elbe-Urstromtal im Bereich der Deutschen Bucht (Nordsee). *E&G–Quaternary Science Journal*, 30(1):302–311, 1980.

K. Figge. *Karte zur Sedimentverteilung im Bereich der Deutschen Bucht im Massstab 1:250000*. Bundesanstalt für Seeschifffahrt und Hydrographie, Hamburg, Germany, 1981.

P. Fleischer, T. Orsi, M. Richardson, and A. Anderson. Distribution of free gas in marine sediments: A global overview. *Geo-Mar Lett*, 21(2):103–122, 2001.

B. Flemming. Zur Klassifikation subaquatischer, strömungstransversaler Transportkörper. *Bochumer geologische und geotechnische Arbeiten*, 29(93–97):44–47, 1988.

S. Forster and G. Graf. Impact of irrigation on oxygen flux into the sediment: Intermittent pumping by callianassa subterranea and "piston-pumping" by *Lanice conchilega*. *Mar. Biol.*, 123(2):335–346, 1995.

H. Friedrich, A. Paarlberg, and J. Lansink. Evaluation of statistical properties of dune profiles. In *Proc. of the 5th IAHR symposium on River, Coastal and Estuarine Morphodynamics*, volume 2, pages 913–921, Enschede, the Netherlands, 2007.

Geopotential Deutsche Nordsee (GPDN). Bathymetrie, Intervalle mit 1 m und 5 m Abstand, 2013. URL http://www.gpdn.de/.

M. Gogina, C. Morys, S. Forster, U. Gräwe, R. Friedland, and M. L. Zettler. Towards benthic ecosystem functioning maps: Quantifying bioturbation potential in the German part of the Baltic Sea. *Ecological indicators*, 73:574–588, 2017.

J. Grant. The relative magnitude of biological and physical sediment reworking in an intertidal community. *J. Mar. Res.*, 41(4):673–689, 1983.

W. D. Grant and O. S. Madsen. Combined wave and current interaction with a rough bottom. *J. Geophys. Res.*, 84(C4):1797–1808, Apr. 1979.

W. D. Grant and O. S. Madsen. Movable bed roughness in unsteady oscillatory flow. *Journal of Geophysical Research: Oceans*, 87(C1):469–481, 1982.

W. D. Grant and O. S. Madsen. The continental-shelf bottom boundary layer. *Annu. Rev. Fluid Mech.*, 18(1):265–305, 1986.

J. P. Grotzinger and R. E. Milliken. *Sedimentary Geology of Mars*. SEPM (Society for Sedimentary Geology), 2012.

B. S. Halpern, S. Walbridge, K. A. Selkoe, C. V. Kappel, F. Micheli, C. D'agrosa, J. F. Bruno, K. S. Casey, C. Ebert, H. E. Fox, et al. A global map of human impact on marine ecosystems. *Science*, 319(5865):948–952, 2008.

C. K. Harris and P. L. Wiberg. A two-dimensional, time-dependent model of suspended sediment transport and bed reworking for continental shelves. *Computers & Geosciences*, 27(6):675–690, 2001.

T. Hasiotis, G. Papatheodorou, N. Kastanos, and G. Ferentinos. A pockmark field in the Patras Gulf (Greece) and its activation during the 14/7/93 seismic event. *Marine Geology*, 130(3):333–344, 1996.

A. E. Hay and T. Mudge. Principal bed states during SandyDuck97: Occurrence, spectral anisotropy, and the bed state storm cycle. *J. Geophys. Res.*, 110(C3):C03013, Mar. 2005.

A. E. Hay and D. J. Wilson. Rotary sidescan images of nearshore bedform evolution during a storm. *Marine Geology*, 119(1–2):57–65, June 1994.

Helmholtz-Zentrum Geesthacht Zentrum für Material- und Küstenforschung GmbH (HZG). Cosyna data web portal CODM, 2016. URL http://codm.hzg.de/codm/.

Helmholtz-Zentrum Geesthacht Zentrum für Material- und Küstenforschung GmbH (HZG). coastmap geoportal, 2017. URL www.coastmap.org.

F. Hjulstrom. Studies of the morphological activity of rivers as illustrated by the River Fyris, Bulletin. *Geological Institute Upsalsa*, 25:221–527, 1935.

P. Hoekstra, P. Bell, P. van Santen, N. Roode, F. Levoy, and R. Whitehouse. Bedform migration and bedload transport on an intertidal shoal. *Cont. Shelf Res.*, 24(11):1249–1269, 2004.

A. Hollingsworth. Sustainable diets: The gulf between management strategies and the nutritional demand for fish. In *Handbook of Sustainability Science and Research*, pages 711–725. Springer, 2018.

M. Hovland. The formation of pockmarks and their potential influence on offshore construction. *Quarterly Journal of Engineering Geology and Hydrogeology*, 22(2):131–138, 1989.

M. Hovland. Submarine gas seepage in the North Sea and adjacent areas. *Petroleum Geology Conference series*, 4:1333–1338, 1993.

M. Hovland and A. Judd. *Seabed pockmarks and seepages: Impact on geology, biology, and the marine environment*. Springer, 1988.

M. Hovland, A. G. Judd, and L. H. King. Characteristic features of pockmarks on the North Sea Floor and Scotian Shelf. *Sedimentology*, 31(4):471–480, 1984.

M. Hovland, A. Judd, and R. Burke Jr. The global flux of methane from shallow submarine sediments. *Chemosphere*, 26(1-4):559–578, 1993.

M. Huettel, W. Ziebis, and S. Forster. Flow-induced uptake of particulate matter in permeable sediments. *Limnol. Oceanogr.*, 41(2):309–322, 1996.

A. Immenhauser. Estimating palaeo-water depth from the physical rock record. *Earth-Science Reviews*, 96(1-2):107–139, 2009.

G. H. Isaksen. Central North Sea hydrocarbon systems: Generation, migration, entrapment, and thermal degradation of oil and gas. *AAPG bulletin*, 88(11):1545–1572, 2004.

R. Jahnke, M. Richards, J. Nelson, C. Robertson, A. Rao, and D. Jahnke. Organic matter remineralization and porewater exchange rates in permeable South Atlantic Bight continental shelf sediments. *Cont. Shelf Res.*, 25(12-13):1433–1452, 2005.

F. Janssen. *Pore-water advection and organic matter mineralization in North Sea shelf sands*. PhD thesis, Universität Bremen, 2004.

A. Judd. Pockmarks in the UK sector of the North Sea. Technical report, UK Department of Trade and Industry Strategic Environmental Assessment, 2001.

A. Judd and M. Hovland. *Seabed Fluid Flow: The Impact on Geology, Biology and the Marine Environment*. Cambridge University Press, 2009.

N. B. Kachel and R. W. Sternberg. Transport of bedload as ripples during an ebb current. *Marine Geology*, 10(4):229–244, 1971.

N. Kenyon and A. Stride. The tide-swept continental shelf sediments between the Shetland Isles and France. *Sedimentology*, 14(3-4):159–173, 1970.

L. H. King and B. MacLean. Pockmarks on the Scotian Shelf. *Geological Society of America Bulletin*, 81(10):3141–3148, 1970.

M. A. F. Knaapen. Sandwave migration predictor based on shape information. *J. Geophys. Res.*, 110(F4), 2005.

W. Köhn. Die nacheiszeitliche Entwicklung der südlichen Nordsee. *Hannoversche Geographische Arbeiten*, 45:1–177, 1991.

B. J. Koo and J. Seo. Sediment reworking by a polychaete, *Perinereis aibuhitensis*, in the intertidal sediments of the Gomso Bay, Korea. *Ocean Science Journal*, 52(4):511–518, 2017.

F. Kösters and C. Winter. Exploring German Bight coastal morphodynamics based on modelled bed shear stress. *Geo-Marine Letters*, 34(1):21–36, 2014.

K. Krämer and C. Winter. Predicted ripple dimensions in relation to the precision of in situ measurements in the southern North Sea. *Ocean Science*, 12(6):1221, 2016.

J. Kudenov. Rates of seasonal sediment reworking in *Axiothella rubrocincta* (polychaeta: Maldanidae). *Mar. Biol.*, 70(2):181–186, 1982.

Y. Kumar, J. Ringenberg, S. S. Depuru, V. K. Devabhaktuni, J. W. Lee, E. Nikolaidis, B. Andersen, and A. Afjeh. Wind energy: Trends and enabling technologies. *Renewable and Sustainable Energy Reviews*, 53:209–224, 2016.

M. P. Lamb, W. E. Dietrich, and J. G. Venditti. Is the critical Shields stress for incipient sediment motion dependent on channel-bed slope? *Journal of Geophysical Research: Earth Surface*, 113(F2), 2008.

Landesamt für Bergbau, Energie und Geologie (LBEG). NIBIS® Mapserver: Boreholes and profiles, 2014. URL http://memas02.lbeg.de/BohrsaeulenGeodin/Bohrungsseite.aspx?BID=9999GE1602&Seite=1&ART=BDN.

G. C. Leckebusch, B. Koffi, U. Ulbrich, J. G. Pinto, T. Spangehl, and S. Zacharias. Analysis of frequency and intensity of European winter storm events from a multi-model perspective, at synoptic and regional scales. *Climate Research*, 31(1):59–74, 2006.

A. Lefebvre. *Bed roughness over vegetated beds*. PhD thesis, University of Southampton, 2009.

A. Lefebvre, V. B. Ernstsen, and C. Winter. Influence of compound bedforms on hydraulic roughness in a tidal environment. *Ocean Dynamics*, 61(12):2201–2210, 2011.

A. Lefebvre, A. J. Paarlberg, and C. Winter. Characterising natural bedform morphology and its influence on flow. *Geo-Marine Letters*, 36(5):379–393, 2016.

M. Z. Li and C. L. Amos. Predicting ripple geometry and bed roughness under combined waves and currents in a continental shelf environment. *Cont. Shelf Res.*, 18(9):941–970, 1998.

M. Z. Li and C. L. Amos. Field observations of bedforms and sediment transport thresholds of fine sand under combined waves and currents. *Marine Geology*, 158(1-4):147–160, 1999.

M. Z. Li, L. Wright, and C. L. Amos. Predicting ripple roughness and sand resuspension under combined flows in a shoreface environment. *Marine Geology*, 130(1):139–161, 1996.

T. Luckner and U. Zanke. An analytical solution for calculating the initiation of sediment motion. *International Journal of Sediment Research*, 22(2):87–102, 2007.

I. Maier and A. E. Hay. Occurrence and orientation of anorbital ripples in near-shore sands. *J. Geophys. Res.*, 114(F4), 2009.

O. Maire, J. Duchêne, A. Grémare, V. Malyuga, and F. Meysman. A comparison of sediment reworking rates by the surface deposit-feeding bivalve Abra ovata during summertime and wintertime, with a comparison between two models of sediment reworking. *Journal of Experimental Marine Biology and Ecology*, 343(1):21–36, 2007.

O. Maire, P. Lecroart, F. Meysman, R. Rosenberg, J.-C. Duchêne, and A. Grémare. Quantification of sediment reworking rates in bioturbation research: a review. *Aquatic Biology*, 2:219–238, 2008.

J. Malarkey, J. H. Baas, J. A. Hope, R. J. Aspden, D. R. Parsons, J. Peakall, D. M. Paterson, R. J. Schindler, L. Ye, I. D. Lichtman, S. J. Bass, A. G. Davies, A. J. Manning, and P. D. Thorne. The pervasive role of biological cohesion in bedform development. *Nat Commun*, 6:6257, Feb. 2015.

Marine Electronics Ltd. 3D Profiling Sonar - Model 2001 Datasheet, 2004. URL http://www.marine-electronics.co.uk/brochures/3DSonar/2001.pdf. Accessed: 2015-03-23.

R. L. Marinelli, R. A. Jahnke, D. B. Craven, J. R. Nelson, and J. E. Eckman. Sediment nutrient dynamics on the South Atlantic Bight continental shelf. *Limnol. Oceanogr.*, 43 (6):1305–1320, 1998.

H. R. Masoumi and G. Degrande. Numerical modeling of free field vibrations due to pile driving using a dynamic soil-structure interaction formulation. *Journal of Computational and Applied Mathematics*, 215(2):503–511, 2008.

S. Masoumi, L. Reuning, S. Back, A. Sandrin, and P. A. Kukla. Buried pockmarks on the Top Chalk surface of the Danish North Sea and their potential significance for interpreting palaeocirculation patterns. *Int J Earth Sci (Geol Rundsch)*, 103(2):563–578, 2014.

I. McCave. Sand waves in the North Sea off the coast of Holland. *Marine geology*, 10(3): 199–225, 1971.

F. Mermillod-Blondin and R. Rosenberg. Ecosystem engineering: the impact of bioturbation on biogeochemical processes in marine and freshwater benthic habitats. *Aquatic Sciences*, 68(4):434–442, 2006.

F. J. Meysman, O. S. Galaktionov, B. Gribsholt, and J. J. Middelburg. Bio-irrigation in permeable sediments: an assessment of model complexity. *J. Mar. Res.*, 64(4):589–627, 2006a.

F. J. Meysman, J. J. Middelburg, and C. H. Heip. Bioturbation: A fresh look at darwin's last idea. *Trends in Ecology & Evolution*, 21(12):688–695, 2006b.

H. Mitchener and H. Torfs. Erosion of mud/sand mixtures. *Coastal engineering*, 29(1-2): 1–25, 1996.

C. Morys, M. Powilleit, and S. Forster. Bioturbation in relation to the depth distribution of macrozoobenthos in the southwestern Baltic Sea. *Mar. Ecol. Prog. Ser.*, 579:19–36, 2017.

T. Mudge and V. Polonichko. Comparing Acoustic Doppler Velocimeters' Current and Wave Measurements. In *EGS - AGU - EUG Joint Assembly*, Apr. 2003.

F. E. Muller-Karger, R. Varela, R. Thunell, R. Luerssen, C. Hu, and J. J. Walsh. The importance of continental margins in the global carbon cycle. *Geophys. Res. Lett.*, 32(1), 2005.

T. Nagel, J. Chauchat, A. Wirth, and C. Bonamy. On the multi-scale interactions between an offshore-wind-turbine wake and the ocean-sediment dynamics in an idealized framework – A numerical investigation. *Renewable Energy*, 115:783–796, 2018.

T. R. Nelson and G. Voulgaris. A spectral model for estimating temporal and spatial evolution of rippled seabeds. *Ocean Dynamics*, 65(2):155–171, Dec. 2014.

T. R. Nelson, G. Voulgaris, and P. Traykovski. Predicting wave-induced ripple equilibrium geometry. *J. Geophys. Res. Oceans*, 118(6):3202–3220, June 2013.

F. H. Nichols. Sediment turnover by a deposit-feeding polychaete. *Limnol. Oceanogr.*, 19 (6):945–950, 1974.

H. Niemann, M. Elvert, M. Hovland, B. Orcutt, A. Judd, I. Suck, J. Gutt, S. Joye, E. Damm, K. Finster, and A. Boetius. Methane emission and consumption at a North Sea gas seep (Tommeliten area). *Biogeosciences Discussions*, 2(4):1197–1241, 2005.

V. I. Nikora and D. G. Goring. Fluctuations of suspended sediment concentration and turbulent sediment fluxes in an open-channel flow. *Journal of Hydraulic Engineering*, 128 (2):214–224, 2002.

C. A. Nittrouer and L. D. Wright. Transport of particles across continental shelves. *Rev. Geophys.*, 32(1):85–113, 1994.

S. W. Nixon. Remineralization and nutrient cycling in coastal marine ecosystems. In *Estuaries and nutrients*, pages 111–138. Springer, 1981.

F. K. Oberle, C. D. Storlazzi, and T. J. Hanebuth. What a drag: Quantifying the global impact of chronic bottom trawling on continental shelf sediment. *J. Mar. Syst.*, 159: 109–119, 2016.

K. O'Driscoll, B. Mayer, T. Ilyina, and T. Pohlmann. Modelling the cycling of persistent organic pollutants (pops) in the north sea system: Fluxes, loading, seasonality, trends. *J. Mar. Syst.*, 111:69–82, 2013.

T. Oehler, M. Schlüter, and U. Schückel. Seasonal dynamics of the biogenic silica cycle in surface sediments of the Helgoland Mud Area (southern North Sea). *Cont. Shelf Res.*, 107:103–114, 2015.

S. Okusa. Wave-induced stresses in unsaturated submarine sediments. *Géotechnique*, 35 (4):517–532, 1985.

OpenStreetMap. Planet dump retrieved from https://planet.osm.org , 2016. URL https://www.openstreetmap.org.

T. Pähtz and O. Durán. Fluid forces or impacts: What governs the entrainment of soil particles in sediment transport mediated by a Newtonian fluid? *Physical Review Fluids*, 2(7):074303, 2017.

D. R. Parsons, R. J. Schindler, J. A. Hope, J. Malarkey, J. H. Baas, J. Peakall, A. J. Manning, L. Ye, S. Simmons, D. M. Paterson, et al. The role of biophysical cohesion on subaqueous bed form size. *Geophys. Res. Lett.*, 43(4):1566–1573, 2016.

D. M. Paterson. Microbiological mediation of sediment structure and behaviour. In *Microbial mats*, pages 97–109. Springer, 1994.

P. R. Pinet. *Invitation to oceanography*. Jones & Bartlett Publishers, 2011.

L. F. Pratson and M. H. Edwards. Introduction to advances in seafloor mapping using sidescan sonar and multibeam bathymetry data. *Marine Geophysical Researches*, 18(6): 601–605, 1996.

QGIS Development Team. QGIS Geographic Information System, 2016. URL http://qgis.osgeo.org.

A. M. Queirós, S. N. Birchenough, J. Bremner, J. A. Godbold, R. E. Parker, A. Romero-Ramirez, H. Reiss, M. Solan, P. J. Somerfield, C. Colen, et al. A bioturbation classification of European marine infaunal invertebrates. *Ecology and evolution*, 3(11):3958–3985, 2013.

A. Reusch, M. Loher, D. Bouffard, J. Moernaut, F. Hellmich, F. S. Anselmetti, S. M. Bernasconi, M. Hilbe, A. Kopf, M. D. Lilley, G. Meinecke, and M. Strasser. Giant lacustrine pockmarks with subaqueous groundwater discharge and subsurface sediment mobilization. *Geophys. Res. Lett.*, 42(9):2015GL064179, 2015.

D. C. Rhoads. Rates of sediment reworking by *Yoldia limatula* in Buzzards Bay, Massachusetts, and Long Island Sound. *Journal of Sedimentary Research*, 33(3):723–727, 1963.

D. C. Rhoads and L. F. Boyer. The effects of marine benthos on physical properties of sediments. In *Animal-sediment relations*, pages 3–52. Springer, 1982.

C. Rocha. Sandy sediments as active biogeochemical reactors: Compound cycling in the fast lane. *Aquatic Microbial Ecology*, 53(1):119–127, 2008.

S. Rodrigues, C. Restrepo, E. Kontos, R. T. Pinto, and P. Bauer. Trends of offshore wind projects. *Renewable and Sustainable Energy Reviews*, 49:1114–1135, 2015.

J. N. Rogers, J. T. Kelley, D. F. Belknap, A. Gontz, and W. A. Barnhardt. Shallow-water pockmark formation in temperate estuaries: A consideration of origins in the western gulf of Maine with special focus on Belfast Bay. *Marine Geology*, 225(1–4):45–62, 2006.

K. M. Scanlon and H. J. Knebel. Pockmarks in the floor of Penobscot Bay, Maine. *Geo-Marine Letters*, 9(1):53–58, 1989.

R. J. Schindler, D. R. Parsons, L. Ye, J. A. Hope, J. H. Baas, J. Peakall, A. J. Manning, R. J. Aspden, J. Malarkey, S. Simmons, et al. Sticky stuff: Redefining bedform prediction in modern and ancient environments. *Geology*, 43(5):399–402, 2015.

M. Schönke, P. Feldens, D. Wilken, S. Papenmeier, C. Heinrich, J. S. von Deimling, P. Held, and S. Krastel. Impact of *Lanice conchilega* on seafloor microtopography off the island of Sylt (German Bight, SE North Sea). *Geo-Marine Letters*, 37(3):305–318, 2017.

B. M. Schroot, G. T. Klaver, and R. T. E. Schüttenhelm. Surface and subsurface expressions of gas seepage to the seabed: Examples from the Southern North Sea. *Marine and Petroleum Geology*, 22(4):499–515, 2005.

A. Shields. *Anwendung der Ähnlichkeitsmechanik und der Turbulenzforschung auf die Geschiebebewegung*. PhD thesis, Technische Universität Berlin, 1936.

R. Simonini, I. Ansaloni, F. Cavallini, F. Graziosi, M. Iotti, G. M. N'Siala, M. Mauri, G. Montanari, M. Preti, and D. Prevedelli. Effects of long-term dumping of harbor-dredged material on macrozoobenthos at four disposal sites along the Emilia-Romagna coast (Northern Adriatic Sea, Italy). *Mar. Pollut. Bull.*, 50(12):1595–1605, 2005.

M. Sinclair, R. Arnason, J. Csirke, Z. Karnicki, J. Sigurjonsson, H. R. Skjoldal, and G. Valdimarsson. Responsible fisheries in the marine ecosystem. *Fisheries Research*, 58(3):255–265, 2002.

C. Smyth and A. E. Hay. Wave friction factors in nearshore sands. *J. Phys. Oceanogr.*, 32 (12):3490–3498, 2002.

C. E. Smyth and M. Z. Li. Wave-current bedform scales, orientation, and migration on Sable Island Bank. *J. Geophys. Res.*, 110(C2):C02023, Feb. 2005.

P. V. Snelgrove. Getting to the bottom of marine biodiversity: Sedimentary habitats: Ocean bottoms are the most widespread habitat on earth and support high biodiversity and key ecosystem services. *Bioscience*, 49(2):129–138, 1999.

P. V. Snelgrove, S. F. Thrush, D. H. Wall, and A. Norkko. Real world biodiversity–ecosystem functioning: A seafloor perspective. *Trends in ecology & evolution*, 29(7): 398–405, 2014.

M. Solan and R. Kennedy. Observation and quantification of in situ animal-sediment relations using time-lapse sediment profile imagery (t-SPI). *Mar. Ecol. Prog. Ser.*, 228: 179–191, 2002.

R. Soulsby. *Dynamics of marine sands: A manual for practical applications*. Thomas Telford, 1997.

R. L. Soulsby and R. J. S. Whitehouse. Prediction of ripple properties in shelf seas - Mark 2 Predictor, Dec. 2005.

R. L. Soulsby, R. J. S. Whitehouse, and K. V. Marten. Prediction of time-evolving sand ripples in shelf seas. *Cont. Shelf Res.*, 38:47–62, 2012.

E. Stehr. *Grenzschicht-theoretische Studie über die Gesetze der Strombank-und Riffelbildung*. Freie u. Hansestadt Hamburg, Behörde für Wirtschaft, Verkehr u. Landwirtschaft, Strom- u. Hafenbau, 1975.

L. Steinle, M. Schmidt, L. Bryant, M. Haeckel, P. Linke, S. Sommer, J. Zopfi, M. F. Lehmann, T. Treude, and H. Niemannn. Linked sediment and water-column methanotrophy at a man-made gas blowout in the North Sea: Implications for methane budgeting in seasonally stratified shallow seas. *Limnol. Oceanogr.*, 61(S1):S367–S386, 2016.

J. Stronkhorst, F. Ariese, B. van Hattum, J. Postma, M. de Kluijver, P. den Besten, M. Bergman, R. Daan, A. Murk, and A. Vethaak. Environmental impact and recovery at two dumping sites for dredged material in the North Sea. *Environmental Pollution*, 124(1):17–31, 2003.

R. Styles and S. M. Glenn. Modeling bottom roughness in the presence of wave-generated ripples. *Journal of Geophysical Research: Oceans*, 107(C8), 2002.

N. Sultan, G. Bohrmann, L. Ruffine, T. Pape, V. Riboulot, J.-L. Colliat, A. De Prunelé, B. Dennielou, S. Garziglia, T. Himmler, T. Marsset, C. Peters, A. Rabiu, and J. Wei. Pockmark formation and evolution in deep water Nigeria: Rapid hydrate growth versus slow hydrate dissolution. *J. Geophys. Res. Solid Earth*, 119(4):2013JB010546, 2014.

M. T. Szpak, X. Monteys, S. S. O'Reilly, M. K. S. Lilley, G. A. Scott, K. M. Hart, S. G. McCarron, and B. P. Kelleher. Occurrence, characteristics and formation mechanisms of methane generated micro-pockmarks in Dunmanus Bay, Ireland. *Cont. Shelf Res.*, 103:45–59, 2015.

J. H. Terwindt. Sand waves in the southern bight of the North Sea. *Marine Geology*, 10(1): 51–67, 1971.

G. Tietze. *Das Jungpleistozän und marine Holozän nach seismischen Messungen nordwestlich Eiderstedts, Schleswig-Holstein*. Christian-Albrechts-Universität zu Kiel, 1983.

P. Traykovski. Observations of wave orbital scale ripples and a nonequilibrium time-dependent model. *J. Geophys. Res.*, 112(C6), 2007.

P. Traykovski, A. E. Hay, J. D. Irish, and J. F. Lynch. Geometry, migration, and evolution of wave orbital ripples at LEO-15. *J. Geophys. Res.*, 104(C1):1505–1524, 1999.

G. J. Underwood and D. M. Paterson. Seasonal changes in diatom biomass, sediment stability and biogenic stabilization in the Severn Estuary. *Journal of the Marine Biological Association of the United Kingdom*, 73(4):871–887, 1993.

C. F. van der Mark, A. Blom, and S. J. M. H. Hulscher. Quantification of variability in bedform geometry. *J. Geophys. Res.*, 113(F3):F03020, Sept. 2008.

J. Van der Molen. The influence of tides, wind and waves on the net sand transport in the North Sea. *Cont. Shelf Res.*, 22(18-19):2739–2762, 2002.

M. Van Ledden, W. Van Kesteren, and J. Winterwerp. A conceptual framework for the erosion behaviour of sand–mud mixtures. *Cont. Shelf Res.*, 24(1):1–11, 2004.

L. C. van Rijn. Sediment Transport, Part III: Bed forms and Alluvial Roughness. *Journal of Hydraulic Engineering*, 110(12):1733–1754, 1984.

Q. Vanhellemont and K. Ruddick. Turbid wakes associated with offshore wind turbines observed with Landsat 8. *Remote Sensing of Environment*, 145:105–115, 2014.

V. A. Vanoni and L.-S. Hwang. Bed forms and friction in streams. *Journal of the Hydraulics Division*, 93(HY3):121–144, 1967.

J. Venditti. *Bedforms in sand-bedded rivers*, volume 4, pages 137–162. Elsevier Inc., 2013.

J. G. Venditti, M. A. Church, and S. J. Bennett. Bed form initiation from a flat sand bed. *J. Geophys. Res.*, 110(F1):F01009, 2005.

S. Vollmer and M. G. Kleinhans. Predicting incipient motion, including the effect of turbulent pressure fluctuations in the bed. *Water Resour. Res.*, 43(5), 2007.

K. E. Webb, D. K. Barnes, and J. S. Gray. Benthic ecology of pockmarks in the Inner Oslofjord, Norway. *Mar. Ecol. Prog. Ser.*, 387:15–25, 2009.

P. Wessel, W. H. Smith, R. Scharroo, J. Luis, and F. Wobbe. Generic Mapping Tools: Improved version released. *Eos, Transactions American Geophysical Union*, 94(45):409–410, 2013.

P. L. Wiberg, D. E. Drake, and D. A. Cacchione. Sediment resuspension and bed armoring during high bottom stress events on the northern California inner continental shelf: Measurements and predictions. *Cont. Shelf Res.*, 14(10-11):1191–1219, 1994.

D. Wildish, H. Akagi, D. McKeown, and G. Pohle. Pockmarks influence benthic communities in Passamaquoddy Bay, Bay of Fundy, Canada. *Mar. Ecol. Prog. Ser.*, 357:51–65, 2008.

A. Wrede, J. Dannheim, L. Gutow, and T. Brey. Who really matters: Influence of German Bight key bioturbators on biogeochemical cycling and sediment turnover. *Journal of Experimental Marine Biology and Ecology*, 488:92–101, 2017.

M. Yalin. On the determination of ripple geometry. *Journal of Hydraulic Engineering*, 111 (8):1148–1155, 1985.

M. S. Yalin. Geometrical properties of sand wave. *Journal of the Hydraulics Division*, 90(5): 105–119, 1964.

U. Zanke. *Grundlagen der Sedimentbewegung*. Springer-Verlag, 1982.

U. Zanke. On the influence of turbulence on the initiation of sediment motion. *International Journal of Sediment Research*, 18(1):17–31, 2003.

M. Zeiler, J. Schulz-Ohlberg, and K. Figge. Mobile sand deposits and shoreface sediment dynamics in the inner German Bight (North Sea). *Marine Geology*, 170(3-4):363–380, 2000.

EIDESSTATTLICHE VERSICHERUNG

gem. § 5 Abs. 5 der Promotionsordnung vom 15.07.2015

Knut Krämer

Leobener Str. 2
28359 Bremen

Matr.-Nr. 3015580

Ich, Knut Krämer, versichere an Eides Statt durch meine Unterschrift, dass ich die vorliegende Dissertation selbständig und ohne fremde Hilfe angefertigt und alle Stellen, die ich wörtlich dem Sinne nach aus Veröffentlichungen entnommen habe, als solche kenntlich gemacht habe, mich auch keiner anderen als der angegebenen Literatur oder sonstiger Hilfsmittel bedient habe und die zu Prüfungszwecken beigelegte elektronische Version (PDF) der Dissertation mit der abgegebenen gedruckten Version identisch ist.

Ich versichere an Eides Statt, dass ich die vorgenannten Angaben nach bestem Wissen und Gewissen gemacht habe und dass die Angaben der Wahrheit entsprechen und ich nichts verschwiegen habe.

Die Strafbarkeit einer falschen eidesstattlichen Versicherung ist mir bekannt, namentlich die Strafandrohung gemäß § 156 StGB bis zu drei Jahren Freiheitsstrafe oder Geldstrafe bei vorsätzlicher Begehung der Tat bzw. gemäß § 161 Abs. 1 StGB bis zu einem Jahr Freiheitsstrafe oder Geldstrafe bei fahrlässiger Begehung.

Bremen, den 10. April 2018 _____

Knut Krämer